UNIVERSITÉ DE STRASBOURG
École doctorale des sciences de la vie et de la santé
IGBMC - CNRS UMR 7104 - Inserm U 1258

THÈSE
présentée par

Robert FAGIEWICZ

pour obtenir le grade de :
Docteur de l'université de Strasbourg

Discipline/ Spécialité :
Biophysique et Biologie Structurale

Structural studies of the cytoplasmic dyneins and the BicD2 cargo adaptor

Études structurales des dynéines cytoplasmiques et de l'adaptateur cargo BicD2

Soutenue publiquement le **3 février 2022**

THÈSE dirigée par :

Dr SCHMIDT Helgo	Chargé de recherche, IGBMC, Strasbourg, France

RAPPORTEURS :

Dr BAFFET Alexandre	Chargé de recherche Institut Curie, Paris, France
Dr MÉNÉTREY Julie	Directrice de Recherche I2BC, Gif-sur-Yvette, France

AUTRES MEMBRES DU JURY :

Dr ROBERTS Anthony	Chargé de recherche University of London, United Kingdom
Dr RUFF Marc	Directeur de recherché IGBMC, Illkirch-Graffenstaden, France

Once upon a time, a self-replicating molecule appeared. It became a cell, then a clump of cells, then a squishy worm sort of thing, then a fish, then an ape, then a guy who said none of that stuff ever happened. Later, a British man worked it all out and people told him he looked like a monkey.

History of biology
Science: Abridged Beyond the Point of Usefulness

Acknowledgements

First I would like to thank my supervisor Helgo Schmidt for accepting me as his first Ph.D. student. Thank you for guiding me when I needed it the most, teaching me pretty much everything on the bench, and always being enthusiastic when I wasn't. I am grateful for your support, patience, keeping the team social, and being kind to every one of us.

I would like to thank my thesis committee members: Alexandre Baffet, Julie Ménétrey, Anthony Roberts, and Marc Ruff for taking the time to read and evaluate this thesis.

Special thanks go to the past and current lab members. Piotr for everyday coffee breaks and countless discussions about daily bench work. Géraldine for bringing a lot of positive energy to the group and chats about life and career. Torben for your weird sense of humor, daily lunches, and sharing the lab space in the past years - you're a great labmate! Last but not least Johan for all the help with the data processing and chats about cryoEM.

I would like to thank all the people from IGBMC that made these projects happen. Your enthusiasm and passion about science made my time here a pleasant learning experience. I have never anticipated learning so many things during my Ph.D. from so many experts. In the cryoEM platform, I would like to thank Corinne, Nils, Alexandre, Julio, and Gabor for their guidance in sample optimization, data collection, and processing. In the biocrystallography platform Alastair and Pierre for their involvement in all of my crystallographic endeavors. Catherine for helping me out with most of the biophysics done in this work. In the molecular biology platform, big thanks go to Paola for giving me a hand in generating ridiculously large plasmids and not losing her mind with my projects. Isabelle and Evelina in helping me to get started with the insect cell cultures. Also, I would like to thank my first labmates at IGBMC: Adam and Olga, the scientific discussions with you were always enlightening.

Special thanks also go to Bruno Kieffer, Celia Deville, and Marc Ruff. Scientific discussions with you led the project forward. Your expertise is simply priceless and I wish everyone to have scientists like you around.

From a social perspective, I can't express my gratitude to all people who have made my time in Strasbourg an amazing experience. My workmates Pernelle, Ayesha, Anna, Camille, Pau, Beatriz, Christophe, Jason, Katka, Monica, Alexey. The poster session team members Sara, Pierre, Nicla, and all the people from the Students and Post-docs Board. Big hugs to Pernelle, Ayesha, Alastair, and Paola for all coffee breaks and nights out.

I'm also very grateful for my amazing flatmates who made me realize that being a singer or a contemporary dancer can be as complicated as being an academic. I would like to thank my most recent flatmates Juliette, Ezgi, and George, living with you was a blast and I could not wish for better people around.

Special thanks go to my friends Bollin, Fusik, Farba, Bebe and Wicek, Mateusz, François, Lionel, Saba, Alicja and Dan, Laura, Klaudia, and many more people that I've had a great time during these years. Also, I would like to thank my sister for her outstanding support. Without you, this would have been much more difficult.

Contents

Résumé de thèse

Études structurales des dynéines cytoplasmiques

Ces dernières années, les protéines motrices dynéines ont suscité beaucoup d'attention. Le développement de nouvelle analyse structurale telle que la cryo-microscopie électronique (cryo-ME), a permis de visualiser les déplacements de la dynéine avec multiples de ses partenaires comme les microtubules,[1,2,3] les trains de transport intra-flagellaires (IFT), [4,5] la dynactine, les complexes adaptateurs de cargos,[6] et dans les axones de mammifères.[7] Malgré ces avancées, de nombreuses questions fondamentales subsistent sur l'activité motrice de la dynéine et des mécanismes de fixation avec les protéines cargos. En effet, le cycle mécano-chimique, responsable du remodelage du segment de liaison (ou linker) et générateur de forces, n'est pas clairement défini. De plus, les méthodes de recrutement des adaptateurs cargos et leurs spécificités de liaison avec la dynéine ne sont pas caractérisées.

J'ai voulu aborder ces questions au cours de ma thèse sous la forme de deux principaux projets. Dans le projet 1, j'ai utilisé le domaine moteur de la dynéine-2 comme modèle pour étudier les « insertions » ainsi que leurs rôles dans le remodelage des linkers. Ces insertions ont déjà été observées comme jouant un rôle dans la course motrice de la dynéine, mais n'ont jamais été décrites structuralement. Dans le projet 2, j'ai souhaité reconstituer et étudier le complexe de la dynéine entièrement assemblé, comprenant la dynactine, l'adaptateur cargo et le cargo. Il n'a jamais été démontré qu'un tel complexe pouvait être reconstitué in vitro. Cette méthodologie permettrait de progresser significativement notre compréhension sur la mobilité de la dynéine, ainsi que de son activation et le recrutement de protéines cargos.

Projet 1: Contribution des éléments de la structure secondaire au remodelage du linker du moteur de la dynéine

Le déplacement de la dynéine le long des microtubules nécessite l'attachement et le détachement cyclique des microtubules tout en générant une force. Les dynéines génèrent la force nécessaire au mouvement en hydrolysant de l'ATP dans leur anneau AAA+. Cet anneau AAA+ contient quatre sites de liaison aux nucléotides. Le site AAA1 est responsable de la génération de la force et de la régulation de l'affinité des domaines de liaisons des microtubules (MTBD).[8,9,10,11,12,13] La dynamique du domaine moteur nucléotides-dépendant peut être divisé en plusieurs états. Dans l'état APO, l'anneau AAA+ est largement ouvert et le linker adopte une conformation droite. Cette conformation APO est post-course motrice et l'affinité du MTBD au microtubule est élevée. Lors de la liaison de l'ATP dans le domaine AAA1, l'anneau AAA+ se ferme, le MTBD se dissocie du microtubule. Le linker adopte alors une conformation courbée, pré-course motrice, où sa fente centrale agit comme un point de pivot (Figure 1). Une fois que l'hydrolyse de l'ATP en ADP et phosphate (Pi) a été effectuée, la dynéine refixe le microtubule, ce qui réouvre l'anneau AAA+ et stimule le redressement du linker – cela correspond au coup de force produisant la course motrice (ang. 'power stroke').[14] Après la libération de l'ADP du site AAA1, le moteur est prêt pour un autre cycle d'hydrolyse de l'ATP et une étape consécutive sur le microtubule.

L'état nucléotidique dicte la position du linker par rapport à l'anneau AAA+. En l'absence de nucléotide (forme APO), la pointe du linker est arrimée au domaine AAA5. Au cours de la liaison et de l'hydrolyse de l'ATP (avant le coup de force), la pointe du linker est établie à l'interface des domaines AAA2 et AAA3. Après le coup de force et la libération du Pi, le linker se redresse et se fixe au domaine AAA4. Un déplacement supplémentaire de l'extrémité N-terminale du linker vers le domaine AAA5 induit l'ouverture de l'anneau AAA+ et la libération de l'ADP du site AAA1. Ce remodelage du linker nucléotide-dépendant est l'élément clé du cycle mécano-chimique de la dynéine.[8] Jusqu'à présent, plusieurs états nucléotidiques ont été structuralement décrits : AMPPNP,[15,16] ADP,[17] et ADP.Vi.[14] Bien que nous disposions de quelques aperçus de la structure du moteur de la dynéine dans différents états nucléotidiques, la manière dont l'anneau AAA+ soutient réellement le remodelage du linker reste encore inconnu.

Certains éléments de structure secondaire de l'anneau AAA+ pourraient être responsables du remodelage du linker. Ces éléments sont appelés "insertions" et sont

présents dans les domaines AAA1-5 de la dynéine. Ces derniers sont constitués d'extensions α-hélicoïdales ou d'épingle à cheveux β, de la structure de base α/β AAAL. Ils résident sur la face du linker de l'anneau AAA+. Leurs emplacements sont indiqués sur la figure 1 et résident dans le domaine moteur de la dynéine. Les insertions ont également une nomenclature spécifique qui précise leurs emplacements dans le domaine AAA. L'insertion H2 est une épingle à cheveux β qui émerge de l'hélice H2 du domaine AAA. Il pointe vers le centre de l'anneau AAA+ pour interagir avec le substrat dans certaines protéines AAA+. L'insertion pré-sensorielle I (PS-I) est une insertion entre l'hélice 3 et le brin 4 du domaine AAA.[18]

Il semblerait que l'insertion PS-I du domaine AAA4 provoquerait un conflit stérique avec l'extrémité N-terminale du linker lors de la fermeture de l'anneau AAA+. Induit par la présence d'ATP, elle déclencherait la flexion du linker.[19] Les insertions PS-I et H2 du domaine AAA2 ont également été associées au remodelage du linker.[17] Elles sembleraient interagir avec la région du point pivot dans le domaine linker pour participer au remodelage de ce dernier. A ce jour, aucune de ces hypothèses n'a pu être vérifiée par une étude structurale. J'ai ainsi voulu évaluer, en utilisant une approche structurale, la contribution de ces éléments au remodelage du linker. Le domaine moteur de la dynéine-2 est un excellent modèle pour étudier la contribution des insertions. En effet, dans ce système il y a peu, voire pas d'interférence dans l'hydrolyse des nucléotides dans les autres domaines : le domaine AAA3 est dépourvu de résidus catalytiques;[16,20] le domaine AAA4 est peu conservé ; les domaines AAA5 et 6 ne possèdent pas de sites de liaison aux nucléotides. Pour cette raison, j'ai choisi la dynéine-2 dans mes études et je me suis fixé les objectifs suivants:

1. Production du domaine moteur de la dynéine-2 humaine recombinante : WT (native), ΔAAA2 PS-I et H2, ainsi que ΔAAA4 PS-I;
2. Étude cryo-ME à haute résolution de ces délétions et évaluation de leurs influences sur le comportement du domaine moteur et du linker.

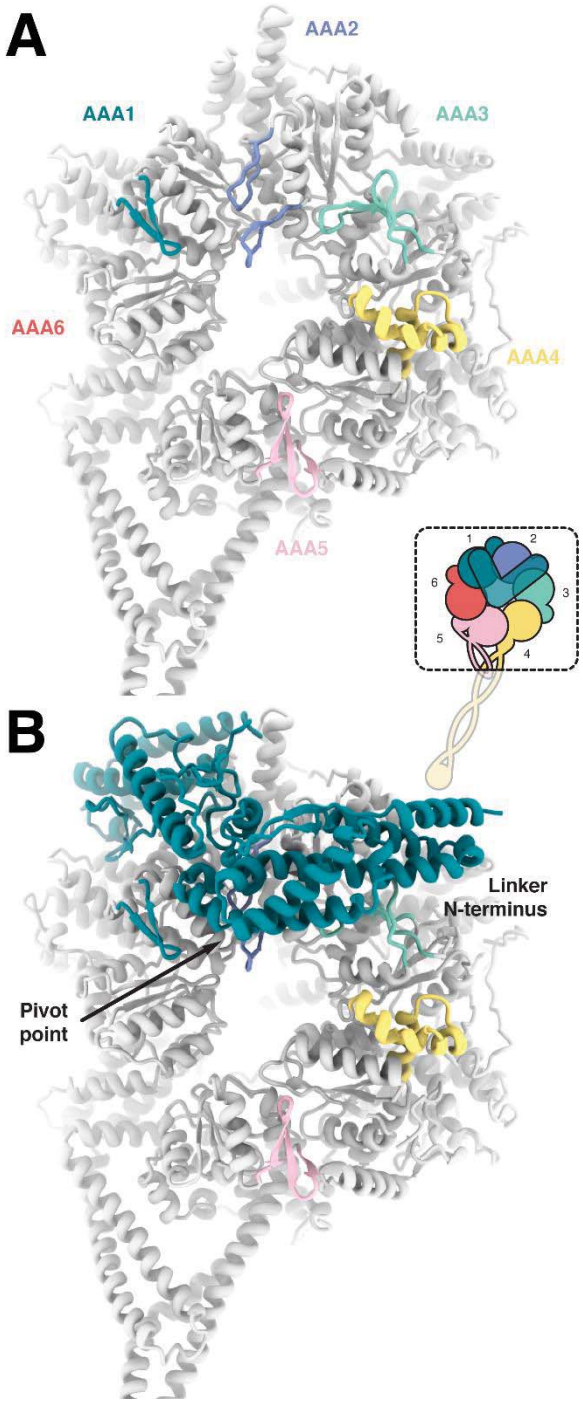

Figure 1. A Emplacement des insertions dans les domaines AAA1-5 de la dynéine-2, PDB : 4rh7 (le domaine linker a été enlevé pour des raisons de clarté). **B** Domaine moteur de la dynéine-2. Le point pivot du linker et la partie N-terminale sont mis en avant.

Projet 2: Études structurales du complexe de la dynéine impliqué dans le développement du néocortex

Le néocortex est un tissu cérébral spécifique aux mammifères, associé à des capacités cognitives élevées. Dans le cerveau adulte, le néocortex est constitué de six couches, dont deux sont la zone ventriculaire et la plaque corticale.[21] Chaque couche contient des neurones pyramidaux d'un sous-type spécifique qui sont générés à partir de cellules progénitrices gliales radiales apicales (abrégée RGPCs) situées dans la zone ventriculaire. Les RGPCs de la zone ventriculaire se divisent pour générer des progéniteurs intermédiaires qui migrent le long des RGPCs, de la zone ventriculaire vers la plaque corticale, où ils se différencient en neurones pyramidaux. La division des RGPCs pour générer des progéniteurs intermédiaires est régie par le cycle mitotique des RGPCs. Il est étroitement lié aux mouvements oscillatoires de leurs noyaux, un phénomène également connu sous le nom de migration nucléaire inter-cinétique (abrégé INM ci-après).[22] En phase G1 du cycle cellulaire, le noyau se déplace du côté apical au côté basal de la zone ventriculaire. Une fois que le noyau a atteint le côté basal, les RGPCs entrent en phase S. Au cours de la phase G2 suivante, le noyau se déplace à nouveau vers le côté apical de la zone ventriculaire, où les cellules subissent une mitose pour générer les cellules progénitrices intermédiaires, qui se déplacent dans la plaque corticale du néocortex pour se différencier en neurones. Le mouvement de ces cellules progénitrices intermédiaires de la zone ventriculaire vers le néocortex est guidé par les RGPCs, qui traversent latéralement l'ensemble du néocortex. La représention schématique de la migration neuronale guidée par l'INM et les RGPCs est présentée dans la figure 2. La fonction biologique de la migration nucléaire inter-cinétique dans les RGPC n'est pas bien comprise. Il a été supposé qu'elle pourrait permettre de regrouper un grand nombre de RGPCs dans un espace limité, augmentant ainsi le nombre de progéniteurs intermédiaires pouvant être générés dans la zone ventriculaire.[22] Le renflement nucléaire des RGPCs conduirait à de grands espaces vides, si ces cellules étaient regroupées latéralement. En raison de l'INM, la position du renflement nucléaire varie entre les RGPCs voisins, ce qui permet un empilement serré des cellules voisines. Bien que le rôle biologique de l'INM dans les RGPCs fasse encore l'objet de débats, son importance pour le développement du cerveau des mammifères n’est plus à prouver et est reflété par plusieurs neuropathologies telles que la lissencéphalie (phénotype de cerveau lisse) et la microcéphalie (phénotype de cerveau de taille réduite).

De premières études ont établi que le processus INM dépend des microtubules ainsi que des protéines motrices associées aux microtubules.[23,24,25] La protéine motrice Kif1a (qui se dirige vers l'extrémité positive des microtubules), est un membre de la famille des protéines motrices de la kinésine. Elle transporte les noyaux pendant la phase G1 du cycle cellulaire vers le côté basal de la zone ventriculaire, où les extrémités positives (+) des microtubules se regroupent.[24] Les extrémités négatives (-) des microtubules dans les RGPCs se regroupent sur le côté apical de la zone ventriculaire. Le mouvement des noyaux, de la partie basale vers la partie apicale pendant la phase G2, est dirigé par la dynéine, une protéine motrice associée aux microtubules. Elle transporte les protéines cargos vers l'extrémité négative des microtubules.[25] Le mouvement nucléaire apical piloté par la dynéine se déroulerait en deux phases. Dans la première phase, la dynéine et son activateur ubiquitaire, la dynactine, sont recrutées dans le noyau par une interaction avec le composant du pore nucléaire RanBP2, ainsi qu'avec la participation de la protéine d'échafaudage BicD2.[25,26] La deuxième phase est contrôlée par le composant du pore nucléaire Nup133 qui se lie à CENP-F, lequel recrute la dynéine/dynactine via les protéines NudE et NudEL.[25,27,28] La synchronisation de ces mouvements nucléaires, avec la phase G2 du cycle cellulaire, est assurée par l'activité de la kinase mitotique CDK1. CDK1 phosphoryle RanBP2 qui à son tour se lie à BicD2. BicD2 recrute la dynéine/dynactine pour conduire la première phase de la migration nucléaire ventriculaire. La deuxième phase de la migration nucléaire apicale des RGPCs implique le joueur clé CENP-F, qui réside à l'intérieur du noyau jusqu'à la fin de la G2. Dans ce cas, l'activité de CDK1 est nécessaire pour relocaliser CENP-F du noyau vers le cytoplasme. Il se lie à Nup133 pour initier la seconde phase de migration nucléaire apicale des RGPCs.[27] La raison de l'existence de deux voies distinctes de recrutement de la dynéine au cours de la migration apicale des RGPCs n'est pas claire pour le moment. Il semblerait que la voie tardive de CENP-F pourrait permettre une meilleure coordination entre le cycle mitotique et l'arrivée du noyau RGPC sur le côté apical de la zone ventriculaire. CENP-F quitte le noyau environ au même moment que la Cycline B y entre, ce qui pourrait garantir que la séparation des centrosomes, la rupture de l'enveloppe nucléaire et l'assemblage des kinétochores soient coordonnées avec les étapes finales de migrations nucléaires médiées par CENP-F vers le côté apical de la zone ventriculaire.[27]

Il existe également des preuves expérimentales solides de l'implication du régulateur de dynéine Lis1 dans la migration nucléaire des RGPCs.[23] La suppression de Lis1 par l'intermédiaire d'un siRNA, dans un cerveau embryonnaire en développement de rat, abolit presque complètement la migration nucléaire oscillatoire dans les RPGCs. Cet effet peut être expliqué par la capacité de Lis1 à induire un état de liaison aux microtubules dans la dynéine plus fort et plus résistant à la force.[29] Ce qui pourrait être nécessaire lorsque la dynéine transporte de grands cargos tels que les noyaux. Des dysfonctionnements dans les voies de recrutement de la dynéine médiées par RanBP2 et Nup133 entraînent l'arrêt des noyaux RGPCs qui ne parviennent pas à atteindre le côté apical de la zone ventriculaire et qui, par conséquent, ne subissent pas de mitose, ce qui a des conséquences dévastatrices sur le développement du néocortex.[30,23,31]

La base structurale de la migration nucléaire des RGPCs pilotée par la dynéine reste inconnue, malgré son importance bien établie dans le développement du néocortex. Nous ignorons comment le composant du pore nucléaire RanBP2 recrute les complexes de dynéine pour promouvoir la migration nucléaire des RGPCs. En plus du recrutement, l'activité motrice de la dynéine doit également être activée. En effet, la dynéine existe dans un état d'auto-inhibition qui n'est levé que lorsqu'elle se lie à un adaptateur cargo et à la dynactine.[32,33,34,35] Pour les complexes cargos comprenant BicD2, comme pour le cas de la voie de recrutement de RanBP2, un mécanisme d'activation potentiel a récemment été suggéré.[35] Malheureusement, ces hypothèses ont été tirées d'expériences effectuées sur BicD2 tronqué et/ou BicD de drosophile. Pour étudier la question essentielle du recrutement et de l'activation de la dynéine par RanBP2, je me suis fixé les objectifs suivants:

1. Production de BicD2 humain recombinant sous forme entière et biochimiquement actif;
2. Reconstitution et études structurales du complexe BicD2-RanBP2$_{BBD}$;
3. Études cryo-ME à haute résolution du complexe DDBR2 reconstitué in vitro;

La majorité de ce travail a été publié dans le manuscrit intitulé « In-vitro characterization of the full-length human dynein-1 cargo adaptor BicD2 ». Toutes les expériences supplémentaires soutenant ce travail sont décrites dans la section des résultats de ce manuscrit.

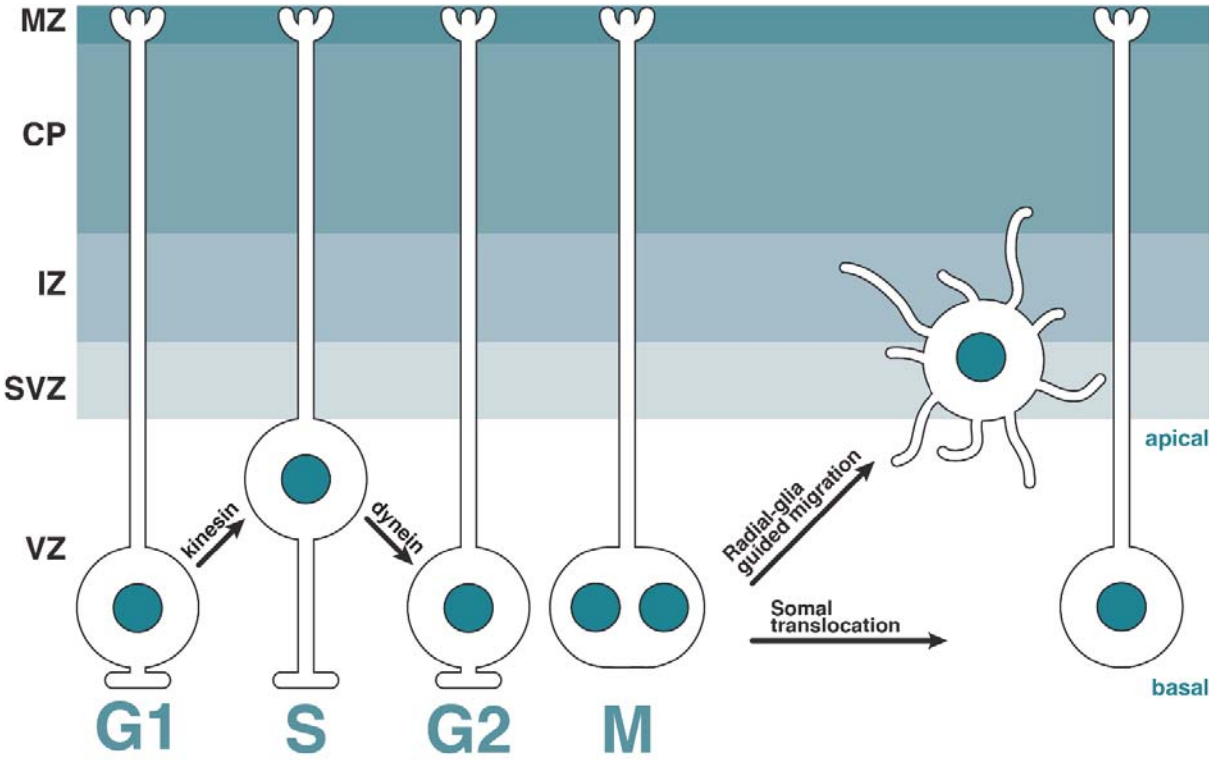

Figure 2. Illustration du processus INM dans la zone ventriculaire (VZ) du néocortex. Une fois la mitose terminée, les cellules progénitrices fraîchement formées vont se différencier en divers types de neurones et peupler la plaque corticale par translocation guidée par la glie radiale ou translocation somale.

Publications and oral communications

Publications

Fagiewicz R., Crucifix C., Deville C., Kieffer B., Nominee Y., Busselez J., Rossolilo P., Schmidt H., In vitro characterization of the full-length human dynein-1 cargo adaptor BicD2. Manuscript submitted to Structure, (2021).

Sosnowski, P.,* Urnavicius L.,* Boland A., **Fagiewicz R.**, Busselez J., Papai G., Schmidt H., The CryoEM structure of the Saccharomyces cerevisiae ribosome maturation factor Rea1. Elife 7, (2018). *first co-authors

Talks

IGBMC Internal Seminar
Structural studies of a human cargo adaptor BicD2;
09.12.2021, Strasbourg, France

Motors in Quarantine Webinar Series
Self-regulation and cargo recruitment of a human cargo adaptor BicD2;
01.12.2021, On-line meeting

Invited talk
Self-regulation and cargo recruitment of a human cargo adaptor BicD2;
10.11.2021, University of California San Diego, USA

35th Scientific Summer Seminar of the Boehringer Ingelheim Fonds 2019
Stimulating interaction of dynein-1 with its cargo for structural studies;
03-09.08.2019, Hirshegg, Austria

34th Scientific Summer Seminar of the Boehringer Ingelheim Fonds 2018
Structural studies of cytoplasmic dynein-1 involved in the neocortex development;
18-24.08.2018, Hirshegg, Austria

Posters

IGBMC Poster Sessions

Structural studies of the cytoplasmic dynein involved in the neocortex development;

2018-2020, Strasbourg, France

Cryo 3D Electron Microscopy

Dynein binding to its cargos – a structural approach;

31 May - 9 June 2019, Erice, Italy

IGBMC-IBMC Annual Structural Biology Department Retreat

Structural studies of the cytoplasmic dynein involved in the neocortex development;

December 2017, Liebfrauenberg, France

List of figures and tables

Abbreviations

AAA+ - ATPases associated with various cellular activities

ADP - Adenosine diphosphate

ADP.P_i - Adenosine diphosphate and inorganic phosphate complex

ADP.V_i - Adenosine diphosphate and inorganic vanadate complex

APO - Nucleotide-free state

ATP - Adenosine triphosphate

CC – Coiled coil

CD - Circular dichroism

CHAPS - 3-((3-Cholamidopropyl)dimethylammonium)-1-propanesulfonate

CMC - Critical micelle concentration

cryoEM - Cryo-electron microscopy

cryoET - Cryo-electron tomography

DSF - Differential scanning fluorimetry

GDP - Guanosine diphosphate

GOI - Gene of interest

GTP - Guanosine triphosphate

IF – Intermediate filaments

IFT - Intraflagellar transport

INM - Interkinetic nuclear migration

MAP - Microtubule associated proteins

MTBD - Microtubule binding domain

NTPase - Nucleoside-triphosphatase

RGPC - Radial glial progenitor cells

SEC – Size-exclusion chromatography

SEC-MALS – Size-exclusion chromatography multi angle light scattering

INTRODUCTION

1. Introduction

1.1 The Cytoskeleton – giving shape to the cell

The cytoskeleton is a complex network of protein filaments spanning the cell's cytoplasm. It has a multitude of functions, the most fundamental ones are to give the cell its shape and to control its physical properties.[36] The cytoskeleton provides the cell with the ability to contract to aid cell migration through deformation.[37] It is essential in cell signalling pathways and endocytosis[38], segregation of chromosomes[39], cytokinesis during cell division[40], and may act as an epigenetic determinant of cell shape, function, and fate.[37] The latter also gives the cell the ability to form very specialized structures such as flagella and cilia. The cytoskeleton is present in all organisms, including bacteria and archaea[39], but its structure, function, and dynamics strongly depend on the organism and cell type.[40] The large-scale and more visual example of cytoskeleton function is muscle contraction, where actin-dependent motors collectively exert forces on parallel actin filaments.

The eukaryotic cytoskeleton consists of three types of biopolymers: actin filaments, intermediate filaments, and microtubules. Each of these has a unique ability to assemble and disassemble depending on the current cell requirements. Actin filaments are solid rods with a diameter of ~7 nm that are composed of the globular protein G-actin, which in its filamentous form is known as actin (or F-actin). The ATP-dependent polymerization of G-actin results in polar filaments. There is a growing (+) end that tends to assemble and disassemble quicker than the (-) end (Figure 1). Actin filaments have a structural role in the cell and they can bear a large amount of tension.

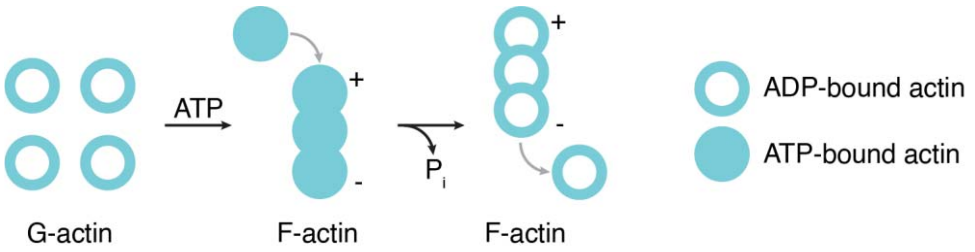

Figure 1. Schematic illustration of actin assembly and disassembly. The globular actin monomers (G-actin) polymerize into filamentous actin (F-actin) upon ATP binding. As the ATP hydrolysis progress the F-actin will depolymerize into ADP-bound actin.

When associated with the motor protein myosin, they participate in force generation during cellular contraction and cell body movement.[41]

The diameter of intermediate filaments (IF) is slightly larger (~10 nm) than that of microfilaments, but smaller than the diameter of microtubules (~25 nm) – hence the name 'intermediate'. They are made of fibrous proteins that contain a central α-helical rod domain. The building blocks of IF's are intertwined coiled coils. They have an antiparallel architecture which implies they are unipolar with both ends having identical properties. Also, unlike the microfilaments and microtubules, the polymerization of IF's is nucleotide independent. They have a mechanical role, because they were shown to buffer mechanical stress[36].

Microtubules are long and stiff polymeric structures. These filaments are the largest in diameter (~25 nm), and result from the polymerization of heterodimers of α- and β-tubulin. They form protofilaments that later assemble into a hollow tube – the microtubule (Figure 2). Tubulin is a GTP-dependent protein which similar to microfilaments, creates polar (+) and (-) ends. Microtubule polarity determines assembly start and end but also directs various motor proteins that facilitate cellular

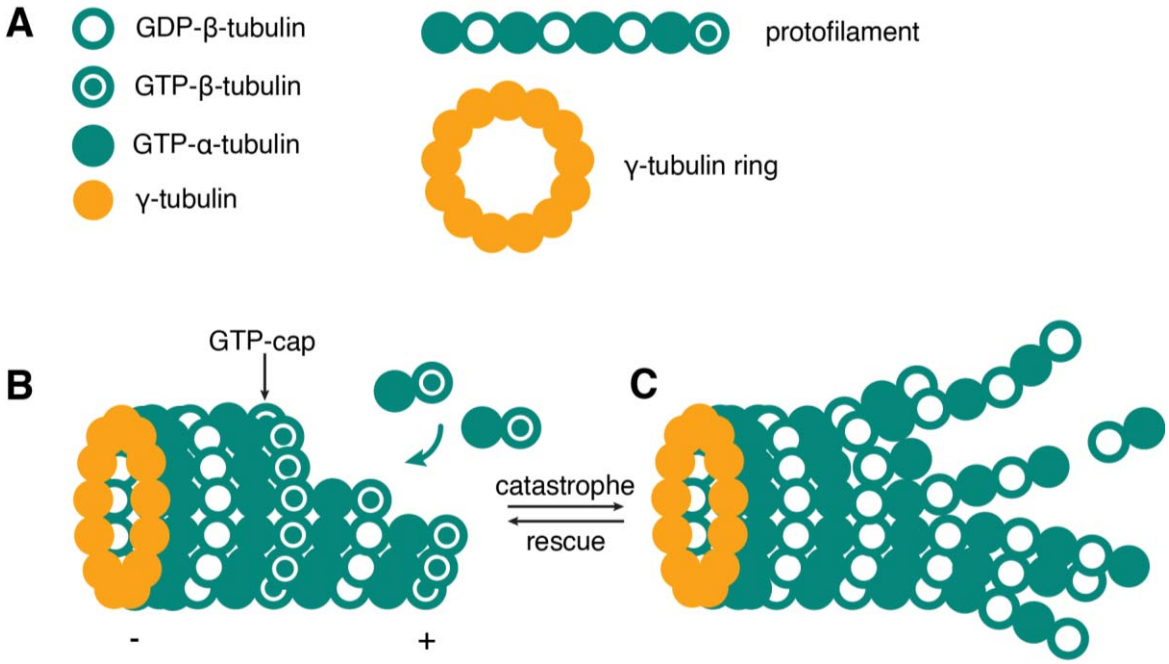

Figure 2. Representation of microtubule dynamic instability. **A** The polar microtubule protofilament is made of β- and α-tubulin units. The polymerizing end contains β-tubulin in the GDP bound state while α-tubulin always stays in the GTP-bound state. The γ-tubulin ring serves as a microtubule nucleating site. **B** Microtubule rescue (assembly). The preformed αβ-tubulin dimers assemble in such a way as to form a GTP cap of β-tubulin. **C** Microtubule catastrophe. The disassembly of the microtubules occurs from the GTP-cap towards the γ-tubulin ring.

transport[42]. Their function and properties are quite broad and will be discussed in more detail in the following sections of this chapter.

1.1.1 Microtubules

α- and β-tubulin are small (~ 55kDa) globular proteins, which form a stable, non-covalent heterodimer. In eukaryotes, α- and β-tubulins are well conserved (~60%) while identity is about 40% between the two. The third form, γ-tubulin, is localized at the centrosome where it serves as a nucleation point for microtubules (Figure 2A). The αβ-tubulin dimers polymerize in a GTP-dependent manner into protofilaments in a head-to-tail fashion (Figure 2B). These protofilaments can later assemble into a hollow tube – the microtubule. In mammals, the microtubule is usually formed through the association of 13 protofilaments, but this number can vary between 10 and 15.[43,44,45,46]

β-tubulin can hydrolyse GTP into GDP, while α-tubulin always stays in the GTP state. During polymerization the nucleotide exchangeable site (E site) of the β-tubulin always contacts the catalytic domain of the α-tubulin of the neighbouring dimer. Protofilaments and microtubules thus have one end with α-tubulin exposed, the (-) end, and the other with β-tubulin exposed, the (+) end. This architecture designates the polarity of each side, and therefore dictates the microtubule growth dynamics, but also directionality for motor proteins. Although growth can occur at both ends it has a higher rate on the (+) end[47]. The (+) end of microtubules is normally stabilized by the minimum GTP cap of one tubulin layer (Figure 2B). As the hydrolysis proceeds, the GTP cap will be lost and microtubule depolymerization begins, the phenomenon also known as microtubule catastrophe (Figure 2C).[43]

1.1.2 Stability and dynamics

Although microtubules are the most stable cytoskeletal filaments because of extensive lateral contacts between their protofilaments[37], they nevertheless switch between constant growth and shrinkage and never reach a steady-state length. This property is known as dynamic instability and has been demonstrated in-vivo and in-vitro.[43,48,49] The switch between the two states depends on the nucleotide state of β-tubulin. When GTP binds to β-tubulin's E-site, the microtubule is in the growth phase and shrinkage occurs upon GTP hydrolysis. The growth dynamics dictate the

microtubule's biological role, whether it is the microtubule's reorganization, spatial and temporal differentiation, or generation of pushing and pulling forces in a cell.[50,51] Moreover, dynamic instability establishes the cell's asymmetry. This comes from the search-and-capture model[50] where microtubules search for their targets, such as plasma membranes, chromosomes, and organelles during the inter-conversion between the growth and shortening cycles. This leads to cell polarization through selective microtubule stabilization, as a result of the microtubule's response to environmental signals and/or factors. Microtubules are also regulated by microtubule assembly-promoting factors, microtubule-stabilizing and destabilizing factors (such as microtubule-associated proteins – MAP's), microtubule severing proteins, and microtubule-based motors from the kinesin and dynein superfamilies.[52,53,54]

1.1.3 Microtubules and traffic control

The polarity-driven spatial arrangement of microtubules inside the cell orchestrates the multiple-cargo carrying motors. Microtubule-based motors are finely regulated to move in the desired direction, at the right moment, and with the right cargo. We have relatively little knowledge about how cells regulate switching between anterograde and retrograde transport. The anterograde transport is driven towards the (+) end of microtubules - away from the cell body, and retrograde transport goes along the (-) end of microtubules, hence toward the cell body. Microtubule structures that can provide a good understanding of motor function are axons and the flagellum as they are specialized for long-distance intracellular transport. In the past years these cellular structures have served as model systems for the development of new cryoEM methods.[55,56,57]

Flagellar IFT transport consists of a continuous stream of anterograde and retrograde migration of so-called IFT-trains on the axoneme, which is composed of microtubule doublets. The axoneme is the core structure found in eukaryotic flagella and cilia. It determines the shape of these organelles and, in the case of motile cilia, bends them. Dynein and kinesin have to be bound to the IFT train at the same time, but only one motor is active depending on the direction of the transport. Kinesin is involved in anterograde transport, and dynein is responsible for retrograde transport. The retrograde IFT trains are known to be smaller and faster compared to anterograde

one, which already indicates that both species have distinct protein compositions.[58] The IFT dynein needs a heterotrimeric kinesin II to reach the flagellar tip, suggesting that it is inactive during anterograde transport. Once the IFT train reaches the flagellar tip it dissociates from the microtubule doublets. Subsequently, the IFT trains undergo a remodeling event (cargo unloading for axoneme maintenance) and dynein gets activated to bring the IFT trains back to the basal end of the flagellum by the retrograde transport.[58] The nature of this remodeling event is still unclear. In Chlamydomonas it has been shown that it consists of the IFT particle remodeling at the flagellar tip to control the length of the flagella.[59] At the flagellar base the reverse process must be taking place. New cargo is loaded, kinesin II becomes the active motor, and dynein gets inactivated.[60] This IFT train flux is continuously recycled within the flagellum and can keep on going for hours without the need for protein synthesis.[61]

Another example of long-distance microtubule trafficking is on the axon of nerve cells. Some axons can be meters long, hence they cannot rely on passive diffusion and have developed a similar cargo trafficking to flagellum – a retrograde and anterograde transport.[62] There are plenty of cargos moving along single microtubule filaments between the cell body and the axon end, such as lipids, proteins, organelles or synaptic vesicles. The regulation of the cargo flux is also similar to that of IFT, as the cargos usually recruit the microtubule motors dynein and kinesin at the same time. Although axonemal cargos can show bidirectional movement, they usually have one overall preferred direction of movement, suggesting that only one of the opposing dynein and kinesin motors is active at one time.[63,64] It is also possible that both motors become active and engage in a so-called tug-of-war competition.[65] During kinesin mediated anterograde transport, activation of the opposing dynein motor can be stimulated upon injury, or any other scenario where the axonal transport is blocked. The vesicles building up at the blocked site can reverse their direction towards the cell body[66], partly mediated by the recruitment of additional dyneins.[63]

Microtubule-based transport in flagella and axons has raised many questions about motor protein regulation. It is still unclear how they coordinate their activity with respect to each other, and what drives the turnaround events along the filaments. Recent advances in cryoET have given some new insight into the inner architecture of the axoneme,[67] but many mechanistic details are still missing. What is interesting about these transport events is the cross-talk between dynein and kinesin. Impairment

of one of these motors abolishes both the anterograde and retrograde transport processes. This implies that a lack of activity of one motor is somehow 'communicated' to the active motor.[68,69,70,71] It has been suggested that this phenomenon can be controlled by dynactin at a molecular level. This is because dynein and kinesin II can bind to an overlapping site in the p150Glued component of dynactin.[69]

1.2 Cytoplasmic dyneins

1.2.1 Dynein transport and discovery

Microtubules are essential for intracellular transport. Their polarity and localization within the cell make them suitable 'highways' for motor proteins. Motor proteins use microtubules to move vesicles, organelles, protein- and RNA-containing complexes, and viruses to specific cell locations.[72] Dyneins were first isolated from Tetrahymena pyriformis and imaged by metal-shadowing electron microscopy in 1965 by Gibbons and Rowe.[73] Later, two cytoplasmic isoforms of dynein were identified (dynein-1 and dynein-2), where dynein-1 is the cytoplasm-based motor, and dynein-2 the cilia based-motor.[74,75,76]

It has been demonstrated that dynein-1 is essential in fruit fly (Drosophila melanogaster) [77] and mouse (Mus musculus).[78] Mutations in dynein-1 are known to cause several neuropathologies in humans. These include neurodegenerative diseases, such as the Parkinson's disease-like Perry syndrome, spinal muscular atrophy with lower extremity predominance (SMA-LED), hereditary motor neuron disease, and Charcot-Marie-Tooth disease. They also include neurodevelopmental disorders such as lissencephaly and microcephaly.[79,80,81,82,83,84,85] The impairment of dynein-1 associated proteins has also been shown to cause various cortical malformations and intellectual disabilities.[86]

Cytoplasmic dynein drives the majority of retrograde microtubule transport events in eukaryotic cells. The cytoplasmic dynein-1 isoform facilitates cell division, the migration of organelles and vesicles, brain and muscle development, and can also be hijacked by pathogenic viruses to reach specific cellular locations.[72,87,88,89] It is a particularly interesting motor in neurons, as it carries essential signals and organelles from distal axon sites to the cell body.[90] The cargos of dynein-1 can be grouped into four main categories: membranes, RNAs, proteins, and viruses. The type of cargo

recruited depends on a number of factors, such as the phase of the cell cycle, or cargo adaptors and regulators such as kinases and phosphatases. This range of interactions suggests that dynein can form higher-order complexes to achieve its cellular functions. Over 30 years after the discovery of dynein, a high molecular weight complex was identified to be crucial for dynein-1 motility on microtubules - the dynactin complex.[91,92] Furthermore, it was shown that the complex associates in the presence of dynein cargo adaptors such as BicD2 – a long and flexible protein that links dynein, dynactin, and the cargo for processive movement along the microtubules. BicD2 is a human homolog of Drosophila BicD, which was identified in 1986.[93] The BicD family of dynein cargo adaptors are relatively large, mostly coiled-coil proteins, that are known to increase the motility of the dynein-dynactin-BicD2 (DDB) complexes in vitro.[32,94] In addition to BicD2 and its homologues, there are several protein families that act as cargo adaptors, and they share the common feature of recruiting dynein, dynactin and adaptor-specific cargos.

Dynein-1, dynactin, and the cargo adaptor are the principal components of the (-) end microtubule-based motor machinery. The speed and affinity of this complex on microtubules are also regulated by Lis1 and two nuclear distribution proteins NDE and NDEL1.[95,96,97] These three proteins can alter dynein's motor properties and they help the DDB complex to assemble correctly.[98] Moreover cytoplasmic dynein-1 and -2 associate with several light chains that regulate correct motor complex assembly and interaction with other proteins.

Dynein-2 is another cytoplasmic isoform of dynein and was first identified in sea urchin (Echinoidea) and rat (Rattus norvegicus) in 1994.[99,100] A few years later it was shown that the light chain of dynein-2 is associated with retrograde IFT in Chlamydomonas and its mutations led to IFT accumulation at the flagella's tip and impairment of kinesin-based trafficking in Caenorhabditis elegans.[101,102,103]

Dynein-2 forms a large complex with kinesin-2 to transport IFT-A and IFT-B complexes from the ciliary base to the tip and back to the cell body.[104] The IFT train consists of IFT-A and IFT-B complexes (Figure 5D) which are driven by kinesin-2 to reach the ciliary tip. At the tip the IFT trains undergo some kind of rearrangement (which is not yet well understood) which activates dynein-2 for retrograde transport.

Even though dynein-2 almost uniquely operates within cilia, there is evidence that it plays cytoplasmic roles in Chlamydomonas, which lacks a dynein-1 isoform.[105]

Within cilia, dynein-2 is attached to the IFT train and passively transported from the ciliary base towards the tip by the motor protein kinesin-2 in an inactive form.[106,107] Microtubule gliding assays have shown that the dynein-2 dimer is less motile compared to dynein-2 alone.[34,4] In a dimer, the dynein's motor domains stack against each other forming an autoinhibited state. This state is speculated to be an inactive form of dynein-2 that is transported by kinesin-2 during anterograde IFT trafficking. These in vitro observations were further confirmed by in vivo cryoET in Chlamydomonas showing anterograde IFT trains with dynein-2 in a compact, autoinhibited conformation with stalks pointing away from the microtubule doublets.[108]

1.2.2 Dynein as a P-loop NTPase

The dynein heavy chain generates the power to move along the microtubules. The motor domain of dynein belongs to the family of the AAA+ proteins (**A**TPases **A**ssociated with various cellular **A**ctivtities) which in turn belongs to a larger protein family – the P-loop NTPases. The P-loop NTPases are nucleotide-dependent proteins that are able to harness the chemical energy of ATP hydrolysis and convert it into mechanical work. Nature evolved many of those essential-for-life enzymes and they are present in all three domains of life: archaea, bacteria, and eukarya.[18] Around 10%

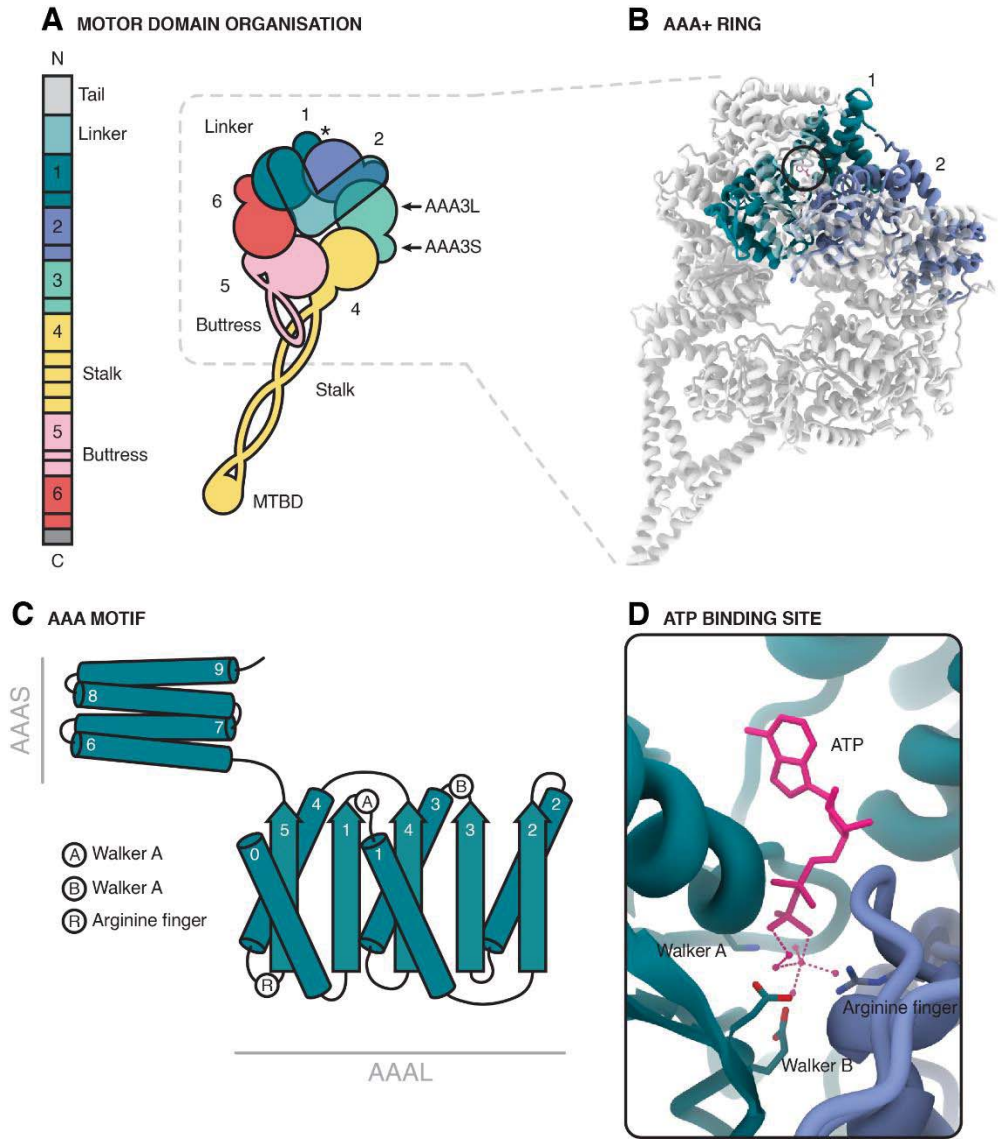

Figure 3. Cytoplasmic dynein motor domain architecture. **A** The motor domain consists of an N-terminal tail domain (not shown), linker, six AAA domains (namely from AAA1 to AAA6), and a C-terminal domain (not shown). **B** Highlighted AAA1 and AAA2 domains in cytoplasmic dynein-2 structure (PDB: 4rh7) with the ATP biding site circled. **C** Scheme of a single AAA domain and its catalytic residues: Walker A, B, and R finger. Their arrangement in the AAA+ ring make it necessary to assemble two AAA domains to form a functional nucleotide binding site **D** Each AAA domain can be subdivided into large and small AAA domain.

of prokaryotic and eukaryotic genomes contain P-loop NTPases in the protein-coding regions.[109] All AAA+ enzymes have a conserved αβα core domain structure. The five-stranded β sheet is sandwiched between α-helical domains and extended by a less conserved α-helical bundle of four helices (a AAA+ specific feature). For simplicity, the αβα core is called the large domain (or AAAL) and the helical bundle emerging from β5 is called the small domain (or AAAS). The ATP molecule is bound between these two domains of the AAA+ motif.[110] In oligomeric structures ATP is further stabilized by the R-finger of the neighbouring subunit (Figure 3C and D). The AAA+ motif contains between 200 and 250 amino acids, and distinct nucleotide-binding features: Walker A, Walker B, Sensor II, and R-finger (Figure 3D).[111]

The superfamily of AAA+ proteins is a functionally diverse group within the P-loop NTPases. They belong to the group that is characterized by an additional strand between the P-loop strand and the Walker B strand.[112] They drive many processes within the cell, such as protein degradation, vesicular fusion, peroxisome biogenesis, assembly of membrane complexes, in-cell transport, gene regulation, and many more.[113,114,115,110] In all cases there are a well-defined regulatory mechanisms controlling their activity. The AAA+ enzymes are active in a certain oligomeric state, where pairs of subunits interact to form a functional nucleotide-binding site.[18] That binding site will in turn be able to bind and hydrolyse a nucleotide to release a chemical energy and convert it into mechanical force. The AAA+ machine can be formed by association of single AAA+ motifs to form an oligomer (e.g. proteins from the **He**licases and **C**lamp loaders group - HEC), and some AAA+ (such as dynein) can be encoded as a single protein (e.g. proteins from the **P**rote**a**se, **C**helatase, **T**ranscriptional activators, and **T**ransport group - PACTT).[111] Another level of diversity within this family arise from extensions and rearrangements in the protein structure. In dynein those elements are: the N-terminal tail domain emerging from the AAA1; the stalk and MTBD emerging from the AAA4 domain; the buttress of the AAA5 domain; and the C-terminal domain (Figure 3A). In dyneins the N-terminal tail domain and C-terminal motor domain is connected by a linker – the structural element responsible for mechanical force generation. The linker domain can be subdivided into an N-terminal and a C-terminal domain with a cleft in between. The cleft in the linker domain acts as a pivot point that helps the linker adapt various, nucleotide state-dependent conformations. The tail domain is a structure that binds the light chains, dictates the

dynein complex geometry, and uses the linker for force generation. The stalk, buttress, and MTBD form a domain that controls microtubule affinity upon receiving the signal from other AAA domains.

The arrangement of the catalytic residues in AAA+ proteins is well-conserved. The Walker A motif, located between strand β1 and helix α1, has a GX_4GKT/S consensus sequence.[116] The lysine and threonine/serine residues of this motif are believed to bind the β-phosphate of the ATP molecule. The phosphate groups of the nucleotide are coordinated by a divalent magnesium cation.[117,116,118]

The Walker B motif is located on strand β3 and has a consensus sequence ψψψψDE, where ψ denotes a hydrophobic residue.[118] Conservation of the Walker B motif is more variable among AAA+ proteins. The function of the aspartate is to coordinate the magnesium cation and the glutamate carboxyl group acts as a catalytic base that withdraws a proton from the water molecule attacking the ATP γ-phosphate.[119,120,121]

The R finger is a conserved residue located on the N-terminal part of strand β5.[122] In AAA+ proteins that form rings it is believed to be an essential feature in allosteric communication. It points to the ATP active site of the neighbouring motif (γ-phosphate of the nucleotide). Hence, to form an active nucleotide-binding site, at least two AAA+ subunits need to interact, which is why most AAA+ are functional in oligomeric states and form ring-like structures.[123,124,125]

1.2.3 Mechanochemical cycle of dynein

Every dynein consists of six AAA domains of which AAA1-AAA4 are able to bind ATP.[126,127] Dynein motility relies on ATP hydrolysis in the AAA1 site which causes the remodeling of the linker to generate the force for the movement along the microtubule and influences the microtubule affinity of the MTBD.[8,9,10,11,12,13] Thus the mechanochemical cycle of dynein can be divided into three main events: ATP hydrolysis in the AAA1 site, linker remodeling, and microtubule affinity change in the MTBD. Upon ATP binding, the MTBD dissociates from the microtubule and the linker bends into the pre-power stroke conformation.[128,129] The MTBD diffusively searches for a new binding site at the microtubule and is able to rebind to the microtubule after ATP hydrolysis. The release of the inorganic phosphate (P_i) induces a tight microtubule binding state and the bent linker switches back to a straight conformation,

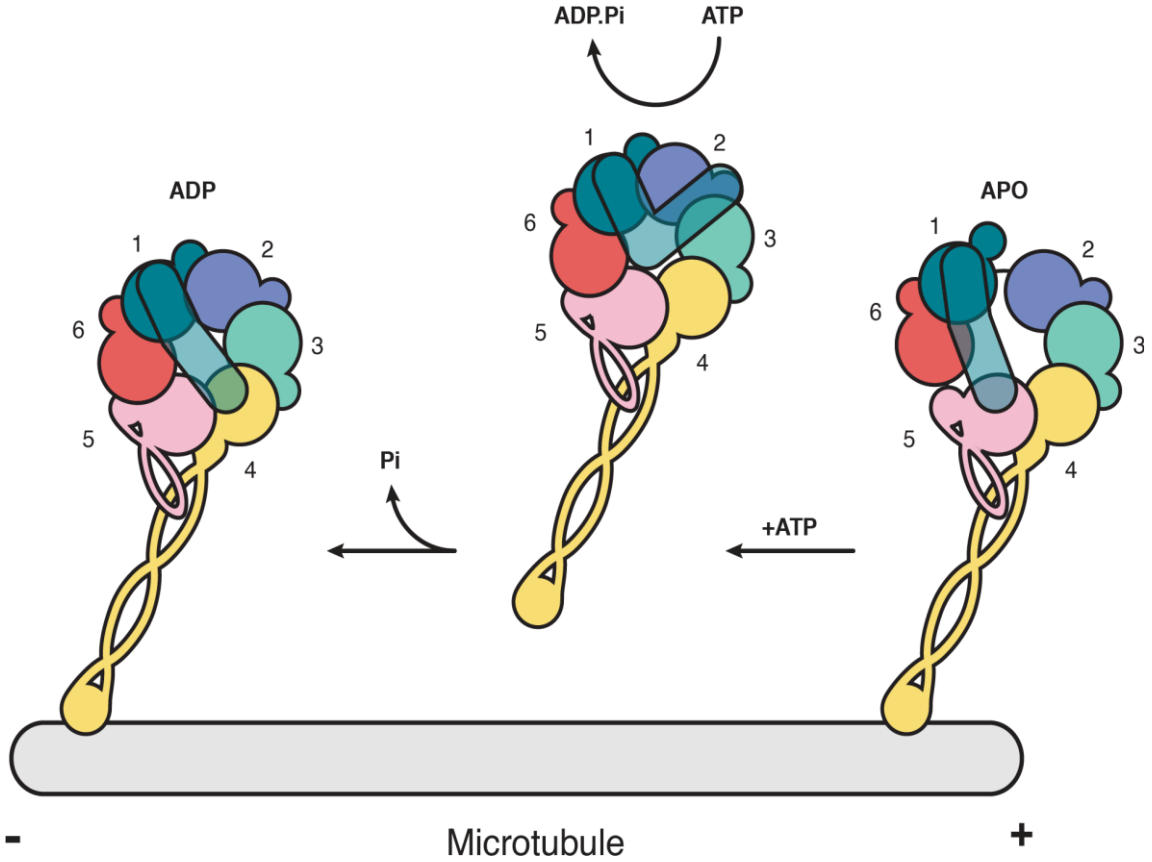

Figure 4. Schematic illustration of dynein's mechanochemical cycle. The APO state (nucleotide-free in the AAA1 domain) adapts a straight linker conformation (right). Upon ATP binding in AAA1 and consecutive hydrolysis into ADP the linker adapts the pre-power stroke conformation (middle) and subsequent release of the inorganic phosphate will cause the actual power stroke and straightening of the linker into its original state (left). Release of ADP will resume the cycle all over again. The change in MTBD microtubule affinity is controlled through the coiled-coil registry shifts in the stalk, which carries the MTBD. The ATP binding to the AAA1 site induces a registry shift in the stalk supporting the low microtubule affinity conformation of the MTBD. After ATP hydrolysis, the stalk registry shift is reversed, which supports the high microtubule affinity conformation of the MTBD and allows the tight binding to the microtubule.[251,252]

the power stroke which generates force to move the dynein forward (Figure 4). The cycle is finalized with the release of ADP.

1.2.4 Dynein-1 and dynactin architecture

Human dynein-1 forms a large 1.4 MDa complex.[130] It has six components, which are present in two copies. There is one isoform encoding the dynein heavy chain (DHC, gene: DYNC1H1), and two isoforms for each of the additional five accessory chains: intermediate chains (IC, encoded by DYNC1IC1 and DYNC1IC2), light intermediate chains (LIC, encoded by DYNC1LI1 and DYNC1LI2), and the three light chains (Roadblock - encoded by DYNLRB1 and DYNLRB2, LC8 - encoded by DYNLL1 and DYNLL2, and Tctex - encoded by DYNLT1 and DYNLT3). The architecture of the dynein-1 complex is presented in Figure 5A. The dynein heavy chain has a molecular weight of 532 kDa (4643 amino acids) and can be divided into an N-terminal tail domain that binds the accessory chains, and the C-terminal motor domain which generates force.

The accessory chains associate with the heavy chain tail domain as homodimers. The intermediate chain (IC, 73 kDa) binds to the N-terminal helical bundles of the tail via its WD40 domain and the largely disordered N-terminal part (~200 AA's). The disordered part of IC also interacts with the light chains Robl (11 kDa), LC8 (10 kDa), and Tctex (11 kDa). The light intermediate chain (LIC, 56.5 kDa) binds to the C-terminal part of the tail domain.[131,132] The LIC is also able to interact with cargo adaptors via its C-terminal region.[133,134,135]

Dynactin is a multi-subunit 1.1 MDa protein complex that is required for dynein motility (hence the name dynactin).[136] Structurally it is made of an actin-like filament of eight α-centractin protomers (ARP1, encoded by ACTR1A and ACTR1B) and a single copy of β-actin (encoded by ACTB). The ARP1 filament is capped on the barbed end by the F-actin protein CAPZ (encoded by CAPZA1 or CAPZA2, and CAPZB), and on the pointed end by ARP11 (encoded by ACTR10), p62 (DCTN4), p27 (DCTN6), and p25 (DCTN5). The dynactin shoulder part emerges from ARP1 closer to the barbed end. It is made of two copies of p150Glued (DCTN1), four copies of p50 (DCTN2), and two copies of p25 (DCTN3). The dynactin assembly scheme is shown

in Figure 5C. The p150Glued N-terminus is a long, flexible coiled-coil which has been reported to interact with microtubules.[137]

1.2.5 Dynein-2 architecture

Dynein-2 is a motor protein complex transporting cargo along microtubules within cilia. Recent years have brought a lot of information about dynein-2, revealing significant differences from dynein-1 and addressing many long-standing questions about its motility, structure, and assembly.[4] The fully assembled dynein-2 complex is made of 16 copies of at least 8 different proteins. Similarly to dynein-1, the N-terminal part of the heavy chain encodes the tail domain, which acts as a dimerization scaffold and binding site for accessory chains.[34,138] The C-terminal part of the dynein-2 heavy chain encodes the force generating AAA+ motor domain.[14]. The N-terminal part of the heavy chains provides a scaffold for binding of the accessory chains: intermediate chains, light intermediate and light chains. Although the overall composition of the complex appears similar to dynein-1, most of the proteins are unique to dynein-2 and have a different nomenclature (Figure 5B).[139]

The accessory chains in dynein-2 are well-known by now, but their individual function in the dynein-2 activities remain unclear. The light intermediate chain 1 (DYNC2LI1) binds to the end of the tail domain and has complex-stabilizing properties.[140,106,141,142,143,144,34] The tail domain of dynein-2 forms a highly asymmetric structure even though in mammals it is made of two identical heavy chain copies.[4] This asymmetry of the heavy chain tail is enforced by unconventional sub-complexes of the intermediate and light chains. While in dynein-1 all accessory chains form homodimers, this is not the case for dynein-2. Its intermediate chains form a heterodimer consisting of the WD repeat-containing proteins 34[145,139,146,147] and 60[139,148] (namely WD43 and WD60). The WD proteins contain a C-terminal β-propeller domain which binds the very N-terminal part of the dynein-2 tail. Also, the dynein-2 complex has different stoichiometry and symmetry compared to dynein-1. The subunit copy number varies from one to six where the intermediate chain N-terminal domains are held together by light chain dimers of roadblock (DYNLRB), three LC8 light chain (DYNLL) dimers, and a dimer of two different Tctex proteins (namely Tctex-type protein – DYNLT, and Tctex1 domain containing-protein (TCTEX1D2).[4,139,138,149]

Interestingly the intermediate chains have different binding partners within the dynein-2 complex. Based on co-expression studies, WD34 interacts with LC8 and roadblock, while WD60 preferentially interacts with the Tctex heterodimer.[138] This unique architecture and composition has implications in dynein-2 motility and recruitment of the IFT particles (Figure 5D).[4]

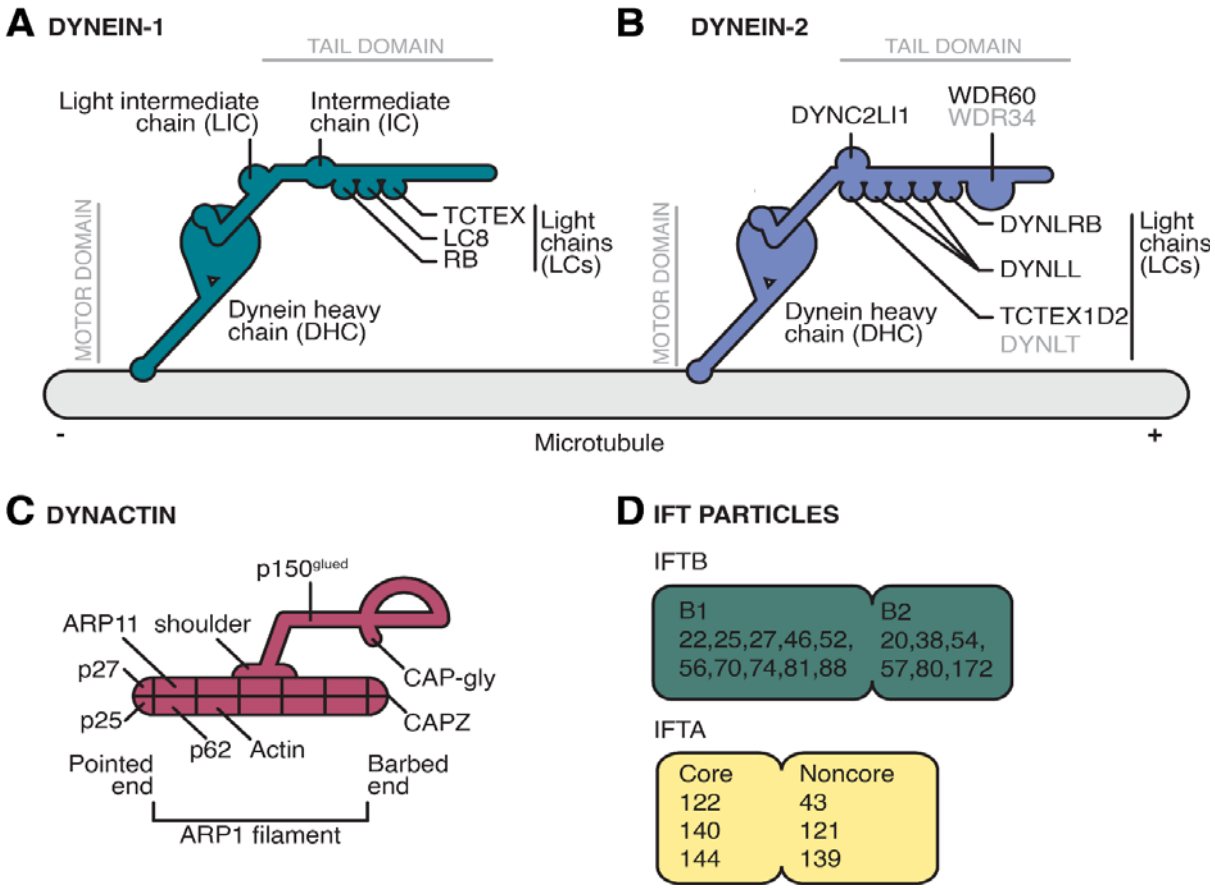

Figure 5. Architecture of the cytoplasmic dyneins and their main interactors. **A** Cytoplasmic dynein-1 heavy chain along with five accessory chains. **B** Cytoplasmic dynein-2 heavy chain with seven accessory chains. The units marked in grey means that they are involved in heterodimer formation in the fully assembled dynein-2 complex. **C** Architecture of the multi-subunit dynein activator dynactin. **D** IFT particle A and B composition.

1.3 Cargo adaptors

1.3.1 Dynein-activating cargo adaptors

Cargo adaptors are usually extended, flexible proteins that share several properties. They are required for dynein motility. Structurally they are characterized by α-helices forming extended coiled-coils and functionally each of them has the ability to interact with multiple protein partners. Generally, the N-terminal region of the cargo adaptor associates with the dynein motor protein while the C-terminal domain recruits cargos. Cargo adaptors of dynein-1 mainly interact with the LIC. An illustrated domain organization and length of these adaptors is presented in Figure 6. Selectivity towards their respective cargos is achieved by adaptor-specific cargo binding mechanisms.[134,135,150] These mechanisms include association with the cargo via conserved motifs, domains, and/or protein modifications. Our knowledge of the molecular bases of cargo recruitment is very limited. Currently there are eleven mammalian dynein cargo adaptors known, but the number is continuously growing.[151]

The best studied family of dynein-1 cargo adaptors are the BicD proteins. BicD was first identified in Drosophila, because mutations in this gene caused double abdomen development - the bicaudal phenotype, hence the name BicD.[93] Mammals have two BicD orthologues, BicD1 and BicD2, with multiple isoforms and molecular weights in the 100 kDa range. BicD's form a homodimer and, based on secondary structure predictions, they tend to fold into three coiled-coil domains (CC1, CC2, and CC3). Each CC domain plays a role in higher-order complex formation. For the N-terminal coiled-coil domain, CC1, it was shown that it is able to bind dynactin and dynein via the ARP1 subunit of dynactin and the N-terminus of the dynein heavy chain[152,132]as well as LIC1.[134,133] These multiple interactions increase the affinity of the dynein for dynactin and are required for stable dynein/dynactin/BicD2 complex (DDB) formation.[33,153,154] It was also shown that the N-terminal region of BicD2 alone is able to induce DDB complex formation with higher efficiency than the full-length protein.[155] BicD2 has the tendency to bind two dyneins and one dynactin for processive movement.

The C-terminal domains of BicD's (CC2 and CC3), are usually implicated in cargo recruitment. The BicD1 C-terminal CC3 domain can interact with GTP-bound RAB6A and B[156,157,158,159,160] and cytomegalovirus/HHV-5 protein UL32[161]. BicD2 is able to recruit RAB6A[162], NEK9[163], DNAI1[164,165], RANBP2[166], and kinesin KIF5A[166].

Cargo adaptors of the BicD family also interact with themselves. It has been observed by several groups that the C-terminal part is able to make contact with the N-terminal part leading to an autoinhibited state in BicD1[167] and BicD[168,169]. There is little known about human BicD2 autoinhibition and many features are assumed to be common with better-studied Drosophila BicD orthologue.[170171] It has also been suggested that the autoinhibited state can be relieved by cargo binding.[168,172,173,170] There is evidence for cargo-induced autoinhibition release for Drosophila BicD in the case of Egl and mRNA cargo.[170] So far no such studies have been done for either BicD1 or BicD2.

The BicDR family is closely related to the BicD2 cargo adaptor family. There are two mammalian orthologues, BicDR1 and BicDR2, which have half the size of BicD2, but share a very similar domain organization. They have three CC domains, dimerize and bind dynein/dynactin. Interestingly, BicDR1 can recruit four dyneins and one dynactin which increases the speed and force of the motor complex.[131,174,175]

Another family of dynein cargo adaptors are the Hook proteins. There are three orthologues in mammals, Hook1, Hook2, and Hook3, and they are believed to operate similarly to the BicD family. They are made of three domains: the N-terminal hook domain; a coiled-coil domain driving dimerization of the protein; and C-terminal random coil domain that mediates cargo binding.[176,133,131] Hook1 and 3 have the ability to induce longer and faster dynein-dynactin runs than BicD2.[135,131,177] Hooks associate

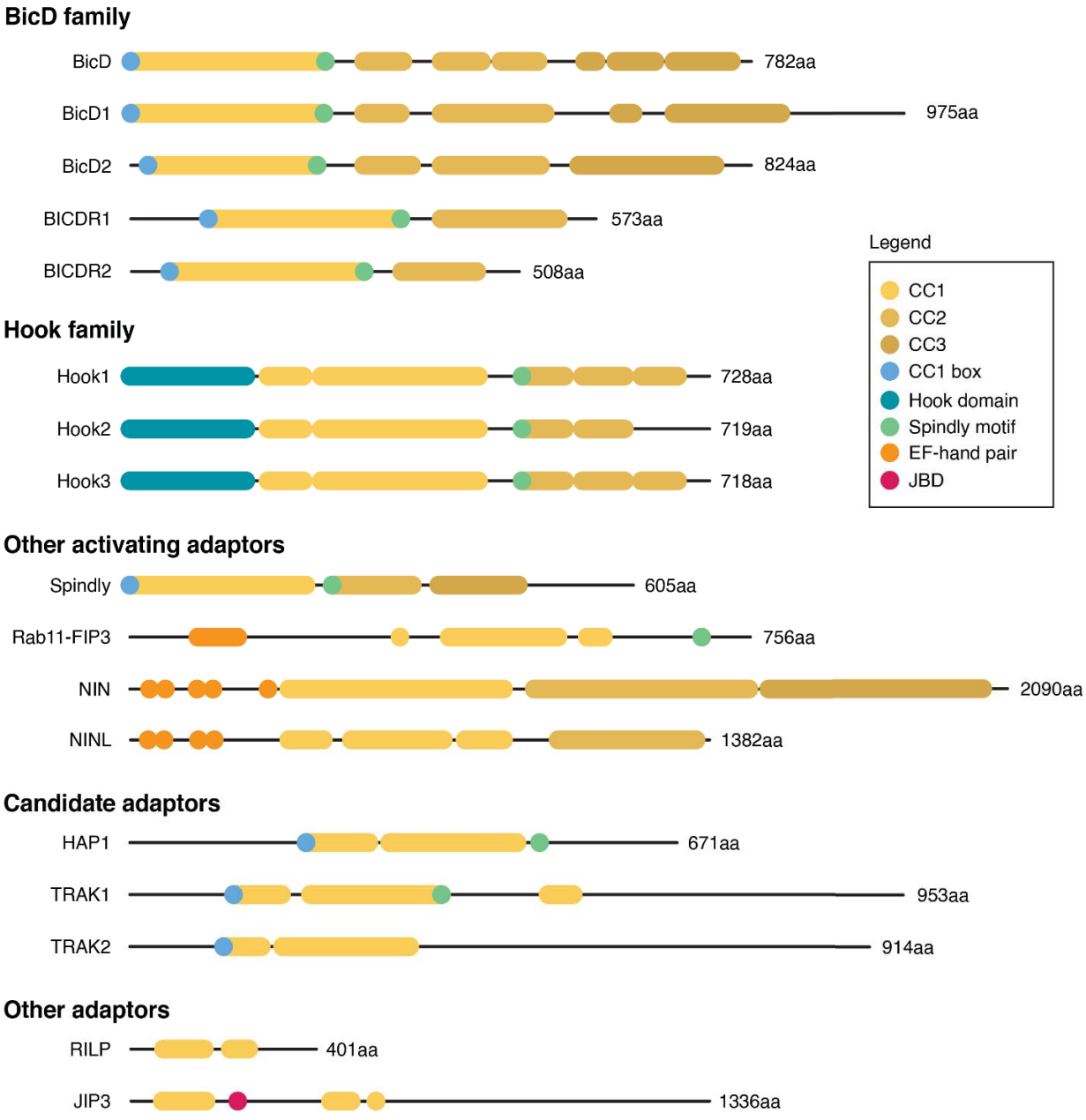

Figure 6. Schematic illustration of known dynein-1 cargo adaptors with highlighted domains and interacting sites. All adaptors drawn to scale except for NIN, NINL and JIP3.

with dyneins similarly to BicD2 as they bind to LIC1 via its N-terminus. This interaction induces processive dynein motility in vitro and in vivo.[133,177,135] Similarly to BicDR1, Hook3 has been shown to recruit a team of two dynein dimers per one dynactin.[131] Hook1 and Hook3 are involved in endosomal trafficking pathways,[178,179,180,176,181] while Hook2 is thought to operate at the centrosome and during mitotic progression.[182,183,184,185] Hook1 has also been reported recently to associate with TrkB-BDNF-containing complexes in neurons.[186]

Another known dynein activating cargo adaptor is Spindly. It is required in mitosis to silence the mitotic checkpoint and localize dynein and dynactin to the mitotic kinetochore.[32,187,188,189] This induces end-on kinetochore-microtubule attachments mediated by the NDC80 complex and subsequent chromosome movements to the pole.[188,190,191] Spindly shares two features with other cargo adaptors: the CC1 box

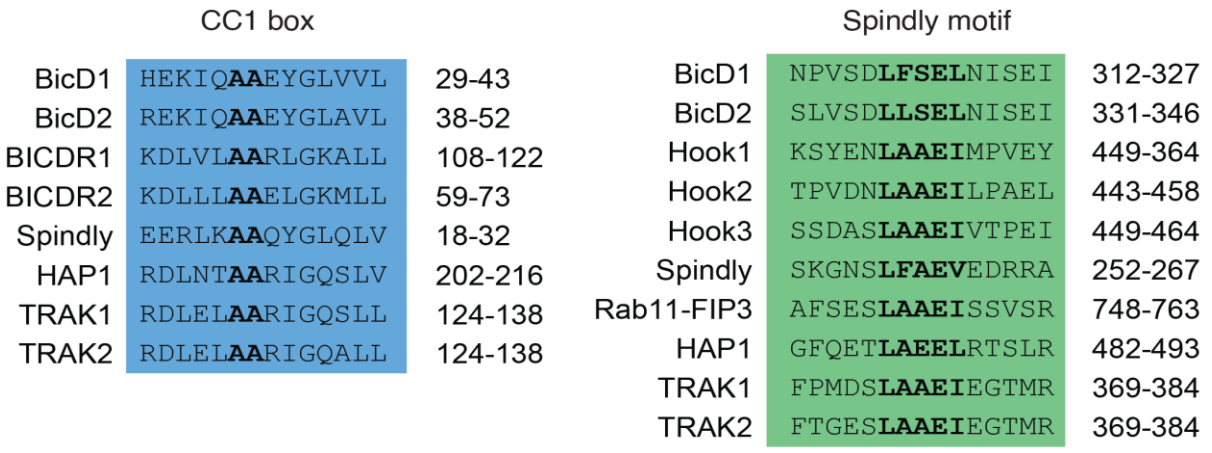

Figure 7. Sequence alignment of the CC1 box and spindly motif of selected cargo adaptors.

motif and Spindly motif (Figure 7).[150] The CC1 box motif is an N-terminal motif in BicD cargo adaptors that mediates the interaction with the dynein LIC1.[133] The BicD and Spindly mechanisms of dynein binding are believed to be similar, because mutating the two conserved alanines of the CC1 box to valine residues in BicD and Spindly results in a loss of the interaction with dynein and dynactin in vitro.[175]

The motif that enables cargo adaptors to interact with the pointed end of dynactin is conserved and named the spindly motif (L(F/A)xE), because it was first identified in the Spindly cargo adaptor.[189] It is located between the first and the second coiled coil domain in most of the adaptors. It is not precisely known how this interaction is mediated at a molecular level. Mutating the phenylalanine into alanine in Spindly causes its dissociation from dynactin, but in other adaptors the same residue is actually an alanine (e.g. BicDs).[150] This suggests that dynein-dynactin-cargo adaptor assembly might occur via different mechanism depending on the cargo adaptor and cellular context.[150] Despite the divergent dynactin binding mechanism, the described adaptors have three main features in common: an N-terminal CC1 box or Hook domain mediating the interaction with LIC1; a coiled-coil domain (~30nm) sandwiched between the dynein tail and dynactin; and a spindly motif at the C-terminus of the coiled-coil domain.

Another, less characterized and discussed dynein cargo adaptor is Rab11-FIP3. It shares the dynein-binding N-terminal properties found in BicDs, Hooks, and Spindly and is able to activate dynein motility.[32] Rab11-FIP3 is involved in movement of peripheral endosomes along microtubules towards the MTOC/centrosome generating endosomal recycling compartment (ERC)[192], and has been implicated in dendrite formation through trafficking of Rab11- and Arf6-dependent endosomal transport.[193,194]

The last group of cargo adaptors described here are the largest representatives of the dynein-dynactin interactors: ninein (NIN) and ninein-like proteins (NINL). They have been identified as cargo adaptors through BioID MS.[195] These large coiled-coil proteins share a similar secondary structure with other cargo adaptors but they also contain EF-hand domains similar to the Rab11-FIP3 protein. The EF-hand domain has a helix-loop-helix architecture and its name comes from the thumb and forefinger-like shape of the motif in which a Ca^{2+} ion is coordinated by the loop region. Ninein localizes to the appendages of mother centrioles[196] where it supposedly anchors centrosomal microtubules.[197,198] It has been shown in mice that ninein re-localizes from centrosomes to the apical surface during differentiation of epithelial cells.[196] It also has been observed that a re-localization targeting desmosomal junctions can take place during differentiation of stratified epithelial cells in the epidermis.[199] The loss of ninein in zebrafish leads to impairment of brain and skull development,[200] and the loss of ninein-like cargo adaptors causes delocalized trafficking patterns of cilia directed cargo (Rab8a) and defects in melanosome transport.[201,202]

1.3.2 Candidate cargo adaptors

There are a number of proteins that share the domain organization with the activating cargo adaptors. They have been suggested to be involved in dynein motility, but their dynein motility-enhancing properties have yet to be confirmed. The first protein is huntingtin-associated protein 1 (HAP1). As its name suggests HAP1 associates with huntingtin and their involvement in Huntington's disease is known.[203] HAP1 can interact with the p150 subunit of dynactin[204,205] as well as kinesin light and heavy chains,[206] which strongly suggests its role in intracellular transport. HAP1 is required for autophagosome huntingtin-mediated transport and amyloid precursor

protein (APP) trafficking.[207] Huntingtin has been linked to the vesicle transport in axons. It has been suggested that huntingtin and HAP1 can act as at scaffold for dynein and kinesin association with vesicles.[208,209,210,211,212]

Another group of candidate cargo adaptors are mammalian TRAK proteins, first identified in drosophila under the name Milton.[213] It has been observed that knockdown of Milton causes a reduction in retrograde transport velocities in axons, but does not significantly affect the anterograde transport. Moreover, mutations in Milton caused the absence of mitochondria in photoreceptors, wing nerves, and motor axons.[214,215,213] Taken together, this suggests that Milton is involved in mitochondria positioning. In rat hippocampal neurons the mammalian homologues of Milton, TRAK1 and TRAK2, are localized in axons and dendrites respectively.[216,217] Consistently with these observations, TRAK1 impairment leads to the reduction of mitochondrial mobility in axons, while TRAK2 defects cause reduced mitochondrial mobility in dendrites.[218] The most recent models describe TRAK1 and TRAK2 as regulators of dynein and kinesin-1 activity to move mitochondria in axons and dendrites.[217] Structurally Milton and TRAKs have an N-terminal coiled-coil domain and a C-terminal cargo interaction region. The cargo protein for Milton and TRAKs is the mitochondrial rho GTPase Miro - an outer membrane protein containing two GTPase domains and two EF hand domains.

1.3.3 Other adaptors

The last group of putative dynein activating adaptors are the RILP and JIP proteins. They fall into the ‘other adaptors’ category for two reasons: they haven’t been shown to activate dynein in vitro or in vivo, and structurally they do not resemble other adaptor proteins.

Rab7-interacting lysosomal protein (RILP) has been speculated to bind to Rab7-containing vesicles, which include late endosomes and lysosomes.[219,220] The recruitment of dynein by RILP takes place in a stepwise fashion. RILP and ORP1L (oxysterol-binding protein-related protein 1L) associate into a complex with the Rab7 GTPase which enables RILP to recruit the p150 subunit of dynactin. This event, in turn, will facilitate dynein and vesicle recruitment.[221] It has been further proposed that

dynein complex formation in this particular pathway can be regulated by cholesterol levels in a ORP1L-dependent manner.[151]

Four mammalian JNK-interacting protein (JIP) proteins have also been identified as potential dynein cargo adaptors, JIP1, 2, 3, and 4.[222,223,224] Despite the dynein context, each JIP contains a JNK kinase domain close to the N-terminus, which facilitates the binding of JNK and p38 kinases, which are involved in cell growth, differentiation, and apoptosis. All of the JIPs have been reported to also bind kinesin-1.[225,226,227,228] JIP3 and JIP4 have been shown to interact with dynein-dynactin via their N-terminal coiled-coil domains.[224] The Drosophila JIP3 homolog, Sunday Driver, was shown to interact with dynein-dynactin during axonal JNK-injury signalling.[229] JIP3-deficient mice, zebrafish, and C. elegans have shown lysosomal accumulation and maturation issues.[230,231,232] JIP4 on the other hand was shown to interact with kinesin-1 and dynactin to transport recycling endosomes during cytokinesis in an ARF6-dependent manner.[227]

1.4 Structural studies of the cytoplasmic dyneins

Dyneins have attracted a lot of attention in the past years with the recent developments in cryoEM. Structural techniques helped us to see how dynein operates in the context of microtubules,[1,2,3] IFT trains,[4,5] dynactin and cargo adaptor complexes,[6] and mammalian axons.[7] Despite these structural advancements there are still many fundamental questions about dynein motor activity and its cargo binding mechanisms. It is not known how the mechanochemical cycle of dynein induces the linker remodeling to generate force. It is unclear how dynein achieves cargo adaptor binding specificity and how it recruits the actual cargo. These are the main questions that I wanted to address in this thesis. In Project 1 I used the dynein-2 motor domain as a model to study the role of the ‘inserts’ and their role in linker remodeling. These inserts have already been observed to play a role in dynein’s power stroke but have never been described structurally. In Project 2 I wanted to reconstitute and study the fully assembled dynein complex with dynactin, cargo adaptor, and cargo. It has not been shown that such complexes can be reconstituted in vitro. Such methodology would significantly advance our understanding of dynein motility, activation, and cargo recruitment.

1.4.1 Project 1: Contribution of the secondary structure elements to the dynein motor linker remodeling

The movement of dynein along microtubules requires cyclic microtubule attachment and detachment while generating force. Dyneins generate force for the movement by hydrolyzing ATP in its AAA+ ring which contains four nucleotide binding sites. The AAA1 site is responsible for force generation and MTBD microtubule affinity regulation.[8,9,10,11,12,13] The nucleotide-dependent motor domain dynamics can be divided into several states. In the APO state, the AAA+ ring is a wide open ring and the linker adopts the straight, post power stroke conformation and the MTBD-microtubule affinity is high. Upon ATP binding in the AAA1 domain, the AAA+ ring closes, the MTBD dissociates from the microtubule, and linker adapts the bent pre-power stroke conformation where its central cleft acts as a pivot point (Figure 8B). Once the ATP hydrolyses into ADP and phosphate has occurred, dynein rebinds the microtubule, which reopens the AAA+ ring and stimulates linker straightening – the force producing power stroke. After the ADP is released from the AAA1 site the motor is ready for another ATP hydrolysis cycle and a consecutive step on the microtubule.

The nucleotide state dictates the linker position with respect to the AAA+ ring. In the absence of the nucleotide (APO) the linker tip is docked onto the AAA5 domain. During ATP binding and hydrolysis (pre-power stroke) the linker tip is docked at the interface of the AAA2 and AAA3 domains. After the power stroke and P_i release the linker straightens back and docks onto the AAA4 domain. Further shifting of the linker N-terminus towards AAA5 induces the AAA+ opening and release of the ADP from the AAA1 site. The nucleotide-dependent linker remodeling is the key element in the dynein mechanochemical cycle.[8] So far, several nucleotide states have been structurally described: AMPPNP,[15,16] ADP,[17] and ADP.V_i.[14] While we have some structural snapshots of the dynein motor in different nucleotide states, it remains largely unknown how the AAA+ ring actually supports linker remodeling. It has been suggested that certain secondary structure elements in the AAA+ ring might be responsible for the linker remodeling.[14] These elements are called ‘inserts’ and are present in the AAA1-5 domains of dynein. The inserts are made up of α-helical or β-hairpin extensions of the basic α/β AAAL fold and reside on the linker face of the AAA+ ring. Their location within the dynein motor domain is shown in figure 8A. The inserts also have specific nomenclature which specifies their location in the AAA domain. The H2 insert is a β-hairpin that emerges from the H2 helix of the AAA domain. It often

points at the center of the AAA+ ring to interact with the substrate in some AAA+ proteins. Pre-sensory insert I (PS-I) is an insertion between helix 3 and strand 4 of the AAA domain.[18]

It has been speculated that the AAA4 PS-I insert might cause a steric clash with the linker N-terminus upon ATP-induced AAA+ ring closure[19] to trigger linker bending. Also, the PS-I and H2 inserts of the AAA2 domain have been implicated in linker remodeling. It has been suggested that they interact with the pivot point region in the linker domain to participate in linker remodeling.[17] None of these hypotheses have been structurally verified so far. I wanted to structurally evaluate the contribution of these elements to linker remodeling. The dynein-2 motor domain is an excellent model system for studying the contribution of inserts because there is a little to no interference of nucleotide hydrolysis in the other domains: the AAA3 domain lacks the catalytic residues;[16,20] the AAA4 domain is poorly conserved; and the AAA5 and 6 domains have no nucleotide binding sites. Because of that I chose dynein-2 in my studies and set myself the following aims:

1. Production of recombinant human dynein-2 motor domain: WT, ΔAAA2 PS-I and H2, and ΔAAA4 PS-I;
2. High-resolution cryoEM study of these deletions and evaluation of their influence on the motor domain and linker behavior.

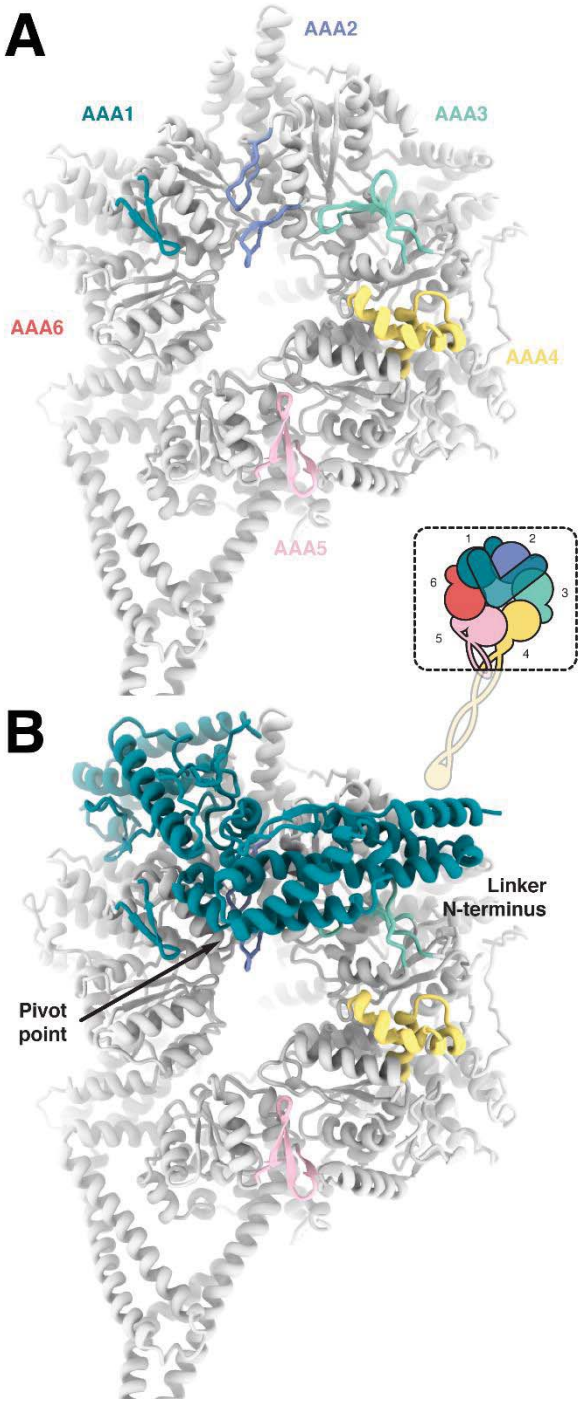

Figure 8. A Location of the inserts in the dynein-2 AAA1-5 domains, PDB: 4rh7 (linker domain removed for clarity reasons). **B** Dynein-2 motor domain with highlighted linker pivot point and the N-terminal part.

1.4.2 Project 2: Structural studies of the dynein complex involved in the neocortex development

The neocortex is a mammal-specific brain tissue associated with higher cognitive abilities. In the adult brain, it consists of six layers.[21] Each layer contains pyramidal neurons of a specific subtype that are generated from the apical radial glial progenitor cells (RGPCs) located in the ventricular zone. The RGPCs in the ventricular zone divide to generate neurons that migrate along the RGPCs from the ventricular zone to the cortical plate where they differentiate into pyramidal neurons. The division of RGPCs to generate intermediate progenitors is driven by the RGPC mitotic cycle, which is tightly linked with oscillatory movements of their nuclei, a phenomenon that is also known as interkinetic nuclear migration (INM).[22] In the G1 phase of the cell cycle, the nucleus moves from the apical to the basal side of the ventricular zone. Once the nucleus has reached the basal side, the RGPCs enter the S-phase. In the following G2-phase, the nucleus moves back to the apical side of the ventricular zone, where the cells undergo mitosis to generate the intermediate progenitor cells that move into the cortical plate of the neocortex to differentiate into neurons. The movement of these intermediate progenitor cells from the ventricular zone to the neocortex is guided by the RGPCs, which laterally traverse across the whole neocortex. The schematic illustration of the INM and RGPC-guided neuron migration is shown in Figure 9. The biological function of interkinetic nuclear migration in RGPCs is not well understood. It has been speculated that it might allow the packing of a large number of RGPCs within a limited space, thereby boosting the number of intermediate progenitors that can be generated at the ventricular zone.[22] Due to the INM, the position of the nuclear bulge varies between neighboring RGPCs, which allows tight packing of neighboring cells. While the biological purpose of INM in RGPCs is still under debate, its importance for the development of the mammalian brain is reflected by several neuropathologies such as lissencephaly (smooth brain phenotype) and microcephaly (reduced brain size phenotype).

Early studies have established that the INM process is dependent on microtubules as well as microtubule-associated motor proteins.[23,24,25] The microtubule (+) end-directed motor protein Kif1a, a member of the kinesin motor protein family, transports nuclei during the G1 phase of the cell cycle to the basal side of the ventricular zone, where the microtubule (+) ends cluster.[24] The microtubule (-) ends in RGPCs cluster at the apical side of the ventricular zone. Consequently, the movement

of nuclei from the basal back to the apical side during the G2-phase is driven by dynein, a microtubule-associated motor protein that transports cargo towards the (-) end of microtubules.[25] The dynein-driven apical nuclear movement is believed to proceeds in two phases. In the first phase, dynein together with its ubiquitous activator dynactin is recruited to the nucleus through an interaction with the nuclear pore component RanBP2 under participation of the scaffolding protein BicD2.[25,26] The second phase is controlled by the nuclear pore component Nup133 that binds to CENP-F which recruits dynein/dynactin via the proteins NudE and Nudel.[25,27,28] Synchronization of these nuclear movements with the G2 phase of the cell cycle is achieved via the activity of the mitotic kinase CDK1. CDK1 phosphorylates RanBP2 which in turn binds BicD2. BicD2 recruits dynein/dynactin[27] to drive the first phase of ventricular nuclear migration. The second phase of RGPC apical nuclear migration involves the CENP-F key player, which resides inside the nucleus until late G2. In this case, the activity of CDK1 is needed to relocate CENP-F from the nucleus to the cytosol so that it can bind to Nup133 to initiate the second phase of apical RGPC nuclear migration.[27] The reason for two separate dynein recruitment pathways during apical RGPC migration is not clear at the moment. It has been speculated that the late CENP-F pathway might allow better coordination between the mitotic cycle and the arrival of the RGPC nucleus at the apical side of the ventricular zone. CENP-F leaves the nucleus at about the same time Cyclin B enters it, which could ensure that centrosome separation, nuclear envelope breakdown, and kinetochore assembly are coordinated with the CENP-F mediated final nuclear migration steps to the apical side of the ventricular zone.[27]

There is also strong experimental evidence that the dynein regulator Lis1 is involved in RGPC nuclear migration. SiRNA mediated knockdown of Lis1 in the developing embryonic rat brain almost completely abolished the oscillatory nuclear migration in RPGCs.[23] This effect can be explained by the ability of Lis1 to induce a strong, more force resistant microtubule binding state in dynein[29], which might be needed when dynein transports large cargos, such as nuclei.

Disturbances in the RanBP2 and Nup133 mediated dynein recruitment pathways lead to arrested RGPC nuclei that fail to reach the apical side of the ventricular zone and as a consequence do not undergo mitosis with devastating consequences for neocortex development.[30,23,31]

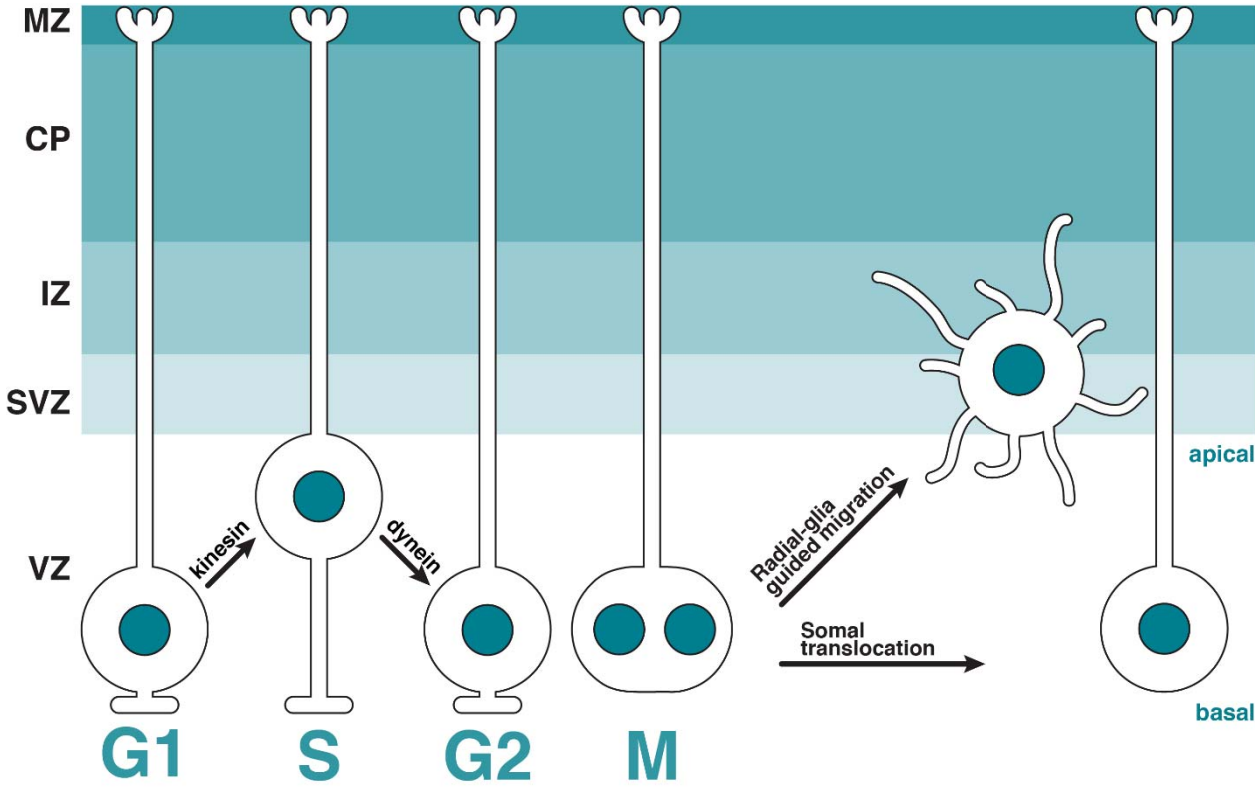

Figure 9. An illustration of the INM process within the ventricular zone (VZ) of the neocortex. Upon mitosis completion the freshly formed progenitor cells will differentiate into various types of neurons and populate the cortical plate through radial-glia guided translocation or somal translocation.

The structural basis of dynein-driven RGPC nuclear migration remains unknown despite its well-established importance in neocortex development. It is not known how the nuclear pore component RanBP2 recruits the dynein complexes to promote RGPC nuclear migration. In addition to the recruitment, the motor activity of dynein has also to be activated. Dynein exists in an auto-inhibited state that is only overcome when it binds to a cargo adaptor and dynactin.[32,33,34,35] For cargo complexes involving BicD2, as in the case of the RanBP2 recruitment pathway, a potential activation mechanism has recently been suggested.[35] Unfortunately these hypotheses were derived from experiments on truncated BicD2 and/or Drosophila BicD. To investigate the important question of RanBP2-mediated dynein recruitment and activation, I set myself the following aims:

1. Recombinant production of biochemically active, full-length human BicD2;
2. Reconstitution and structural studies of the BicD2-RanBP2$_{BBD}$ complex;
3. High-resolution cryoEM studies of the in vitro reconstituted DDBR2 complex;

The major part of this work has been published in the manuscript entitled “In-vitro characterization of the full-length human dynein-*1 cargo adaptor BicD2”.* All additional experiments supporting this work are described in the result section (following the manuscript).

RESULTS

Structural Studies on Dynein Linker Remodeling

2. Results: Structural Studies on Dynein Linker Remodeling

Dynein movement depends on ATP-dependent linker remodeling.[8] The chemical energy generated in the AAA1 domain is converted into a mechanical remodeling of the linker by adapting pre- and post-power stroke conformations.[19] There are a few high- and medium-resolution structures of the dynein motor domain in these conformations but it remains unclear how linker remodeling is induced and regulated. The size and complex architecture of dynein makes its mechanochemical cycle less understood compared to other motors.

There are reports of secondary structure elements in the motor domain that have an influence on the linker's behaviour.[10,14] These elements are called 'inserts' and they are present in dynein's AAA1-5 domains. Among the inserts of the AAA+ ring, the AAA2 and AAA4 inserts have been speculated to be involved in linker remodeling.[14] The H2 insert of AAA2 has been suggested to contact the central linker cleft to induce linker remodeling upon ATP hydrolysis in AAA1.[10,14] The α-helical PS-I insert of AAA4 is speculated to induce linker remodeling via a steric clash with the linker tip upon ATP-mediated AAA+ ring closure.[14] Location of these inserts within the AAA+ ring is shown in Figure 8A. The contribution of these inserts has not been extensively studied even though it might be of high importance for our understanding of dynein motor force generation. For these reasons I decided to structurally characterize dynein's motor domain behaviour upon deletion of the inserts in the AAA2 and AAA4 domains.

2.1 Expression of the dynein-2 motor domain constructs

For this study I chose to work on the human dynein-2 motor domain because, in contrast to dynein-1, linker remodeling only depends on ATP turnover at the AAA1 domain with no influence from the accessory ATP binding sites, which do not hydrolyse ATP (unpublished data). This suggests that linker remodeling in dynein-2 has no interference with ATP activity in other domains making it a good model system to study insert contribution to linker remodeling with cryoEM. Furthermore there is a 3.3 Å crystal structure of human dynein-2 in the pre-power stroke conformation that I could use as a reference for the comparison with linker remodeling in the AAA2 and

AAA4 insert deletion mutants. For convenience the motor domain will be called dynein-2 in this chapter (the N-terminal tail part was deleted).

I started my work with four plasmids encoding cytoplasmic dynein-2: WT, ΔAAA2 H2 & PS-I, ΔAAA2 H2, and ΔAAA4 PS-I. The exact sequences of AAA2 H2, AAA2 PS-I, and AAA4 PS-I are listed in Table 1. The H2 and PS-I insert in the AAA2 domain were replaced by a GG linker and the PS-I insert in AAA4 was replaced by a GSG sequence. The constructs had already been cloned by my supervisor Dr. Helgo Schmidt when I arrived in the lab. The dynein-2 gene was codon optimized for insect cell expression and inserted into the pFastBac vector. The GOI was N-terminally fused with an 8xHis tag, a ZZ tag (protein A), followed by 2xTEV cleavage sites and GFP.

Table 1. List of dynein-2 inserts in the AAA2 and AAA4 domain considered in this work.

Dynein-2 insert	Sequence	Replaced by	Residues
AAA4 PS-I	GLYTLEELEPLLLPLKDQASQDGFFGPVFNYFTYRI	GSG	2739-2775
AAA2 H2	DMDTREW	GG	2016-2023
AAA2 PS-I	LLTMPSGERIQ	GG	2072-2083

To express these constructs in insect cells, I incorporated the plasmids into the baculoviral genome. I transformed the plasmids into the bacterial DH10MultiBac-CFP, DH10MultiBac-YFP, or DH10MultiBac-mCherry strains. Further stages of bacmid production and subsequent transfection are described in the methods section. Each virus was amplified to at least the P2 generation for test- and large-scale expression of the dynein-2 constructs. A diagnostic SEC run and corresponding SDS-PAGE gel are shown in figure 10. For expression and purification steps refer to the Methods section.

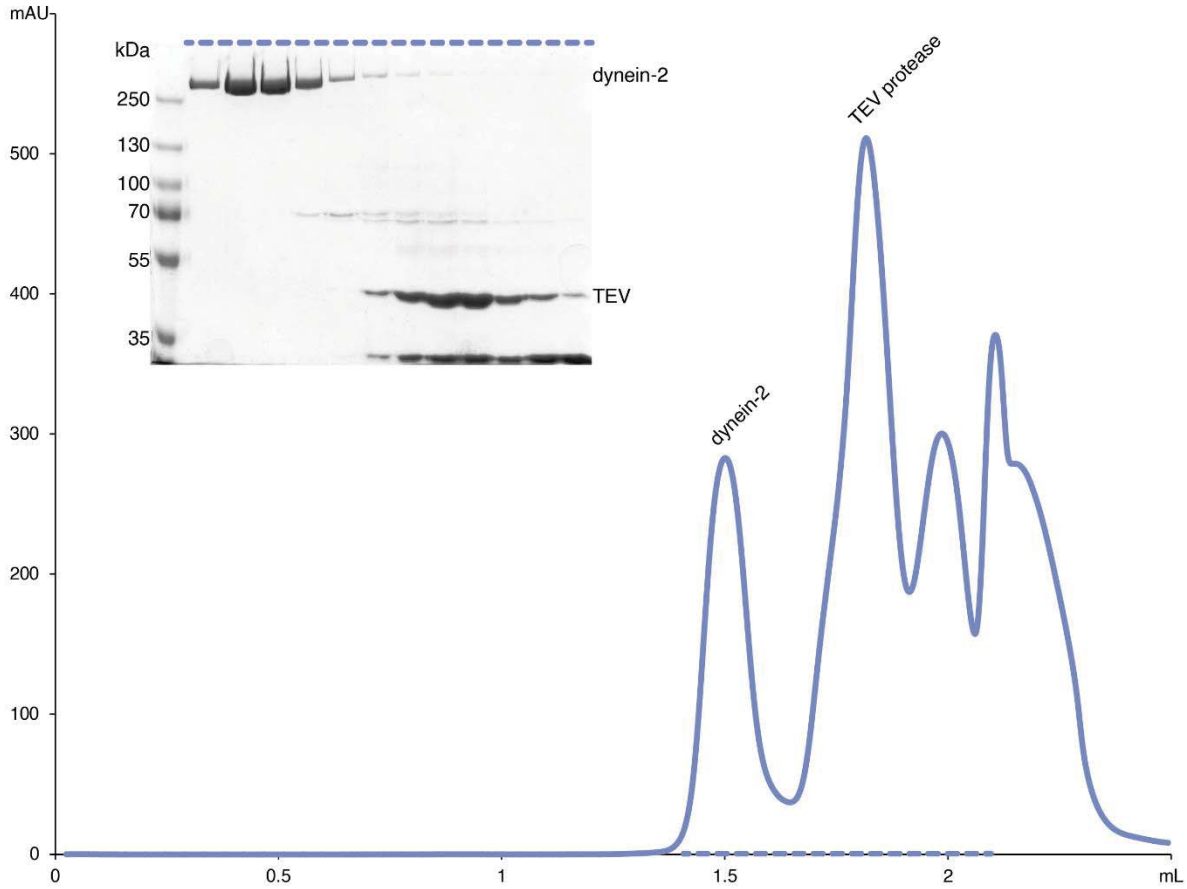

Figure 10. Example of the SEC profile and diagnostic SDS-PAGE gel of the dynein-2 WT after the overnight cleavage with the TEV protease.

2.2 cryoEM data processing of dynein constructs

The data were collected on an FEI Titan Krios (data collection parameters listed in table 2) and processed similarly for all dynein-2 variants. Example of data processing workflow is shown in figure 11 for ΔAAA4 PS-I. The data were collected either on our in-house microscope (WT and ΔAAA4 PS-I) or at the ESRF in Grenoble (ΔAAA2 H2 & PS-I, ΔAAA2 H2, and ΔAAA2 H2). Motion correction and dose-weighting was done with MotionCor2[233] and CTF parameters were set using Gctf.[234] The rest of the processing was done in Relion-2.0.[235] Micrographs were manually examined to remove the low quality images with uncorrected drift, large contamination, astigmatism, or extreme defocus values (<1 μm or >5 μm, except for the phase-plate data where close-to-focus values are acceptable).

Table 2. Data collection parameters for dynein-2 constructs used in this study.

	WT	ΔAAA4 PS-I	ΔAAA2 PS-I & H2
Voltage [keV]	300	300	300
VPP	✓	-	-
Camera	Gatan K2		
Acquisition pixel size	1.09	1.052	1.053
No. of acquired movies	3548	4117	4540
Defocus range	0-1.4μm	0-5.5μm	0-4μm
CTF resolution range	2.37-12.65	2.3-14	2.3-12
No. of picked particles	940,625	1,712,074	1,435,296
No. of particles from 2D classification	344,867	584,020	372,208
Final number of particles	268,642	149,509	171,665
Resolution	4.7Å	3.23Å	4.0Å
Final B factor fitted	-25	-59	-106
Relion version	2.1	3.0.7	3.0.8

For each dataset I picked a small set (1-5k) of particles manually, and subjected them to reference-free 2D classification. The classes representing the motor domain were centered and used as references for autopicking with Gautomatch (K. Zhang, MRC Laboratory of Molecular Biology, Cambridge, UK). The particles were then cleaned through several cycles of 2D classifications and subsequent 3D classification and refinement. For the 3D classification a large and featureless mask was applied to increase the resolution in the AAA+ ring rather than considering the motor domain with stalk and buttress.

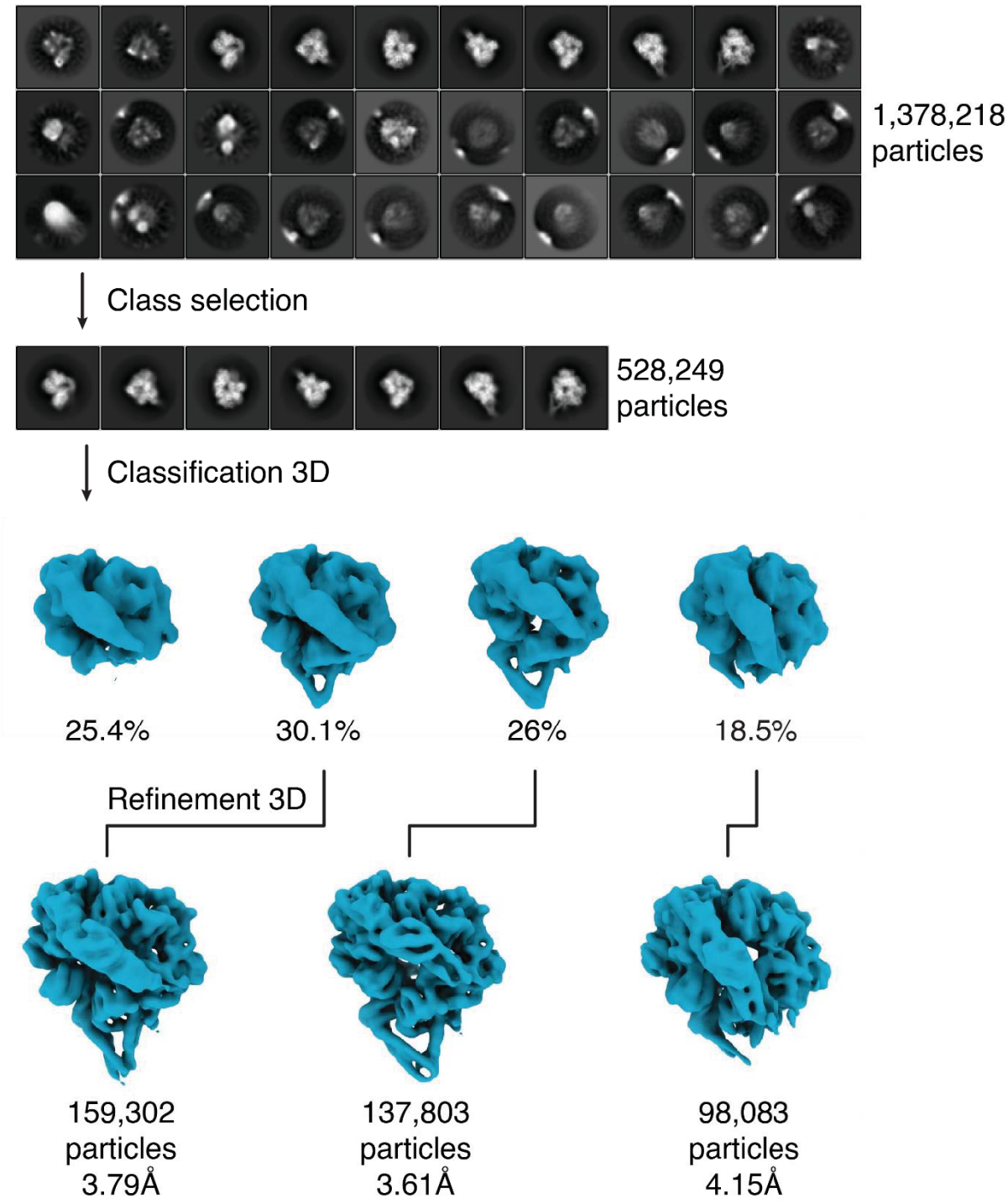

Figure 11. Cryo-EM data-processing workflow for the maps presented in this study. Example on ΔAAA4 PS-I deletion mutant. Other datasets were processed similarly and minor differences were usually in software used for the CTF estimation and/or particle picking. The ΔAAA4 PS-I ADP.Vi map yielded 3.61Å (with Bayesian polishing 3.2Å). Resolutions are for an FSC of 0.143.

2.3 Dynein-2 WT in the ADP.Vi state

At the point when I started my work there were not many cryoEM structures of dynein-2 (either full-length or motor domain) available. For that reason, I decided to prepare the WT dynein-2 and characterize the conformations it samples in the presence of ADP.Vi. From the total ~260k particles, the ADP.Vi reconstruction yielded a 4.8Å density map of the motor domain (Figure 12 A and B). The WT dynein-2 had several projections (Figure 12 C and D) mainly located at the back of the AAA+ ring. The reconstruction allowed me to clearly assign the domains. In my reconstructions there was a relatively even distribution of ADP.Vi (bent linker), ADP (linker associated with AAA4), and APO (linker associated with AAA5) states. This suggests that in presence of the ADP.Vi the motor exists in an equilibrium of states. The density presented in figure 12 B is seen in the ADP.Vi state and the linker is in the pre-power stroke conformation, hence pointing towards AAA2/3. Interestingly the linker tip appears to be more flexible compared to the crystal structure in the same nucleotide state as its density is less defined. This is likely due to the crystal contacts of the N-terminal part of the protein that stabilize the conformation.

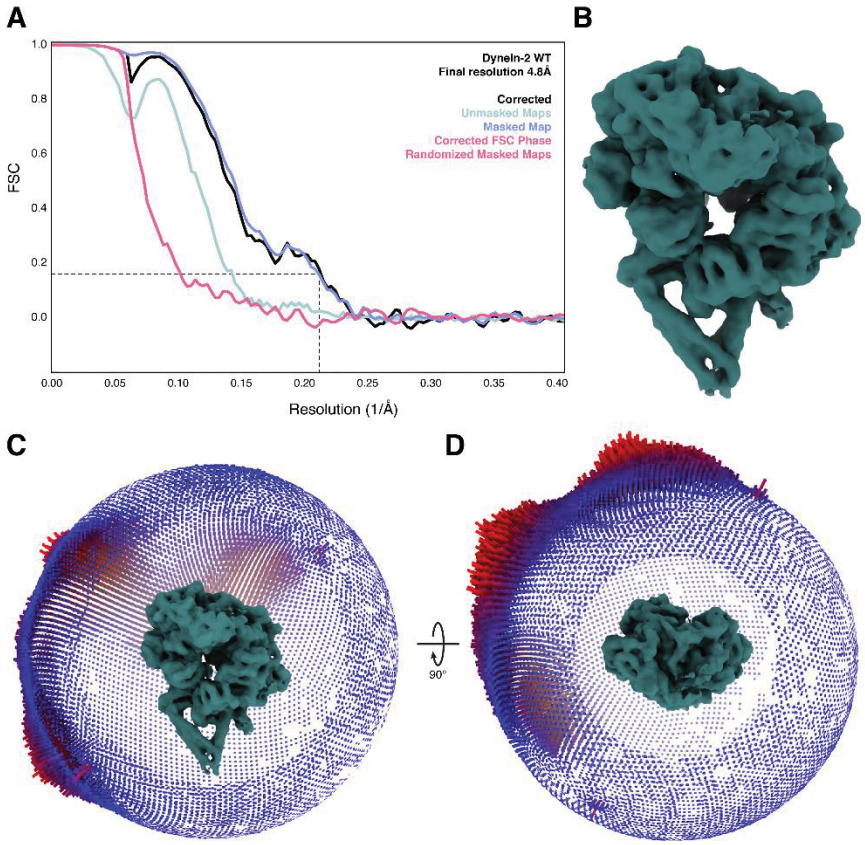

Figure 12. CryoEM reconstruction of the dynein-2 WT. **A** Fourier shell correlation (FSC) for half maps of the dynein-2 WT reconstruction with 0.143 FSC criteria indicated. **B** Density map of the final reconstruction with final resolution of 4.8 Å. Angular distribution of the particle views seen from the motor domain front **C** and the top of the motor domain **D**.

2.4 Dynein-2 ΔAAA2 H2 & PS-I

The protein was prepared with sodium orthovanadate and Mg.ATP to induce ADP.Vi state in the AAA1 domain. Also, in this case the motor domain would be expected to adapt the pre-power stroke conformation. The final reconstruction was done with ~170k particles. There was a significant preferential orientation in the data set. While the final reconstruction was estimated to be around 4.0 Å it was difficult to resolve the main chain (Figure 13 A and B). Nevertheless, I could confidently dock in all the domains in the AAA+ ring. I had attempted grid optimization to overcome the preferential orientation issue by testing gold grids and the addition of detergent, but

none of these measures improved the angular distribution of the projections (Figure 13 C and D).

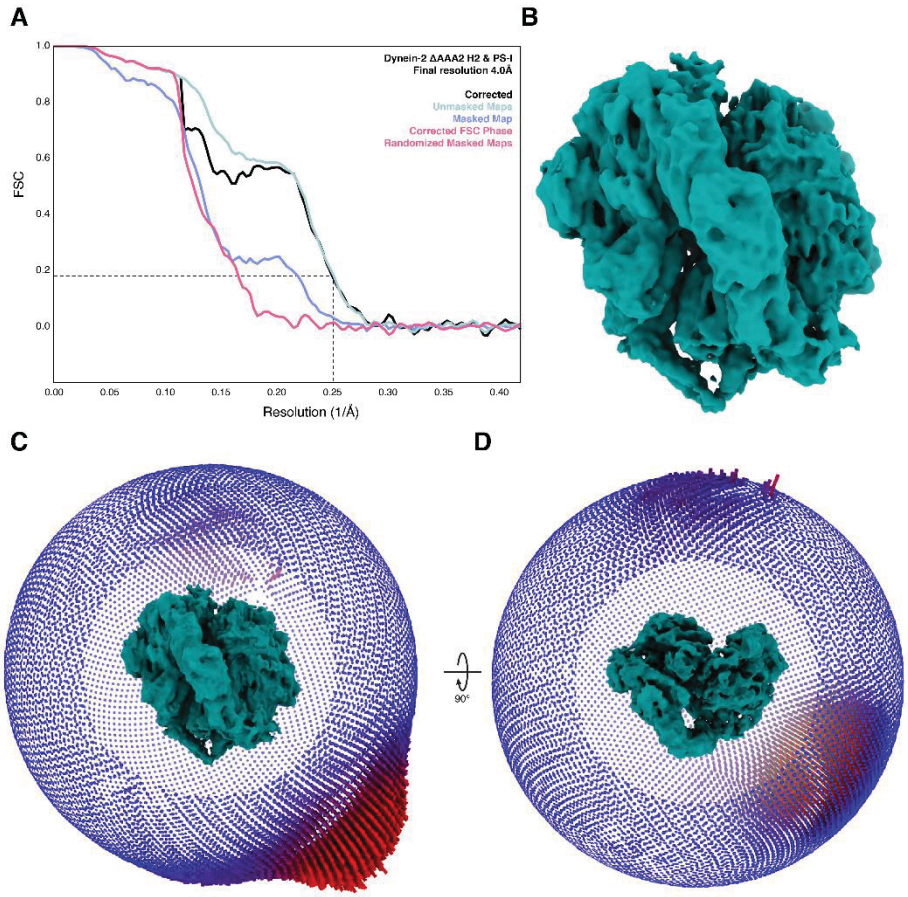

Figure 13. CryoEM reconstruction of the dynein-2 ΔAAA2 H2 & PS-I. **A** Fourier shell correlation (FSC) for half maps of the dynein-2 ΔAAA2 H2 & PS-I reconstruction with 0.143 FSC criteria indicated. **B** Density map of the final reconstruction with final resolution of 4.0 Å. Angular distribution of the particle views seen from the motor domain front **C** and the top of the motor domain **D**.

2.5 Dynein-2 ΔAAA4 PS-I in the ADP.Vi state

The AAA4 PS-I deletion dynein-2 variant was prepared in the presence of ADP.Vi. Dynein-2 in this nucleotide state should mimic the pre-power stroke linker conformation.[8] For the protocol for ADP.Vi nucleotide preparation please refer to the cryoEM sample preparation section in this chapter. The final reconstruction was done with ~140k particles. The final resolution of 3.2Å allowed for a clear assessment of the deletion in the protein structure (Figure 14 A and B), the nucleotide state in the AAA1 domain, and to resolve the side chains. (Figure 14 C and D).

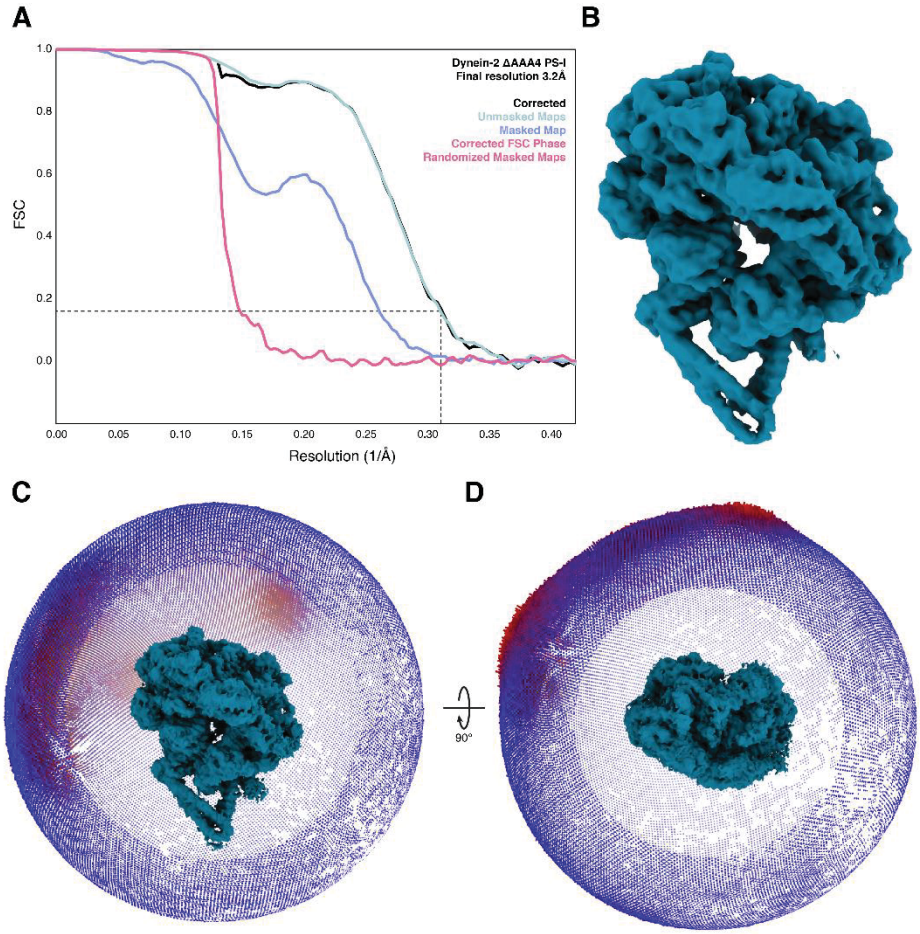

Figure 14. CryoEM reconstruction of the dynein-2 ΔAAA4 PS-I. **A** Fourier shell correlation (FSC) for half maps of the dynein-2 ΔAAA4 PS-I reconstruction with 0.143 FSC criteria indicated. **B** Density map of the final reconstruction with final resolution of 3.2 Å. Angular distribution of the particle views seen from the motor domain front **C** and the top of the motor domain **D**.

2.6 Effect of the AAA2 and AAA4 inserts on dynein-2 linker remodeling

The resolution of the cryoEM maps for dynein-2 WT, AAA2 H2 & PS-I, and AAA4 PS-I deletions allowed for a confident AAA+ domain docking and characterization of the linker conformation.

The dynein motor domain can adapt several geometries depending on the nucleotide state in the AAA1 domain. In the absence of the nucleotide, the APO state, the ring is split into two halves as there are gaps at the interfaces of AAA1 and 2, and AAA5 and 6. In this state the N-terminal linker is docked onto the AAA5 domain.[15] This state is a post-power stroke state and is presented in Figure 15 A. Upon ATP binding the ring enters a closed conformation and there are no gaps at the AAA domain interfaces. This state induces the pre-power stroke conformation which means that

linker bends towards the AAA2/3 interface as shown in Figure 15 B.[14] Upon ATP hydrolysis into ADP and Pi the power stroke takes place, the linker reaches towards the AAA4 domain and the AAA+ ring starts opening up the gaps between AAA1/2 and AAA5/6 again. This is also the post-power stroke conformation (Figure 15 C).[10] The cycle is completed when the linker docks onto the AAA5 domain by opening up the

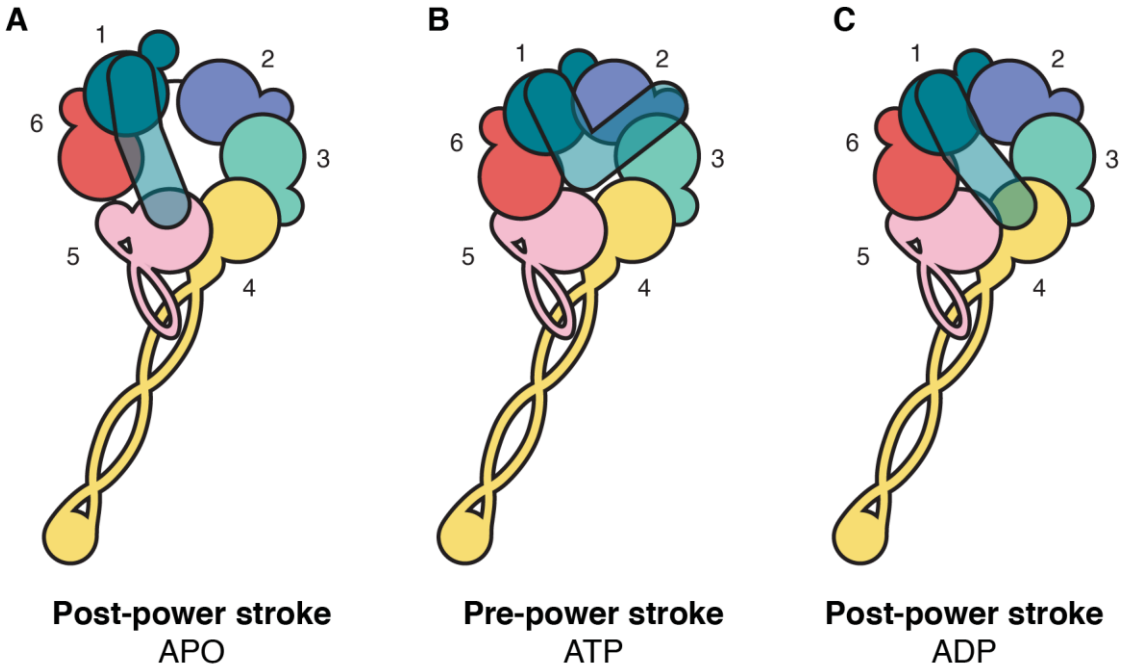

Figure 15. The schematic illustration of different linker and the AAA+ ring geometry. **A** In the APO state the gap between AAA1 and 2, and AAA5 and 6 is open splitting the AAA+ ring into two 'halves'. Without nucleotide the linker is docked onto AAA5. **B** Upon ATP binding AAA+ closes and linker adapts pre-power stroke conformation by reaching the AAA2/3 interface. **C** Upon ATP hydrolysis progression the linker performs the power stroke and lean towards the AAA4 domain. Further docking onto the AAA5 will ejects the ADP from the AAA1 site and prepare the protein for the new power stroke cycle.

AAA1 site even further which 'ejects' the ADP molecule and dynein can undergo a new cycle again.

To maintain a consistent nucleotide state, all samples were prepared with the ATP hydrolysis transition state analogue ADP.Vi, which favours the pre-power stroke conformation of the linker.[8] Moreover this nucleotide state should induce a closed conformation of the AAA+ ring. This significantly helps in the assessment of the nucleotide state based on the ring geometry, and relative population of nucleotide states in the deletion mutants.

In the AAA2 H2 & PS-I deletion mutant both inserts have been replaced with a GG linker. From the cryoEM reconstruction it is clear that the majority of the particles fall into the open AAA+ ring conformation – the APO state. A clear gap between the AAA1/2 domains, and the AAA5/6 domains indicates that no nucleotide is bound to the AAA1 domain (Figure 16 C). This means that ADP.Vi is unable to drive the ring closure as is the case for the WT protein (Figure 16 A). As a consequence the linker is docked onto the AAA5 domain. These structural observations are in line with the reported motility of this deletion, indicating no ATPase activity.[14]

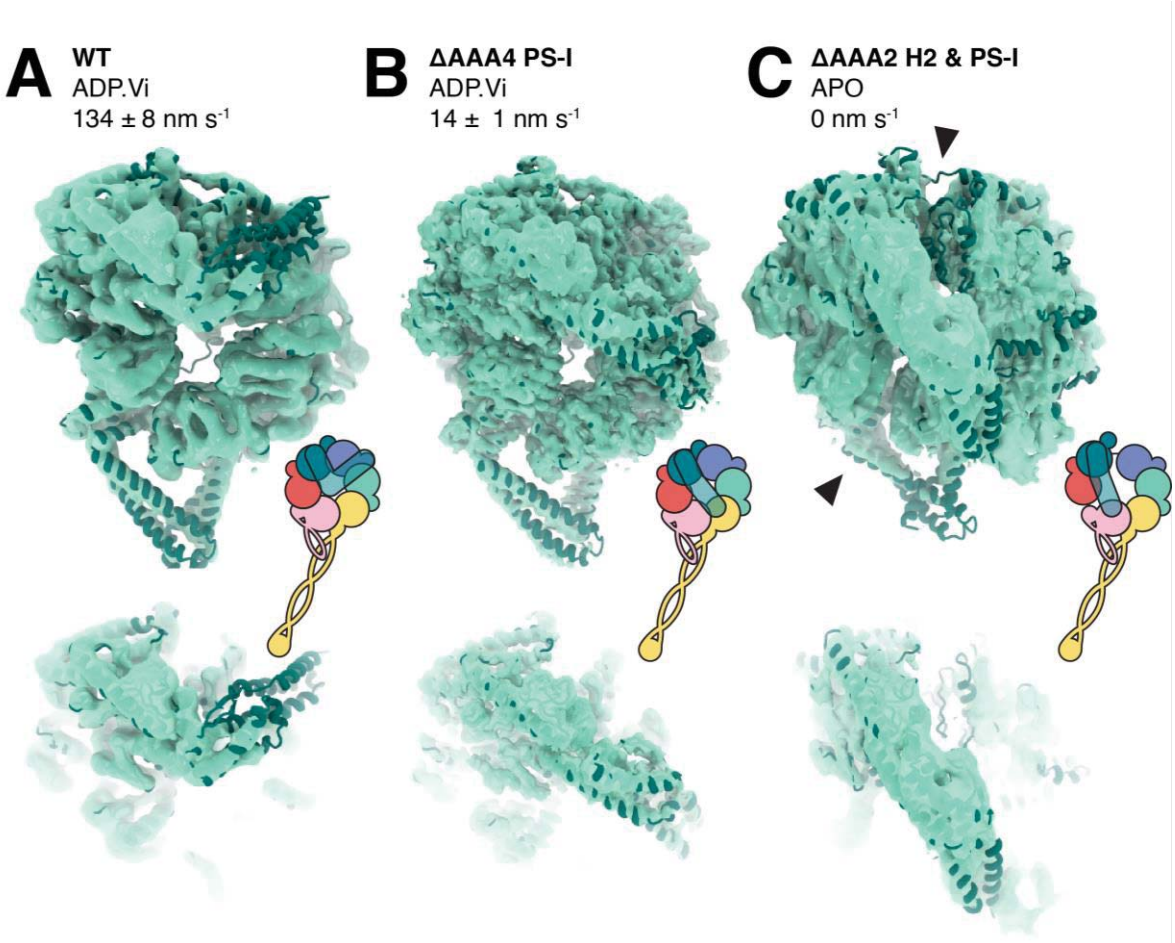

Figure 16. WT, ΔAAA4 PS-I, ΔAAA2 H2 & PS-I reconstructions with indicated nucleotide state in the AAA1 domain and microtubule motility value. Top and bottom panel show the same view of the motor domain and the bottom panel has reduced background to make the linker orientation clearer. **A** WT with the linker docked onto the AAA2/AAA3 domain. **B** ΔAAA4 PS-I variant with the linker docked onto the AAA4. **C** ΔAAA2 H2 & PS-I with linker docked onto the AAA5 domain. Also arrows indicate the gaps created in the APO state. Microtubule motility of each variant taken from Schmidt et al., 2015.

On the other hand PS-I deletion in the AAA4 domain shows a rather closed AAA+ ring conformation (Figure 16 B) and a similar nucleotide state distribution of ADP, ADP.Vi, and APO. This suggests that dynein ATPase activity is not abolished by this deletion, and motility measurements showed only decreased ATPase activity compared to the WT.[14] The nucleotide state of this deletion could also be confidently

assessed from the cryoEM maps as the ADP and ADP.Vi state maps reached sub 3.5 Å resolution. Strikingly, even in the closed ring conformations the linker docks onto the AAA4 domain. This is an unexpected observation as in the ADP.Vi state the linker is expected to be in the pre-power stroke conformation – bent and docked onto the AAA2/3 interface.

2.7 Discussion

Dynein developed the ability to convert chemical energy into mechanical work to drive movement along microtubules. This energy conversion is directly linked to a large conformational change in the dynein motor domain – the linker remodeling.

It is not precisely known how ATP hydrolysis at AAA1 and the subsequent opening and closing of the AAA+ ring trigger linker remodeling. The AAA4 PS-I α-helical insert and the two AAA2 β-hairpin inserts (AAA2 H2 & PS-I) have already been shown to affect the linker conformation based on low resolution negative stain electron microscopy. Moreover the effect of these structural features have been shown to dramatically affect dynein's motility in microtubule gliding assays.[14] In this work I wanted to investigate what the exact role of the AAA2 and AAA4 inserts were during linker remodeling.

I successfully produced four dynein-2 constructs in insect cells: dynein-2 WT, ΔAAA2 H2 & PS-I, ΔAAA2 H2, and ΔAAA4 PS-I. All of them expressed very well yielding sufficient amounts for cryoEM analysis. Normally a litre of Sf9 culture gave around 0.5-1.0 mg of pure protein. Even though all the samples behaved similarly during purification the ΔAAA2 H2 particles displayed a strong preferential orientation on the cryoEM grid compared to WT, ΔAAA2 H2 & PS-I, and ΔAAA4 PS-I. In order to overcome the preferred orientation problem, I screened several types of grids and additives, but none of them solved the problem. Also, in every condition and independently of concentration the protein had a tendency to aggregate on the grid. This might be due to an intrinsic property of this deletion that cause some misfolding or change in surface character of the AAA4 domain, and consequently, aggregation on the grid. Another strategy that I used to try to overcome the preferred orientation problem was to combine several datasets to potentially enrich the rare particle orientations needed for a convincing reconstruction. Even though I was able to

increase the number of particles from ~180k to ~450k, there were no additional views in the 2D classification, and as a consequence, I was not able to obtain a 3D reconstruction for the dynein-2 ΔAAA2 H2 deletion mutant.

The resolution of the AAA2 H2 & PS-I deletion mutant structure allowed for confident domain assignment in the dynein-2 motor domain. The cryoEM reconstruction resulted in one major population with an open AAA+ ring – the APO state. Consistently with an open ring conformation, the linker is docked onto the AAA5 domain. This indicates that H2 or PS-I are both necessary for the closure of the AAA1 nucleotide binding site. Their location in respect to the AAA1 is shown in Figure 17. This observation is further supported by a reported lack of motility.[14] Based on our unpublished data, ATP hydrolysis in dynein-2 takes place only in the AAA1 domain. This allows me to conclude that this deletion mutant directly affects the AAA1 site in the AAA+ ring.

To narrow down the contribution of the H2 and PS-I inserts separately I attempted to produce the H2 deletion mutant, but as outlined above, the preferential orientation in the cryoEM reconstructions was difficult to overcome. Nevertheless my supervisor performed an ATPase activity assay of that deletion mutant, and strikingly ΔAAA2 H2 had activity close to that of the WT (Figure 17). This suggests that the PS-I insert is required for the AAA+ ring closure and that this insert is somewhat involved in the linker power stroke. A structure of ΔAAA2 H2 would help in understanding whether PS-I involvement in linker dynamics is direct or indirect, but this would require further work to overcome the preferential orientation issue.

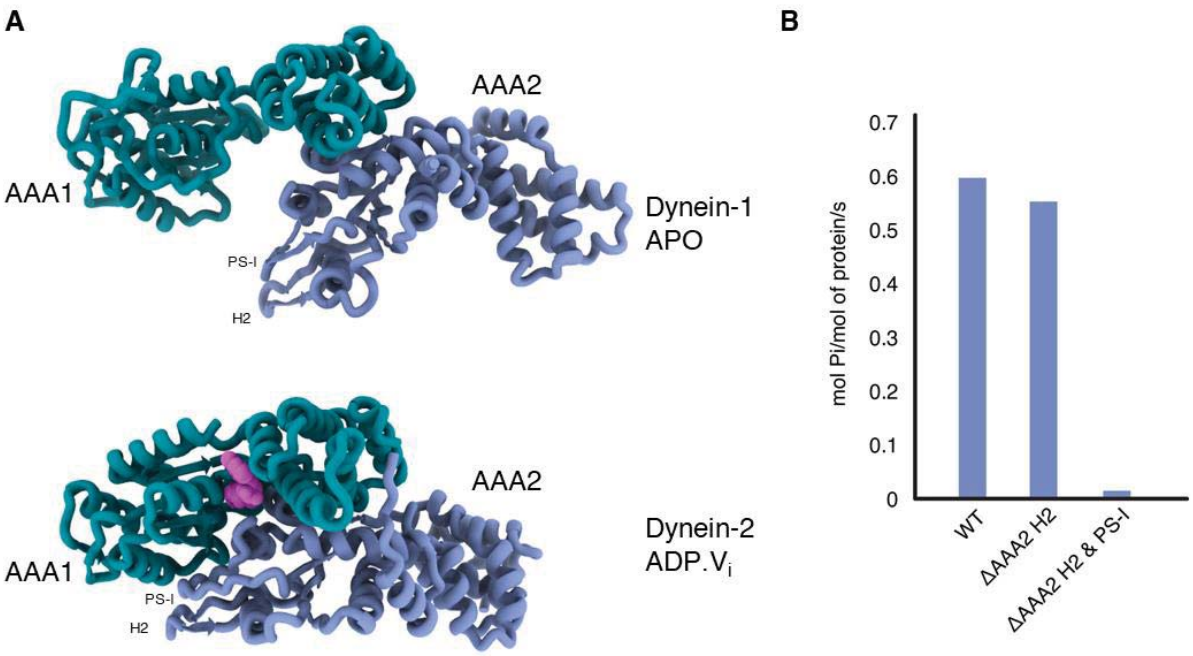

Figure 17. Location of the AAA2 H2 & PS-I inserts in the WT motor domain in APO and ADP.Vi state. **A** Interface between AAA1 and AAA2 in the APO state shows no contacts of the AAA2 PS-I and H2 inserts with AAA1. Upon nucleotide binding the gap between these two domains closes, where AAA2 PS-I insert faces the AAA1 domain. AAA3, 4, 5, and 6 removed for clarity reasons. **B** ATPase activity of the WT, ΔAAA2 H2, and ΔAAA2 H2 & PS-I.

The AAA4 PS-I deletion mutant yielded sub 3.5Å resolution for the ADP and ADP.Vi states. Both nucleotide states are of similar abundance (160k and 140k particles respectively) and both of them appear to be in a closed ring conformation. In both states the linker is docked onto the AAA4 domain. It is expected that in the ADP state we would observe a closed ring conformation, with the linker contacting the AAA4 domain. On the other hand, it was not the expected architecture of the ADP.Vi state, as it should resemble the pre-power stroke linker conformation. This implies that PS-I deletion in the AAA4 domain decouples the linker remodeling from the AAA+ ring closure. The ΔAAA4 PS-I AAA+ ring density is comparable that of the closed ring of the WT protein. This shows that the defective linker dynamics in the ΔAAA4 PS-I is due to deletion of the insert and not due to the altered AAA+ ring geometry. The motility of that deletion mutant is also significantly lower compared to the WT. These observations, taken together, make it difficult to interpret why the AAA4 PS-I insert decouples the linker remodeling from the ring closure and docks it onto the AAA4. The WT maps don't display an obvious structural role of that insert in respect to the linker. It is clear nonetheless that the AAA4 PS-I insert is essential for linker remodeling. One possibility is that the AAA4 PS-I is involved in a transient interaction with the linker that

induces its remodeling and it is a state that is hard to capture with conventional dynein-2 sample preparation methods and applied cryoEM workflows.

2.8 Perspectives

Several obstacles that I faced in this work can be of crucial importance in understanding the dynein linker dynamics. The ΔAAA2 H2 structure would be a great addition to this work and the preferred orientation issue could be addressed by the use of streptavidin affinity grids. This relatively simple approach offers superb particle view distribution where spontaneously biotinylated protein is anchored down to the streptavidin-covered grids. Moreover this approach has proved efficient in cryoEM studies of dynein.[236] Another approach to overcome the preferential orientation problem might be use of the novel blotless grid technologies, such as chameleon® form SPT Labtech which is going to be installed soon at the cryoEM facility at the IGBMC.

There are also some alternative approaches to resolve transient states which potentially limit our interpretation of the ΔAAA4 PS-I deletion mutant. One of them would be use the of the slowly hydrolysable ATP analogue ATPγS. Incubation with that nucleotide could increase the relative abundance of the short-lived states. The incorporation of unnatural amino acids, such as BPA[237] could also be used for a very precise cross-linking approach in order to stabilize selected states.

This work highlights the importance of the AAA+ inserts in the dynein motor domain. The roles of the AAA domain inserts have not yet been structurally characterized, even though their importance has already been reported. Interestingly, they are not part of the catalytic sites involved in binding and nucleotide hydrolysis, but they do affect the dynein conformation by altering the ATP binding properties and the power stroke performance. Deletion of the AAA2 and AAA4 inserts has been shown to have a dramatic effect on AAA+ properties in dynein. This raises several other aspects worth considering to understand dynein's mechanochemical cycle. Analysis of the AAA1, AAA3, and AAA5 inserts in the dynein motor domain would be useful to complete this work and to give a global image on the roles of these motifs, as it is already clear that the AAA2 and AAA4 inserts have distinct effects on the motor domain by altering the linker docking sites as well as the ATPase activity.

RESULTS

Structural Studies of the Dynein Complex Involved in the Neocortex Development

3. Results: Structural Studies of the Dynein Complex Involved in the Neocortex Development

3.1 In vitro characterization of the full-length human dynein-1 cargo adaptor BicD2

This chapter includes a manuscript submitted to the bioRxiv server and to the journal Structure (Cell Press). The manuscript is followed by supplementary materials which are not going to be included in this publication but that were essential parts of this project.

In vitro characterization of the full-length human dynein-1 cargo adaptor BicD2

Robert Fagiewicz[1,2,3,4], Corinne Crucifix[1,2,3,4], Célia Deville[1,2,3,4], Bruno Kieffer[1,2,3,4], Yves Nominé[1,2,3,4], Johan Busselez[1,2,3,4], Paola Rossolilo[1,2,3,4], Helgo Schmidt[1,2,3,4]

1. Institut de Génétique et de Biologie Moléculaire et Cellulaire, Integrated Structural Biology Department, Illkirch, France
2. Centre National de la Recherche Scientifique, UMR7104, Illkirch, France
3. Institut National de la Santé et de la Recherche Médicale, U1258, Illkirch, France
4. Université de Strasbourg, Illkirch, France

ABSTRACT

The cargo adaptors are crucial in coupling motor proteins with their respective cargos and regulatory proteins. BicD2 is one of the most prominent examples within the cargo adaptor family. BicD2 is able to recruit the microtubule motor dynein to RNA, viral particles and nuclei. The BicD2-mediated interaction between the nucleus and dynein is implicated in mitosis as well as interkinetic nuclear migration (INM) in radial glial progenitor cells, and neuron precursor migration during embryonic neocortex development. In vitro studies involving full-length cargo adaptors are difficult to perform due to the hydrophobic character, low-expression levels, and intrinsic flexibility of cargo adaptors. Here we report the recombinant production of full-length human BicD2 and confirm its biochemical activity by interaction studies with RanBP2 and cytoplasmic dynein-1. We also describe pH-dependent conformational changes of BicD2 using cryoEM, template-free structure predictions, and biophysical tools. Our results will help define the biochemical parameters for the in vitro reconstitution of higher order BicD2 protein complexes.

INTRODUCTION

Cytoplasmic dynein drives the majority of retrograde microtubule transport events in eukaryotic cells. The main isoform – cytoplasmic dynein-1 (hereafter dynein-1) is involved in cell division, the transport of organelles and vesicles, brain and muscle development, and can also be hijacked by pathogenic viruses to reach cellular locations[1,2,3,4,5]. It is a particularly interesting motor in neurons, as it carries essential signals and organelles from distal axon sites to the cell body[6].

Dynein-1 motility and cargo specificity depends on cargo adaptor proteins. Currently there are eleven dynein-1 cargo adaptors known and this number is continuously growing[7]. Cargo adaptors are characterized by α-helices forming extended coiled-coil domains and they have the ability to interact with multiple proteins. Generally, the N-terminal region of

the cargo adaptor associates with the dynein motor while the C-terminal domain recruits cargos. Selectivity towards their cargos is achieved by adaptor-specific cargo binding mechanisms[8,9,10].

The best studied family of cargo adaptors are the BicD proteins. Mammals have two BicD orthologues, BicD1 and BicD2. BicD's form a homodimer and based on secondary structure predictions, they fold into three coiled-coil domains (CC1, CC2, and CC3). The N-terminal coiled-coil domain (CC1), was shown to bind dynactin and dynein via the ARP1 subunit of dynactin and the N-terminus of the dynein heavy chain[11,12] as well as LIC1.[8,13] These multiple interactions increase the affinity of the dynein for dynactin and are required for stable dynein/dynactin/BicD2 complex (DDB) formation.[14,15,16] It was also shown that the N-terminal region of BicD2 alone is able to induce DDB complex formation with higher efficiency than the full-length protein[17]. CC1 domain contains the dynein and dynactin interacting motifs – the CC1 box[10,13,18] and the spindly motif[10,19,20]. The C-terminal domains of BicD's (CC2 and CC3), are usually implicated in cargo recruitment. The BicD1 C-terminal CC3 domain can interact with GTP-bound RAB6B[21,22,23,24,25] and cytomegalovirus/HHV-5 protein UL32[26]. BicD2 is able to recruit RAB6A[27], NEK9[28], DNAI1[29,30], RANBP2[31], and kinesin KIF5A[31]. Cargo adaptors of the BicD family also interact with themselves. It has been observed by several groups that the C-terminal part is able to make contact with the N-terminal part leading to an autoinhibited state in BicD1[32] and BicD[33,34]. There is little known about human BicD2 autoinhibition and many features are assumed to be common with better-studied Drosophila BicD ortholog[35,36]. It has also been suggested that the autoinhibited state can be relieved by cargo binding[33,37,38,35]. There is evidence of cargo-induced autoinhibition release in Drosophila BicD with Egl and mRNA as a cargo.[35] So far no such studies have been done for either BicD1 or BicD2.

Understanding the structure, dynamics and reactivity of cargo adaptor proteins is required to advance our understanding of cargo selection, recruitment, and release. Most of the in vitro reconstitution experiments of the human BicD2 with cargo and/or dynein-dynactin were performed on a truncated protein or the Drosophila ortholog. As it is an extensively studied dynein adaptor, there is a need for a protocol for robust production of the full-length human BicD2. The long-standing challenges in characterising cargo adaptors like BicD2 are limited expression levels and solubility which makes them poor targets for structural and functional analyses. Here we describe the recombinant production of the human full-length BicD2 and provide novel insights to its in vitro behaviour. We validated the dimeric nature of recombinant BicD2 and its correct folding. Our findings reveal unexpected pH-dependent conformations of BicD2 in in vitro conditions. It affects BicD2 folding and conformation in a pH range from 6 to 8, which we confirmed with several biophysical techniques and cryoEM. We also address the biochemical activity of BicD2 by interaction studies with RanBP2 and dynein-1/dynactin. Our findings lay the ground for further studies on BicD2 reactivity, regulation, and role in motor protein complexes formation.

RESULTS

Biochemical characterization of full length BicD2

We succeeded in producing full-length human BicD2 isoform 2 under mild solubilizing conditions (see methods) and subsequently characterized its biochemical and functional properties. The addition of mild zwitterionic surfactants like CHAPS to the lysis buffer was crucial for obtaining sufficient protein amounts for large scale purifications. Our size-exclusion multi-angle light scattering (SEC-MALS) analysis indicates a molecular weight of 192 (±0.7%) kDa (Supplementary figure 1A). The slightly higher molecular weight is likely caused by the presence of the detergent in solution hence it is in agreement with the expected value of 186 kDa for a full-length BicD2 dimer. BicD2 also elutes at a volume of 1.35 mL on a Superose® 6 Increase 3.2/300 size exclusion column, which is earlier than expected and most likely caused by the increased hydrodynamic radius due to the extended coiled-coil fold of BicD2.

We evaluated the effect of buffers on the stability of BicD2 by differential scanning fluorimetry (nanoDSF) to establish an optimal buffer composition. The pH screen revealed that the BicD2 stability varies considerably in the range from pH 6.0 to pH 8.0 (Figure 2A). The melting curves at pH 7.0 and pH 8.0 show clear but distinct inflection points, while the curve at pH 6 indicates partly unfolded protein. The full-length BicD2 carries a net negative charge at all of these pH values (Supplementary figure 1B). We also performed three SEC runs on full-length BicD2 at pH 6.0, 7.0, and 8.0. The first run after affinity purification at pH 7.0 and pH 8.0 was characterized by an elution peak for dimeric BicD2 between 1.3 – 1.4 mL and a broad peak of degraded BicD2 around 1.8 mL (Supplementary figure 1C). The second SEC run yielded clean BicD2 fractions (Figure 2B). The slightly different SEC elution volumes and the distinct inflection points in the DSC melting curves suggest the possibility of different BicD2 conformations at pH 7.0 and pH 8.0. Moreover, the protein ran at pH 7.0 had significantly higher ratio of BicD2 to degrading protein compared to pH 8.0 where degradation proceeds more rapidly (Supplementary figure 1B). At pH 6.0 BicD2 eluted almost at the end of the column suggesting partial denaturation (Figure 2B). Re-running the BicD2 peak fractions revealed elution peaks at the expected volumes without additional degradation peaks. These results were further confirmed by circular dichroism (CD) experiments (Supplementary figure 2). The spectra for pH 7.0 and pH 8.0 suggest almost pure α-helical content, consistent with the predicted BicD2 fold. The CD spectrum for pH 6.0 does not resemble the α-helical model, but also does not fit into random-coil models. Heating the protein up to 60 °C did not reveal the random coil characteristic peaks (Supplementary figure 2B). This suggests that the protein at pH 6.0 adopts partially unfolded structure.

Influence of pH value on BicD2's conformation and stability

In order to obtain insights into the conformation of BicD2 at pH 7.0 and pH 8.0, we directly visualized BicD2 at these pH values using a cryo-electron microscope. We collected two datasets and applied identical data processing workflows to avoid bias in the

interpretation. The representative 2D classes showed that most molecules at pH 8.0 fall into an extended conformation (Figure 2C), whereas the vast majority of BicD2 particles adopt more compact conformations (Figure 2D) at pH 7.0. These results are consistent with the results from the SEC runs where BicD2 elutes at 1.4 mL at pH 7.0 but 1.35 mL at pH 8.0 suggesting a shorter hydrodynamic radius at pH 7.0.

Next we wanted to identify amino-acid residues that potentially could be responsible for the pH dependent conformational changes of BicD2. We analysed multiple sequence alignments and focused on conserved histidines as they often have crucial functions in pH-sensitive proteins. The alignment of eukaryotic BicD, BicD1's, and BicD2's shows only a poor sequence identity of less than 10%. However, in the C-terminal part of the CC2 domain there is a short 'YH' sequence motif that is present in all BicD isoforms (Figure 3A). We generated a structure prediction with AlphaFold2[39] for the CC2 and CC3 domain of the human BicD2 (Figure 3B) to evaluate where these residues are potentially located within the predicted structure. Our analysis suggests that they are not involved in dimer interactions, but that they are located within the tri-helical interface of H3, H4, and H5. We compared the YH-containing motif of hsBicD2 (Y538-H539) with its two distant isoforms – D. melanogaster BicD and C. elegans BicD1. The architecture is very similar for all isoforms. Importantly, in all cases there is another conserved basic residue (H640) on the H5 helix that could interact with residue Y538 on the H3 helix (Figure 3C). In order to validate the structure predicted by AF2, we have also compared it to the negative stain class averages reported for BicD[35] (Supplementary figure 3).

To test if the YH motif and the interhelical tyrosine-histidine pair (Y538-H640) interfere with BicD2's pH dependent behaviour in-vitro, we generated the H539A/Y538A and H539A/Y538A/H640A mutants and characterized them by SEC at pH 7.0 and pH 8.0. The fact that the differences in the BicD2 elution peaks do still exist suggests that also the underlying conformational differences are still present. Furthermore, the mutant BicD2 proteins are more prone to degradation, because the equilibrium between the peaks for full-length BicD2 and its degradation products has shifted towards the degradation products. This effect is more pronounced for the H539A/Y538A/H640A triple mutant (Figure 3D). At pH 7.0 the BicD2 fraction is the most abundant, while at pH8.0 the BicD2 fraction significantly decreases and the protein is prone to degradation. Even though H539/Y538/H640 does not seem to be involved in the pH-induced conformational changes of full-length BicD2, these residues nevertheless are clearly important for the stability of the protein.

BicD2's interaction with RanBP2 and dynein/dynactin

RanBP2 (or Nup358) is known to recruit BicD2 through a small disordered region between two Ran binding domains (2003-2444) as demonstrated in yeast two-hybrid assays.[40] The BicD2 binding domain of RanBP2 (hereafter $RanBP2_{BBD}$) interacts with the C-terminus of BicD2 (715-804)[41] and contains several consensus CDK1 phosphorylation sites, which have been shown to be important for BicD2 binding.[42] However, a recent in-vitro experiment demonstrated that the $RanBP2_{BBD}$ -BicD2 complex can also be formed in the absence of phosphorylation.[41] Since all these experiments used the truncated BicD2 C-terminus, the binding of the full-length BicD2 to $RanBP2_{BBD}$ remains to be characterized. In order to clarify the role of phosphorylation in BicD2- $RanBP2_{BBD}$ complex formation, and to confirm the biochemical activity of our recombinant full-length BicD2, we evaluated the interaction with its binding partner RanBP2.

We performed double pull-down assays with full length BicD2 and $RanBP2_{BBD}$ as well as with a phosphomimetic variant of $RanBP2_{BBD}$ where the known CDK1 phosphorylation sites had been mutated to aspartates (T2153D, S2246D, S2251D, S2276D, and S2280D). We were able to obtain a BicD2-$RanBP2_{BBD}$ complex in both cases (Supplementary figure 3A). However, subsequent SEC runs of the purified complexes indicated that they are not stable and that they dissociate. In order to investigate if $RanBP2_{BBD}$ phosphorylation leads to more stable complex formation, we produced recombinant CDK1[43] and performed an in vitro kinase assay on $RanBP2_{BBD}$. The mass spectrometry analysis revealed eight S/T consensus sites in the BicD2 binding region of RanBP2 of which five overlapped with earlier findings[42] (Supplementary figure 4). We mixed in vitro phosphorylated or non-phosphorylated $RanBP2_{BBD}$ with full length BicD2 and analysed the samples by SEC. Successful complex formation was only observed for the in vitro phosphorylated RanBP2 (Figure 4A). Next, we investigated if BicD2 can be phosphorylated by CDK1 and if such a modification could potentially strengthen complex formation with $RanBP2_{BBD}$. The mass spectrometry analysis after BicD2 in vitro phosphorylation indicated five phosphorylation sites in regions predicted to be structurally disordered demonstrating that BicD2 can be phosphorylated by CDK1 (Supplementary figure 4). We mixed the in vitro phosphorylated BicD2 with non-modified $RanBP2_{BBD}$ and subsequently analysed the sample by SEC. There was no indication of complex formation (Figure 4A). The equivalent experiment with in vitro phosphorylated $RanBP2_{BBD}$ did not show any evidence of increased BicD2-$RanBP2_{BBD}$ complex formation compared to non-modified BicD2 – in vitro phosphorylated RanBP2 SEC run (Figure 4A). These results suggest that BicD2 phosphorylation does not contribute to the BicD2-$RanBP2_{BBD}$ complex formation.

We also analysed the influence of pH on BicD2-$RanBP2_{BBD}$ complex formation. To this end, we mixed full-length BicD2, $RanBP2_{BBD}$ and CDK1 at pH 7.0 and pH 8.0 to induce complex formation and analysed the samples by SEC. We also carried out the corresponding control experiments in the absence of CDK1 (Figure 4B). From the fractions analysed by SDS-PAGE, it is evident that complex formation is enhanced with

CDK1-treated samples. Interestingly, the two runs at pH 7.0 (with and without CDK1) showed a broad distribution of RanBP2$_{BBD}$ throughout the elution and only minor increase in the RanBP2 intensity at BicD2 peak fractions in the presence of CDK1. Taken together, these observations suggest that the BicD2-RanBP2$_{BBD}$ complex forms best under slightly alkaline pH which narrows the pool of RanBP2$_{BBD}$ species.

Next, we analysed if the complex between full-length BicD2 and RanBP2$_{BBD}$ is able to interact with dynein/dynactin. We pre-incubated CDK1 phosphorylated RanBP2$_{BBD}$ with BicD2 and mixed the complex with freshly prepared rat brain lysate. We pulled on BicD2 and characterized the sample by mass spectrometry. We could identify several dynein and dynactin components, such as dynein-1 heavy chain and p150, which indicated the presence of a dynein/dynactin-BicD2-RanBP2 complex (Supplementary figure 3B).

DISCUSSION

The ability of Dynein-1 to bind a wide range of cargoes is mediated by its compatibility with many cargo adaptor proteins, such as BicDs, Hooks, NINs, Spindly, TRAKs, RILP or JIP3.[7] Investigating in vitro reconstituted complexes between cargo adaptors and dynein/dynactin has led to valuable insights into dynein motor recruitment and activation.[32,44,45] However most of these studies were done with truncated BicD2 constructs that lack either the dynein- or the cargo- binding domains. Many biophysical and structural studies have been hampered by the lack of sufficient amounts of full-length cargo adaptors. Here we report a robust method for the recombinant production of a full-length BicD2 and demonstrate its correct fold and biochemical activity towards the RanBP2 cargo as well as dynein/dynactin. We believe that our results will facilitate in vitro reconstitution approaches of motor-cargo complexes.

One of the unexpected findings was the strong influence of the pH value on the conformation and stability of full-length BicD2. At pH 6.0, 7.0 and 8.0 BicD2 switches from partially unfolded to compact and to an open conformation. Our cryoEM 2D classification of full-length BicD2 at pH 7.0 indicates that over 50% of the particles fall into compact classes while the majority of particles at pH 8.0 adopt an open conformation. Recent work has provided evidence that the autoinhibited state is characterized by an interaction between the CC2 and CC3 domains.[35] Although we were not able to assign individual coiled-coil domains in our cryoEM 2D class averages due to the intrinsic flexibility of BicD2, there is the possibility that the more compact 2D class averages at pH 7.0 might represent the autoinhibited state and the extended conformation at pH 8.0 the open, activated state. Similar autoinhibited conformation has also been recently described for cargo adaptor Spindly[46] which suggest that autoinhibition might be a common feature of cargo adaptors.

It is not clear if these pH driven conformational changes are relevant only in vitro or if they also have a physiological relevance. In principle, the cellular pH value could also trigger pH dependent conformational changes of the BicD2 cargo adaptor. At the cytosolic pH

value of ~7.2 most BicD2 molecules would adapt the compact, potentially autoinhibited form and require additional, activating signals to recruit motor proteins and cargo. Conditions that lead to an increase in the intracellular pH, like mitosis and growth factor signalling[47,48,49], could bypass the need for such signals and activate the BicD2 cargo adaptor on a globular level.

In the case of BicD2 one of the activating signals is believed to be the interaction with its cargos like RanBP2[33,35,37,38]. Furthermore, post-translational BicD2 modifications might also influence its reactivity. BicD2 contains several consensus phosphorylation sites[50] and an acetylation site in its N-terminal part[51].

We also have identified three conserved residues, H539/Y538/H640 that contribute to the stability of BicD2. Mutating these amino-acid residues to alanines clearly increased the tendency of BicD2 for self-degradation. Our template-free AlphaFold2 prediction suggest the possibility of Y538/H640 stabilizing the H3-H4-H5 α-helical bundle via intramolecular hydrogen bonds (Supplementary figure 5B and C). Disrupting it could trigger partial unfolding and subsequent protein degradation. A similar architecture (Supplementary figure 5) was also observed in a pH-sensitive endotoxins and mutating the equivalent histidine-tyrosine pair mutation lead to protein destabilization and degradation.[52]

We characterized the BicD2 reactivity with its known cargo protein RanBP2. There are conflicting results in the field with respect to the question whether RanBP2 phosphorylation is a requirement for the interaction with BicD2[42,41]. Our results now reconcile these reports, because they show that BicD2 has the ability to bind both non-phosphorylated as well as phosphorylated $RanBP2_{DDB}$. In double pull-downs we observed that BicD2 readily interacts with RanBP2 without any protein modification at pH 7.0 and 8.0. These complexes are nevertheless unstable over SEC. This suggests that there is a weak association of these proteins in vitro in a wide range of conditions. The CDK1 phosphorylation of $RanBP2_{BBD}$ (but not BicD2) significantly increased the stability of the complex and increase in the pH value improved the complex homogeneity.

ACKNOWLEDGEMENT

This research was supported by a LabEx start up grant (ANR-10-LABEX-30-HS) to HS and Boehringer Ingelheim Fonds as well as FRM PhD fellowships to RF. This study was further supported by the grant ANR-10-LABX-0030-INRT, a French State fund managed by the Agence Nationale de la Recherche under the frame program Investissements d'Avenir ANR-10-IDEX-0002–02. The authors acknowledge the support and the use of resources of the French Infrastructure for Integrated Structural Biology (FRISBI) ANR-10-INBS-05 and of Instruct-ERIC. We also thank the IGBMC molecular biology and virus service (Nicole Jung and Thierry Lerouge) as well as IGBMC proteomics platform (Frank Ruffenach, Luc Negroni, and Bastien Morlet).

AUTHOR CONTRIBUTIONS

RF: conceptualization, data curation and analysis, validation, investigation, methodology, funding acquisition and manuscript writing. CC: methodology, investigation and data analysis. CD & BF: data analysis and discussion. YN, JB and PR: investigation and data analysis. HS: conceptualization, data analysis, supervision, funding acquisition, methodology, manuscript writing and project administration.

DECLARATION OF INTEREST

The authors declare no competing interests.

MATERIALS AND METHODS

Cloning and mutagenesis

Human BicD2 isoform 2 and $RanBP_{BBD}$ genes were ordered from Epoch LifeScience and codon-optimized for Escherichia coli expression. The genes were subsequently cloned into the pNHD expression vector (a vector used for site-specific pSer incorporation[53], but both proteins express equally well in a commercial pMMS vector). The BicD2 plasmid was modified to introduce an N-terminal STREP-tag followed by a short 'GSGSG' linker. The $RanBP_{BBD}$ plasmid was fused with a C-terminal double TEV cleavage site, a GSGSG linker, and a 6xHis tag. The H539A/Y538A and H539A/Y538A/H640A mutants were generated by rolling circle PCR. The co-expression plasmid encoding CDK1-cyclinB for insect cell expression was a kind gift from the Andrea Musacchio lab.

Protein expression and purification

Plasmids for bacterial expression were transformed into E. coli BL21(DE3) chemically competent cells and grown overnight on tetracycline plates. The plate was used for inoculation of the 50 mL LB medium pre-culture which was grown overnight at 37°C for further scale-up. Protein expression was induced at 25°C with 1mM isopropyl-1-thio-β-D-galactopyranoside (IPTG) and expressed for 3h at 37°C. Cells were harvested, washed with 1xPBS, and frozen. BicD2 WT and mutants were re-suspended in the lysis buffer containing 1xPBS pH8.0, 10% glycerol, 7 mM CHAPS, 2 mM DTT, 2mM PMSF, protease inhibitors, and incubated on a roller for 1-2h at 4°C. Cells were lysed by sonication (5x30s with 30s breaks on ice) and centrifuged at 30000 rpm at 4°C for 1 hour. The supernatant was mixed with pre-equilibrated STREP-tactin 4XL beads and incubated on a roller for 30 minutes at 4°C before loading on a gravity flow column. The resin was washed with 10 CVs of the lysis buffer, 10 CVs of the wash buffer (1xPBS pH8.0, 10% glycerol, 7 mM CHAPS), and eluted with the elution buffer (1xPBS pH8.0, 10% glycerol, 7 mM CHAPS, 50 mM biotin). Pooled fractions were concentrated to 2 mg/mL and snap-frozen in 100 µL

aliquots for further experiments and gel filtration. RanBP2$_{BBD}$ was purified in the same manner as BicD2 with a difference in the buffer used (20 mM Tris-HCl pH8.0 instead of PBS). Both constructs (WT) yielded around 1 mg of protein per litre of culture (after affinity step).

The CDK1^{CyclinB} plasmid was transformed into E. coli DH10MB-MCherry chemically competent cells with heat shock at 42°C for 30s followed by 6h recovery in LB medium at 37°C with shaking. The cells were then plated on agar plates containing kanamycin (50 µg ml^{-1}), gentamicin (7 µg ml^{-1}), tetracycline (10 µg ml^{-1}), Xgal (600 µg ml^{-1}) and IPTG (40 µg ml^{-1}) and positive clones were identified by a blue/white selection after 24h incubation at 37°C followed by 24h at RT. The positive clones were grown in LB media containing kanamycin (50 µg ml^{-1}), gentamicin (7 µg ml^{-1}), and tetracycline (10 µg ml^{-1}) overnight. Bacmids were purified using the isopropanol precipitation method. 2ml of Sf9 cells at 0.5×10^6 cells per ml were transfected with 2 µg of fresh bacmid DNA and FuGene HD transfection reagent (Promega) at a ratio of 3:1 transfection reagent to DNA. After 72h the 6-well plate was analysed for mCherry fluorescence signal and the positive conditions (V_0) were directly used for further virus amplifications by adding 2mL of V_0 to 50 mL of Sf9 cells at 1x10^6 cells per mL (V_1) and grown for 72h. The V_1 was then used for infecting another 50 mL of Sf9 at 1x10^6 cells/mL (V_2). The V_2 virus was further used to infect 500 mL of the Sf9 culture 1x10^6 cells/mL. After 72h the cells were collected at 1000 rpm for 10 min at 4°C. The pellet was flash-frozen in liquid nitrogen and stored at -80°C until purification. The CDK1^{CyclinB} pellet was re-suspended in the lysis buffer containing 50mM Tris-HCl pH8.0, 10mM $MgCl_2$, 10% glycerol, 0.1% NP40, 0.1 mM EDTA, 2mM DTT, 2 mM PMSF, protease inhibitors, and incubated on a roller for 1h at 4°C. The cells were lysed by sonication (2x30s with 30s breaks on ice) and centrifuged at 40000 rpm at 4°C for 1 hour. The supernatant was mixed with pre-equilibrated GST-sepharose beads for 30 minutes at RT and loaded onto a gravity flow column. The resin was washed with 10 cvs of the lysis buffer, 10 cv' of the wash buffer (Tris-HCl pH8.0, 150mM NaCl, 10% glycerol, 0.1mM EDTA), and eluted with the elution buffer (Tris-HCl pH8.0, 150mM NaCl, 10% glycerol, 0.1mM EDTA, 25mM reduced GST). Pooled fractions were concentrated to 0.5 mg/mL and snap-frozen in 50µL aliquots for further experiments.

SEC-MALS

Prior to SEC-MALS analysis BicD2 dimer was purified on Superose® 6 Increase 3.2/300 column in SEC buffer (50 mM Tris pH 7.5, 150 mM Potassium acetate, 10 mM Magnesium acetate, 7 mM CHAPS). Then 90µL of BicD2 sample (1mg/mL) was injected into FPLC Ettan Micro LC (formerly GE Healthcare, now Cytiva) coupled with MiniDAWN TREOS MALS detector (Wyatt Technology), Optilab T-rEX (Wyatt Technology) RI detector, and Superdex® S200 10/300 GL (formerly GE Healthcare, now Cytiva) column and run at 25°C in SEC buffer (50 mM Tris pH 7.5, 150 mM Potassium acetate, 10 mM Magnesium acetate). The data was processed using the ASTRA software (Wyatt Technology).

Circular dichroism

CD experiments were recorded on a Jasco J-815 spectropolarimeter (Easton, MD) equipped with an automatic 6-position Peltier thermostated cell holder. The instrument was calibrated with 10-camphorsulphonic acid. Samples (65 µL) were prepared in PBS supplemented with CHAPS 7 mM and buffered at various pH (6.0, 7.0 or 8.0). Far-UV CD data were collected in the 182–270 nm range using a 0.1 mm pathlength cell (Quartz-Suprasil, Hellma UK Ltd) at 20.0 °C ± 0.1 °C. Spectra were acquired using a continuous scan rate of 50 nm/min and are presented as an average of 10 successive scans. The response time and the bandwidth were 1.0 s and 1 nm, respectively. The spectra were corrected by subtracting the solvent spectrum obtained under identical conditions.

CryoEM sample preparation

The 100µL sample was thawed on ice and equilibrated with 5xPBS at either pH 8.0 or pH 7.0. The Superose® 6 Increase column was equilibrated for 16h at a specific pH (in PBS buffer only) and the dimer fraction from the SEC taken for grid preparation. Cu/Rh 1.2/1.3 300mesh grids were plasma cleaned for 90s at 30% plasma power (80:20 argon:oxygen). The protein concentration was adjusted to 1µM and applied on the grid and plunge-frozen in a Vitrobot Mark IV robot (FEI), maintained at 100% humidity and 10 °C.

CryoEM data collection and image analysis

Datasets for BicD2 at pH 8.0 and pH 7.0 were collected using a Glacios™ Cryo-TEM operating at 200keV with a K2 Summit direct electron detector (Gatan). Videos were collected in counting mode, with a final calibrated pixel size of 1.078 Å/pixel, 8s exposure, and total dose of ~ 54 $e^-/Å^2$.

SerialEM[54] was used for automated data collection and the videos were processed using Relion3.0.[55] The micrographs were manually filtered giving each dataset ~700 micrographs. Particles were picked using the general model in TOPAZ[56] and 2D classified twice. Each dataset yielded around 150k particles used for 2D classification. All data processing steps were done reference-free.

In vitro kinase assays and phosphorylation mapping

BicD2 or $RanBP2_{BBD}$ were mixed with CDK1 at 1:100 molar ratio with 0.1mM MgATP and incubated for 30min at RT. Each sample had a negative control that did not contain MgATP. Each reaction mixture was loaded on SDS-PAGE and stained with pro-Q diamond stain to check for phosphorylated proteins. Phosphorylatoin sites were analysed with trypsin digest MS using an Orbitrap Elite and Acclaim Pepmap 100 column. The PSM values corresponded to the number of MS2 spectra which made it possible to identify peptides. In BicD2 we covered 75% of the sequence (PSM's: 2087) while for RanBP2 we covered 85% (PSM's: 1195).

AlphFold2 structure prediction

We used the whole CC2 and CC3 domain of a human BicD2 (residues 265-855) to model a homooligomer. We generated 5 models using AlphaFold2[39] advanced notebook from Google Colab. We used MMseqs2[57] (UniRef+Environmental) for MSA generation.

REFERENCES

1. Reck-Peterson, S. L., Redwine, W. B., Vale, R. D. & Carter, A. P. The cytoplasmic dynein transport machinery and its many cargoes. Nat. Rev. Mol. Cell Biol. (2018). doi:10.1038/s41580-018-0004-3
2. Paschal, B. M. & Vallee, R. B. Retrograde transport by the microtubule-associated protein MAP 1C. Nature **330**, 181–183 (1987).
3. Dodding, M. P. & Way, M. Coupling viruses to dynein and kinesin-1. EMBO Journal **30**, 3527–3539 (2011).
4. Wilson, M. H. & Holzbaur, E. L. F. Opposing microtubule motors drive robust nuclear dynamics in developing muscle cells. J. Cell Sci. **125**, 4158–4169 (2012).
5. Fu, M. meng & Holzbaur, E. L. F. Integrated regulation of motor-driven organelle transport by scaffolding proteins. Trends in Cell Biology **24**, 564–574 (2014).
6. Schiavo, G., Greensmith, L., Hafezparast, M. & Fisher, E. M. C. Cytoplasmic dynein heavy chain: The servant of many masters. Trends in Neurosciences **36**, 641–651 (2013).
7. Olenick, M. A. & Holzbaur, E. L. F. Dynein activators and adaptors at a glance. J. Cell Sci. **132**, (2019).
8. CM, S., JM, O., NT, H. & RD, V. A Ras-like domain in the light intermediate chain bridges the dynein motor to a cargo-binding region. Elife **3**, 1–22 (2014).
9. CM, S. & RD, V. Assembly and activation of dynein-dynactin by the cargo adaptor protein Hook3. J. Cell Biol. **214**, 309–318 (2016).
10. JB, G. et al. Molecular mechanism of dynein recruitment to kinetochores by the Rod-Zw10-Zwilch complex and Spindly. J. Cell Biol. **216**, 943–960 (2017).
11. Chowdhury, S., Ketcham, S. A., Schroer, T. A. & Lander, G. C. Structural organization of the dynein-dynactin complex bound to microtubules. doi:10.1038/nsmb.2996
12. L, U. et al. The structure of the dynactin complex and its interaction with dynein. Science **347**, 1441–1446 (2015).
13. IG, L. et al. A conserved interaction of the dynein light intermediate chain with dynein-dynactin effectors necessary for processivity. Nat. Commun. **9**, (2018).
14. MA, S., HT, H., L, U., SL, B. & AP, C. In vitro reconstitution of a highly processive recombinant human dynein complex. EMBO J. **33**, 1855–1868 (2014).
15. Splinter, D. et al. BICD2, dynactin, and LIS1 cooperate in regulating dynein recruitment to cellular structures. https://doi.org/10.1091/mbc.e12-03-0210 **23**, 4226–4241 (2012).

16. McKenney, R. J., Huynh, W., Tanenbaum, M. E., Bhabha, G. & Vale, R. D. Activation of cytoplasmic dynein motility by dynactin-cargo adapter complexes. Science (80-.). **345**, 337–341 (2014).

17. Hoogenraad, C. C. et al. Bicaudal D induces selective dynein-mediated microtubule minus end-directed transport. EMBO J. **22**, 6004–6015 (2003).

18. Celestino, R. et al. A transient helix in the disordered region of dynein light intermediate chain links the motor to structurally diverse adaptors for cargo transport. PLoS Biol. **17**, (2019).

19. Zhang, K. et al. Cryo-EM Reveals How Human Cytoplasmic Dynein Is Auto-inhibited and Activated. Cell **169**, 1303-1314.e18 (2017).

20. Torisawa, T. et al. Autoinhibition and cooperative activation mechanisms of cytoplasmic dynein. Nat. Cell Biol. 2014 1611 **16**, 1118–1124 (2014).

21. Wanschers, B. F. J. et al. A role for the Rab6B Bicaudal–D1 interaction in retrograde transport in neuronal cells. Exp. Cell Res. **313**, 3408–3420 (2007).

22. Hoogenraad, C. C. et al. Mammalian golgi-associated Bicaudal-D2 functions in the dynein-dynactin pathway by interacting with these complexes. EMBO J. **20**, 4041–4054 (2001).

23. Short, B., Preisinger, C., Schaletzky, J., Kopajtich, R. & Barr, F. A. The Rab6 GTPase Regulates Recruitment of the Dynactin Complex to Golgi Membranes. Curr. Biol. **12**, 1792–1795 (2002).

24. Schlager, M. A. et al. Pericentrosomal targeting of Rab6 secretory vesicles by Bicaudal-D-related protein 1 (BICDR-1) regulates neuritogenesis. EMBO J. **29**, 1637–1651 (2010).

25. Matanis, T. et al. Bicaudal-D regulates COPI-independent Golgi-ER transport by recruiting the dynein-dynactin motor complex. Nat. Cell Biol. **4**, 986–992 (2002).

26. SV, I., ME, B. & WJ, B. Bicaudal D1-dependent trafficking of human cytomegalovirus tegument protein pp150 in virus-infected cells. J. Virol. **84**, 3162–3177 (2010).

27. K, P. et al. Molecular defects in the motor adaptor BICD2 cause proximal spinal muscular atrophy with autosomal-dominant inheritance. Am. J. Hum. Genet. **92**, 955–964 (2013).

28. PM, H. et al. Purification, cloning, and characterization of Nek8, a novel NIMA-related kinase, and its candidate substrate Bicd2. J. Biol. Chem. **277**, 16229–16240 (2002).

29. EC, O. et al. Mutations in BICD2 cause dominant congenital spinal muscular atrophy and hereditary spastic paraplegia. Am. J. Hum. Genet. **92**, 965–973 (2013).

30. K, P. et al. Molecular defects in the motor adaptor BICD2 cause proximal spinal muscular atrophy with autosomal-dominant inheritance. Am. J. Hum. Genet. **92**, 955–964 (2013).

31. Splinter, D. et al. Bicaudal D2, dynein, and kinesin-1 associate with nuclear pore complexes and regulate centrosome and nuclear positioning during mitotic entry. PLoS Biol. **8**, (2010).

32. Terawaki, S. I., Yoshikane, A., Higuchi, Y. & Wakamatsu, K. Structural basis for cargo binding and autoinhibition of Bicaudal-D1 by a parallel coiled-coil with homotypic registry. Biochem. Biophys. Res. Commun. **460**, 451–456 (2015).

33. Y, L. et al. Bicaudal-D uses a parallel, homodimeric coiled coil with heterotypic registry to coordinate recruitment of cargos to dynein. Genes Dev. **27**, 1233–1246 (2013).

34. Wharton, R. P. & Struhl, G. Structure of the Drosophila BicaudalD protein and its role in localizing the posterior determinant nanos. Cell **59**, 881–892 (1989).

35. Sladewski, T. E. et al. Recruitment of two dyneins to an mRNA-dependent bicaudal D transport complex. Elife **7**, (2018).

36. Stuurman, N. et al. Interactions between coiled-coil proteins: Drosophila lamin Dm0 binds to the Bicaudal-D protein. Eur. J. Cell Biol. **78**, 278–287 (1999).

37. W, H. & RD, V. Disease-associated mutations in human BICD2 hyperactivate motility of dynein-dynactin. J. Cell Biol. **216**, 3051–3060 (2017).

38. MA, M. et al. RNA-directed activation of cytoplasmic dynein-1 in reconstituted transport RNPs. Elife **7**, (2018).

39. Jumper, J. et al. Highly accurate protein structure prediction with AlphaFold. Nat. 2021 1–7 (2021). doi:10.1038/s41586-021-03819-2

40. D, S. et al. Bicaudal D2, dynein, and kinesin-1 associate with nuclear pore complexes and regulate centrosome and nuclear positioning during mitotic entry. PLoS Biol. **8**, (2010).

41. Gibson 1$, J. M. et al. Coil-to-Helix Transition at the Nup358-BicD2 Interface for Dynein Recruitment and Activation. bioRxiv 2021.05.06.443034 (2021). doi:10.1101/2021.05.06.443034

42. Baffet, A. D., Hu, D. J. & Vallee, R. B. Cdk1 Activates Pre-mitotic Nuclear Envelope Dynein Recruitment and Apical Nuclear Migration in Neural Stem Cells. Dev. Cell **33**, 703–716 (2015).

43. Veld, P. J. H. in 't et al. Reconstitution and use of highly active human CDK1:Cyclin-B:CKS1 complexes. bioRxiv 2021.09.24.461690 (2021). doi:10.1101/2021.09.24.461690

44. Liu, Y. et al. Bicaudal-D uses a parallel, homodimericcoiled coil with heterotypic registry tocoordinate recruitment of cargos to dynein. Genes Dev. **27**, 1233–1246 (2013).

45. Noell, C. R. et al. Role of Coiled-Coil Registry Shifts in the Activation of Human Bicaudal D2 for Dynein Recruitment upon Cargo Binding. J. Phys. Chem. Lett. **10**, 4362–4367 (2019).

46. d'Amico, E. et al. Conformational transitions of the mitotic adaptor Spindly underlie its interaction with Dynein and Dynactin. bioRxiv 2022.02.02.478874 (2022). doi:10.1101/2022.02.02.478874

47. Gagliardi, L. J. & Shain, D. H. Is intracellular pH a clock for mitosis? Theor. Biol. Med. Model. **10**, 8 (2013).

48. Pouysségur, J., Franchi, A., L'Allemain, G. & Paris, S. Cytoplasmic pH, a key determinant of growth factor-induced DNA synthesis in quiescent fibroblasts. FEBS Lett. **190**, 115–119 (1985).

49. Chambard, J. C. & Pouyssegur, J. Intracellular pH controls growth factor-induced ribosomal protein S6 phosphorylation and protein synthesis in the G0→G1 transition of fibroblasts. Exp. Cell Res. **164**, 282–294 (1986).

50. PM, H. et al. Purification, cloning, and characterization of Nek8, a novel NIMA-related kinase, and its candidate substrate Bicd2. J. Biol. Chem. **277**, 16229–16240 (2002).

51. Van Damme, P. et al. N-terminal acetylome analyses and functional insights of the N-terminal acetyltransferase NatB. Proc. Natl. Acad. Sci. U. S. A. **109**, 12449–12454 (2012).

52. Seale, J. W. The role of a conserved histidine–tyrosine interhelical interaction in the ion channel domain of δ-endotoxins from Bacillus thuringiensis. Proteins Struct. Funct. Bioinforma. **63**, 385–390 (2006).

53. Rogerson, D. T. et al. Efficient genetic encoding of phosphoserine and its nonhydrolyzable analog. Nat. Chem. Biol. 2015 117 **11**, 496–503 (2015).

54. Mastronarde, D. N. Automated electron microscope tomography using robust prediction of specimen movements. J. Struct. Biol. **152**, 36–51 (2005).

55. Zivanov, J. et al. New tools for automated high-resolution cryo-EM structure determination in RELION-3. Elife **7**, (2018).

56. Bepler, T. et al. Positive-unlabeled convolutional neural networks for particle picking in cryo-electron micrographs. Nat. Methods 2019 1611 **16**, 1153–1160 (2019).

57. Steinegger, M. & Söding, J. MMseqs2 enables sensitive protein sequence searching for the analysis of massive data sets. Nat. Biotechnol. 2017 3511 **35**, 1026–1028 (2017).

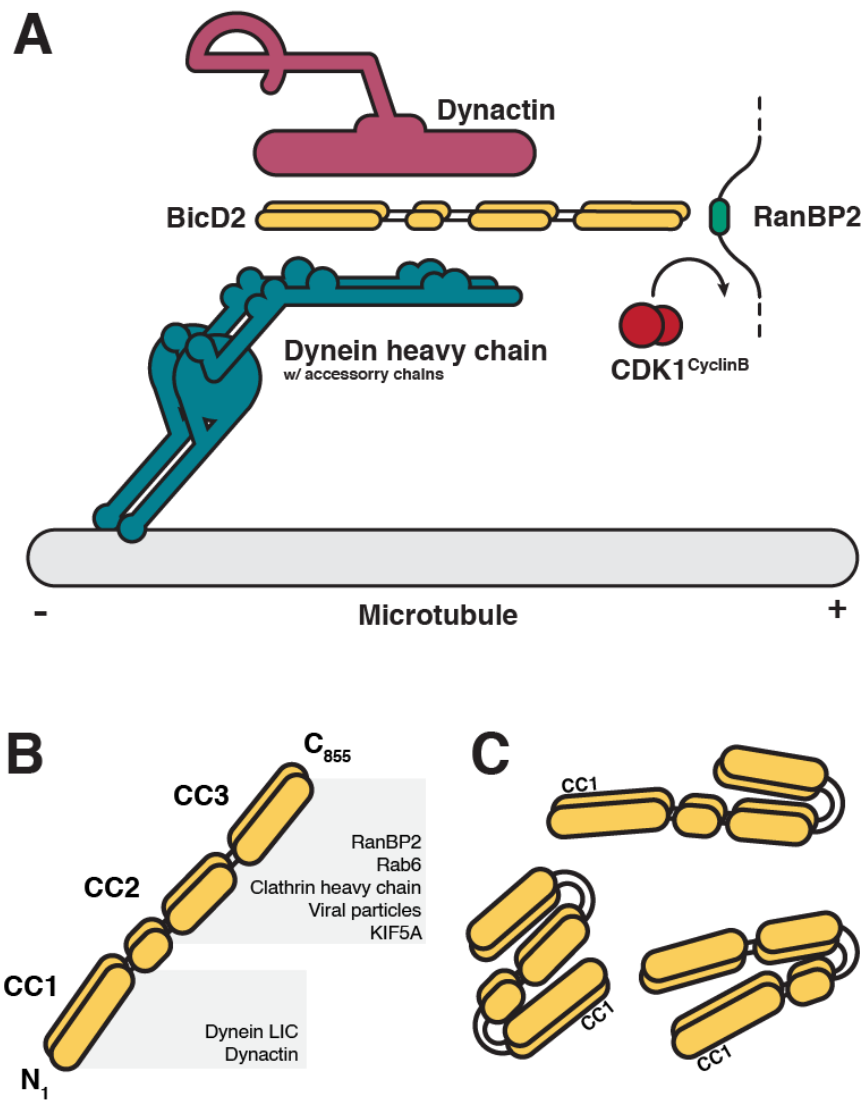

Figure 1. A Schematic representation of the dynein-dynactin-BicD2 complex associated with the cargo protein – RanBP2. $CDK1^{CyclinB}$ activity has been known to activate this complex to progressively move the nucleus in radial glial progenitor cells towards the base of the neocortex in the developing human brain. **B** Domain organization of the BicD2 cargo adaptor dimer. The N-terminal part is responsible for binding dynein and dynactin while the C-terminal part binds plus-end directed motor kinesin-1 and cargos. **C** Hypothetical BicD2 autoinhibited conformations from the previously reported data.

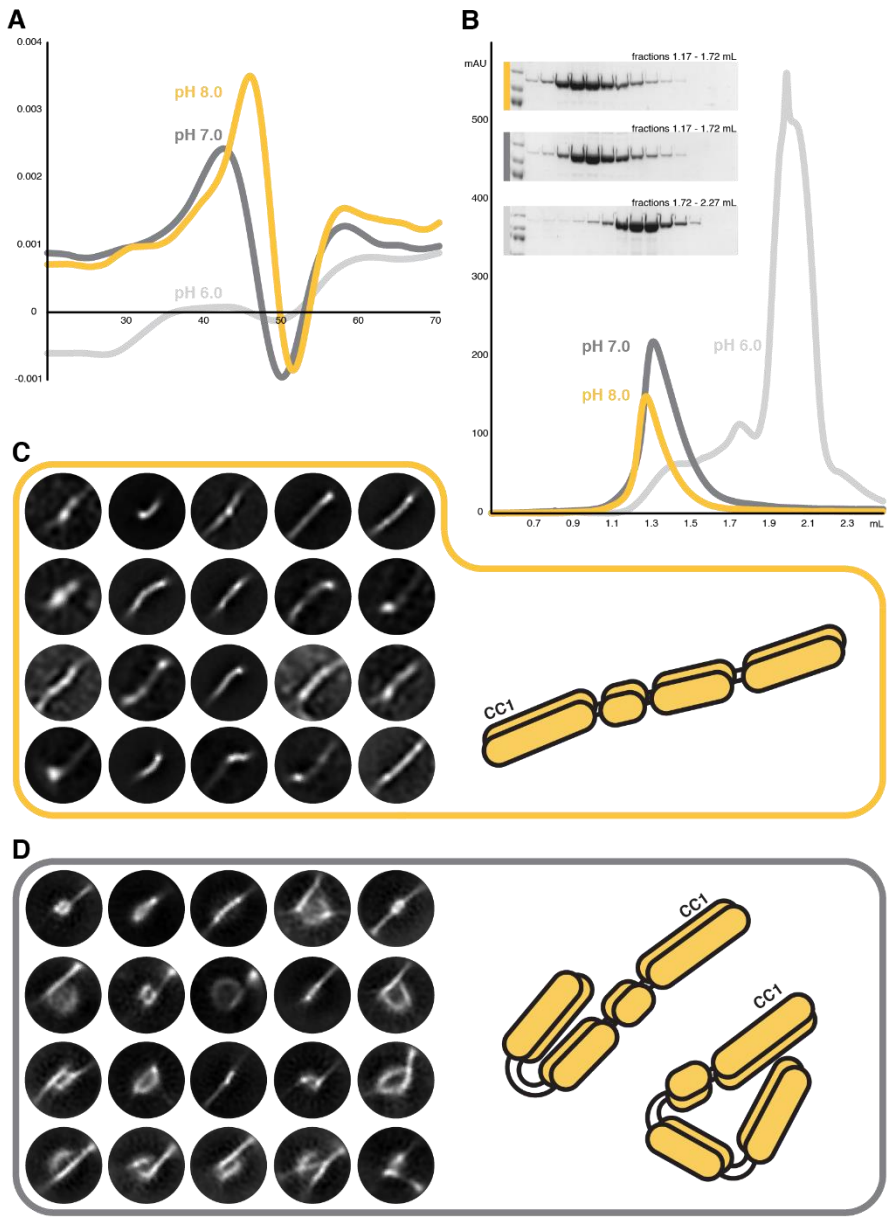

Figure 2. A First-derivative of the DSF melting curves at three different pH values. The curves at pH 7.0 and pH 8.0 display main inflection point in the range of 47-50°C. The curve at pH 6.0 doesn't show a distinct inflection point. Each measurement was repeated 3 times. **B** SEC profiles of BicD2 run at three different pH values. Each sample was run twice on a Superose® 6 Increase column to ensure clean peak fractions. **C** and **D** Representative cryoEM 2D classes from ~700 micrographs (per pH condition). The yellow box represents classes from pH 8.0 while the grey box from pH 7.0. In both cases we processed the data with Relion3.1.

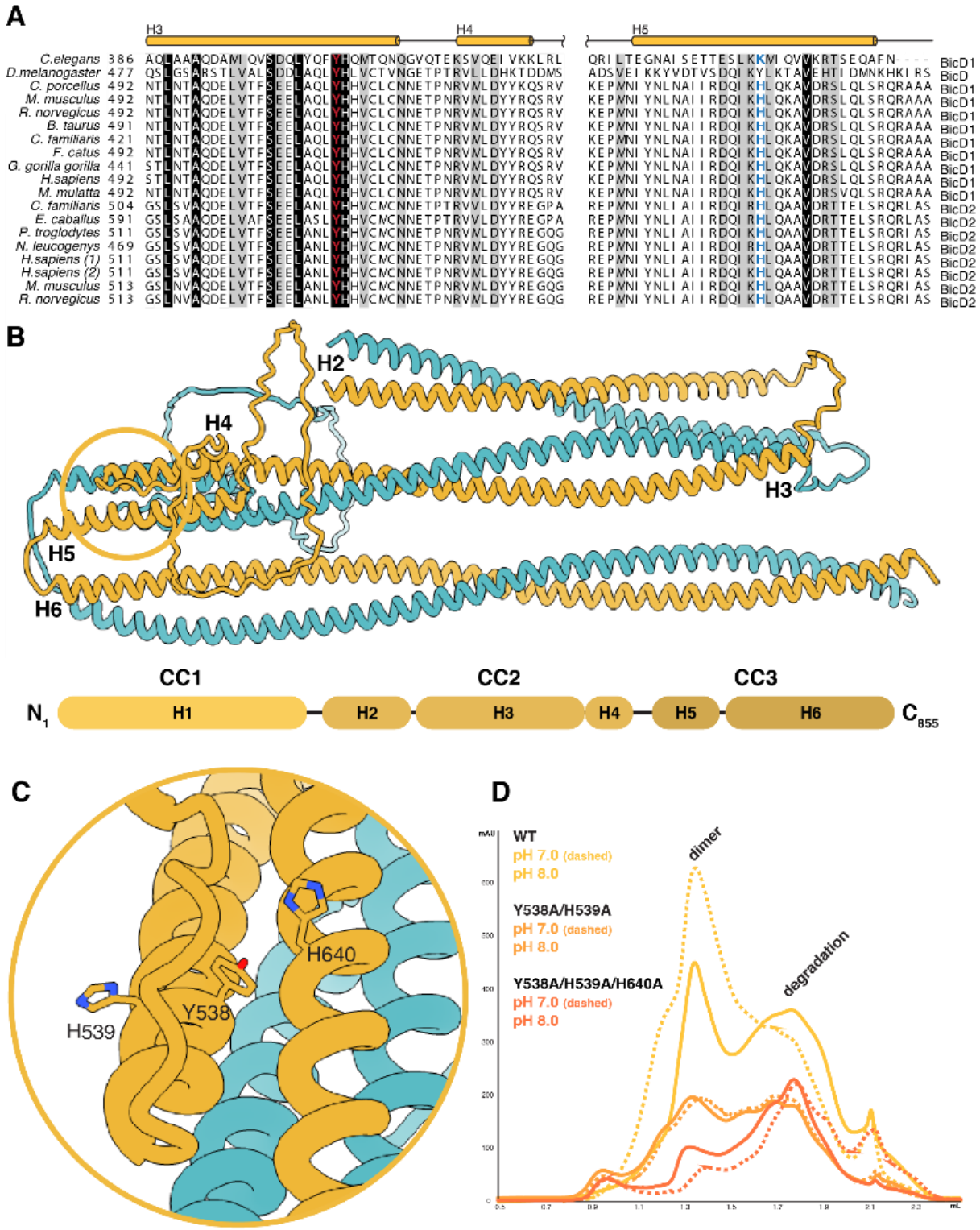
A
H3
H4
H5
C.elegans 386 AQLAAAAQDAMIQVSDQLYQFYHQMTQNQGVQTEKSVQEIVKKLRL QRILTEGNAISETTESLKKMIQVVKRTSEQAFN BicD1
D.melanogaster 477 QSLGSARSTLVALSDDLAQLYHLVCTVNGETPTRVLLDHKTDDMS ADSVEIKKYVDTVSDQIKYLKTAVEHTIDMNKHKIRS BicD
C. porcellus 492 NTLNTAQDELVTFSEELAQLYHVCLCNNETPNRVMLDYYKQSRV KEPMNIYNLNAIIRDQIKHLQKAVDRSLQLSRQRAAA BicD1
M. musculus 492 NTLNTAQDELVTFSEELAQLYHVCLCNNETPNRVMLDYYRQSRV KEPMNIYNLNAIIRDQIKHLQKAVDRSLQLSRQRAAA BicD1
R. norvegicus 492 NTLNTAQDELVTFSEELAQLYHVCLCNNETPNRVMLDYYRQSRV KEPMNIYNLNAIIRDQIKHLQKAVDRSLQLSRQRAAA BicD1
B. taurus 491 NTLNTAQDELVTFSEELAQLYHVCLCNNETPNRVMLDYYRQSRV KEPMNIYNLNAIIRDQIKHLQKAVDRSLQLSRQRAAA BicD1
C. familiaris 421 NTLNTAQDELVTFSEELAQLYHVCLCNNETPNRVMLDYYRQSRV KEPMNIYNLNAIIRDQIKHLQKAVDRSLQLSRQRAAA BicD1
F. catus 492 NTLNTAQDELVTFSEELAQLYHVCLCNNETPNRVMLDYYRQSRV KEPMNIYNLNAIIRDQIKHLQKAVDRSLQLSRQRAAA BicD1
G. gorilla gorilla 441 STLNTAQDELVTFSEELAQLYHVCLCNNETPNRVMLDYYRQSRV KEPMNIYNLNAIIRDQIKHLQKAVDRSLQLSRQRAAA BicD1
H.sapiens 492 STLNTAQDELVTFSEELAQLYHVCLCNNETPNRVMLDYYRQSRV KEPMNIYNLNAIIRDQIKHLQKAVDRSLQLSRQRAAA BicD1
M. mulatta 492 NTLNTAQDELVTFSEELAQLYHVCLCNNETPNRVMLDYYRQSRV KEPMNIYNLNAIIRDQIKHLQKAVDRSVQLSRQRAAA BicD1
C. familiaris 504 GSLSVAQDELVTFSEELANLYHVCMCNNETPTRVVLDYYREGPA REPMNIYNLIAIIRDQIRHLQAAVDRTTELSRQRLAS BicD2
E. caballus 591 GSLSAAQDELVAFSEELASLYHVCMCNNETPTRVVLDYYREGPA REPMNIYNLIAIIRDQIRHLQAAVDRTTELSRQRLAS BicD2
P. troglodytes 511 GSLSVAQDELVTFSEELANLYHVCMCNNETPNRVMLDYYREGQG REPMNIYNLIAIIRDQIKHLQAAVDRTTELSRQRIAS BicD2
N. leucogenys 469 GSLSVAQDELVTFSEELANLYHVCMCNNETPNRVMLDYYREGQG REPMNIYNLIAIIRDQIRHLQAAVDRTTELSRQRLAS BicD2
H.sapiens (1) 511 GSLSVAQDELVTFSEELANLYHVCMCNNETPNRVMLDYYREGQG REPMNIYNLIAIIRDQIKHLQAAVDRTTELSRQRIAS BicD2
H.sapiens (2) 511 GSLSVAQDELVTFSEELANLYHVCMCNNETPNRVMLDYYREGQG REPMNIYNLIAIIRDQIKHLQAAVDRTTELSRQRIAS BicD2
M. musculus 513 GSLNVAQDELVTFSEELANLYHVCMCNNETPNRVMLDYYREGQG REPMNIYNLIAIIRDQIKHLQAAVDRTTELSRQRIAS BicD2
R. norvegicus 513 GSLNVAQDELVTFSEELANLYHVCMCNNETPNRVMLDYYREGQG REPMNIYNLIAIIRDQIKHLQAAVDRTTELSRQRIAS BicD2
B
H2
H4
H3
H5
H6
CC1
CC2
CC3
N1
H1
H2
H3
H4
H5
H6
C855
C
H640
Y538
H539
D
mAU
WT
pH 7.0 (dashed)
pH 8.0
Y538A/H539A
pH 7.0 (dashed)
pH 8.0
Y538A/H539A/H640A
pH 7.0 (dashed)
pH 8.0
dimer
degradation
mL

Figure 3. A Sequence alignment of the tri-helical domain (H3, H4, and H5 helix) of D. melanogaster, C. elegans, and mammalian BicD1 and BicD2 isoforms. The conserved Y538 is marked in red, and H640 in blue. **B** Structure prediction of the BicD2 CC2 and CC3 dimer with AlphaFold2. The C-terminal loop of CC3 has been deleted for clarity reasons. **C** Zoom into the conserved histidine and tyrosine that are crucial for the protein stability. **D** Chromatograms of affinity purified BicD2 variants. In yellow - WT, orange - Y538A/H539A double mutant, dark orange - Y538A/H539A/H640A triple mutant. In all chromatograms the solid line represents pH8.0, and the dashed line pH 7.0. For each construct an identical protein amount was loaded.

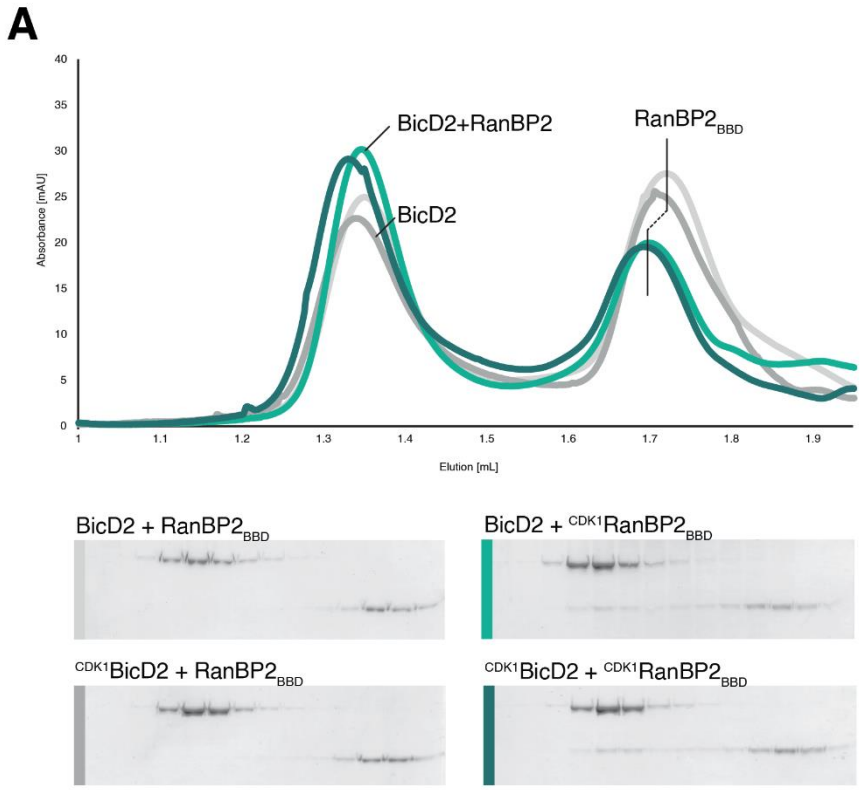
A
BicD2+RanBP2
RanBP2BBD
BicD2
Absorbance [mAU]
Elution [mL]
BicD2 + RanBP2BBD
BicD2 + CDK1RanBP2BBD
CDK1BicD2 + RanBP2BBD
CDK1BicD2 + CDK1RanBP2BBD

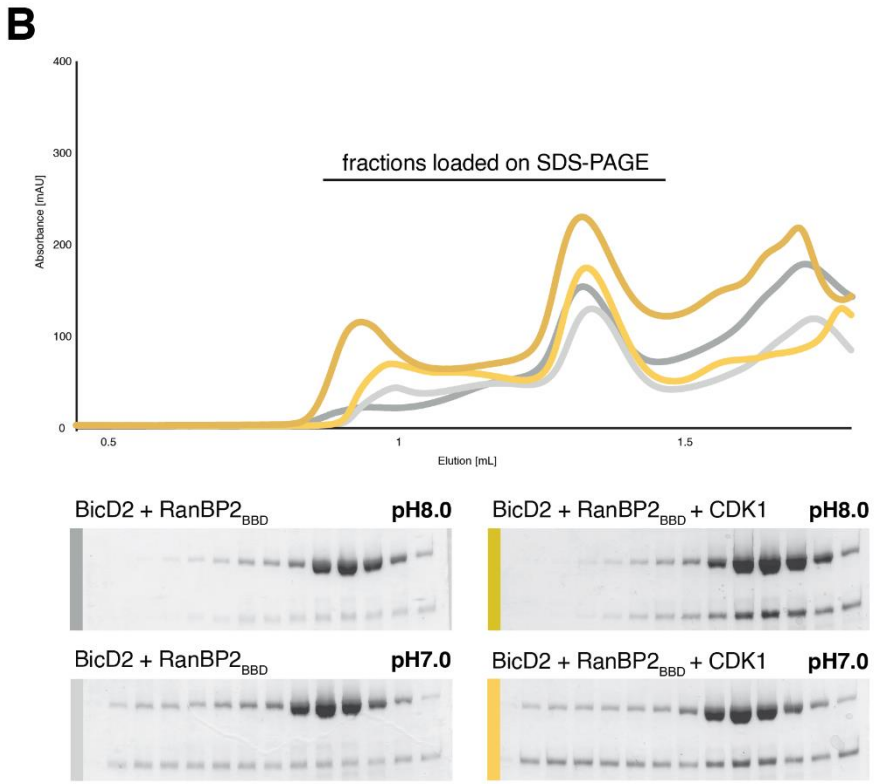
B
fractions loaded on SDS-PAGE
Absorbance [mAU]
Elution [mL]
BicD2 + RanBP2BBD pH8.0
BicD2 + RanBP2BBD + CDK1 pH8.0
BicD2 + RanBP2BBD pH7.0
BicD2 + RanBP2BBD + CDK1 pH7.0

Figure 4. SEC profiles of the BicD2 reaction with $RanBP2_{BBD}$ with or without action of the $CDK1^{CyclinB}$ complex. **A** Purified proteins were mixed at a 1:1 molar ratio and incubated for 30 minutes at RT. In light grey a chromatogram of unphosphorylated BicD2 and unphosphorylated $RanBP2_{BBD}$. In dark grey $CDK1^{CyclinB}$ phosphorylated BicD2 with unphosphorylated RanBP2. In light green unphosphorylated BicD2 with $CDK1^{CyclinB}$ phosphorylated RanBP2, and dark green represents both proteins being $CDK1^{CyclinB}$ phosphorylated. All reactions were performed at pH 8.0 **B** Pull-down of affinity-purified BicD2, $RanBP2_{BBD}$, at two different pH values with or without $CDK1^{CyclinB}$. The dark yellow chromatogram represents BicD2, $RanBP2_{BBD}$, and $CDK1^{CyclinB}$ pull-down at pH 8.0, while light yellow shows the same reaction but at pH 7.0. Dark and light grey chromatogram show the same reactions but without activity of $CDK1^{CyclinB}$ complex (at pH 8.0 and pH 7.0 respectively).

Supplementary figures

A

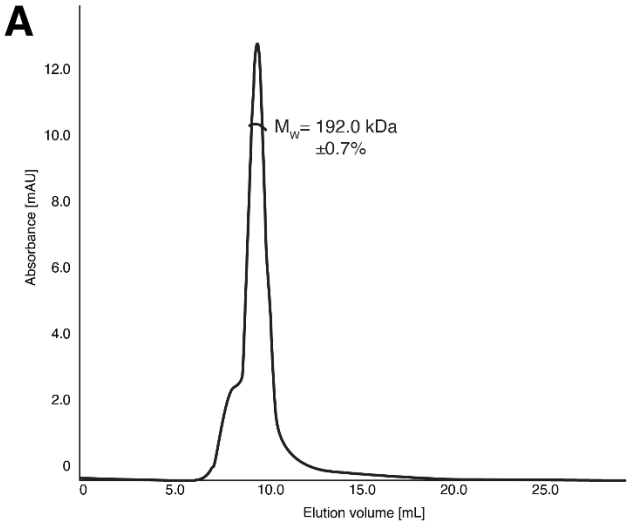

B

	Charge, z	Net charge at pH7.4	Isoelectric point
$BicD2_{FL}$	-16.61 (pH6.0)	-31.92	5.37
	-29.52 (pH7.0)		
	-35.66 (pH8.0)		

C

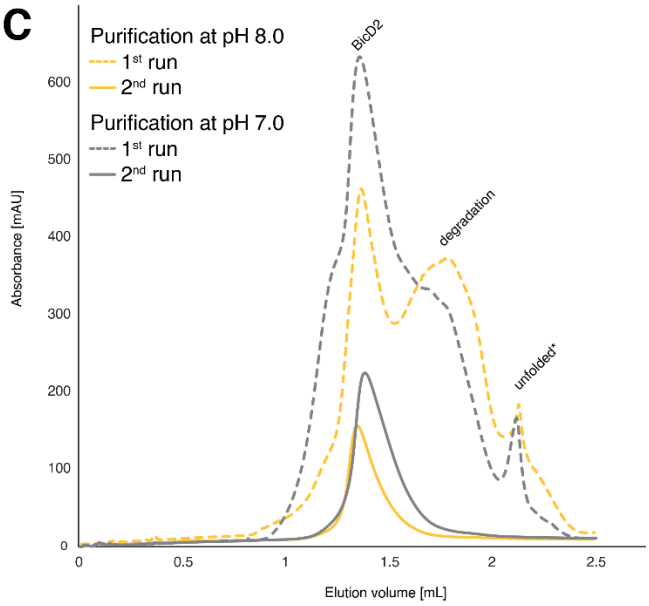

Supplementary figure 1. A The SEC-MALS profile of the pre-purified BicD2. **B** Table with BicD2 charge values at specific pH. To generate this data we used 'Prot pi' bioinformatic tool box for the calculation and simulation of physico-chemical parameters of proteins (Release: 2.2.29.150). **C** The SEC profile of an affinity purified full-length BicD2. The grey chromatogram represents the sample ran at pH 7.0, and the yellow chromatogram is the sample ran at pH 8.0. In both cases an identical protein amount was loaded on to the Superose® 6 Increase column.

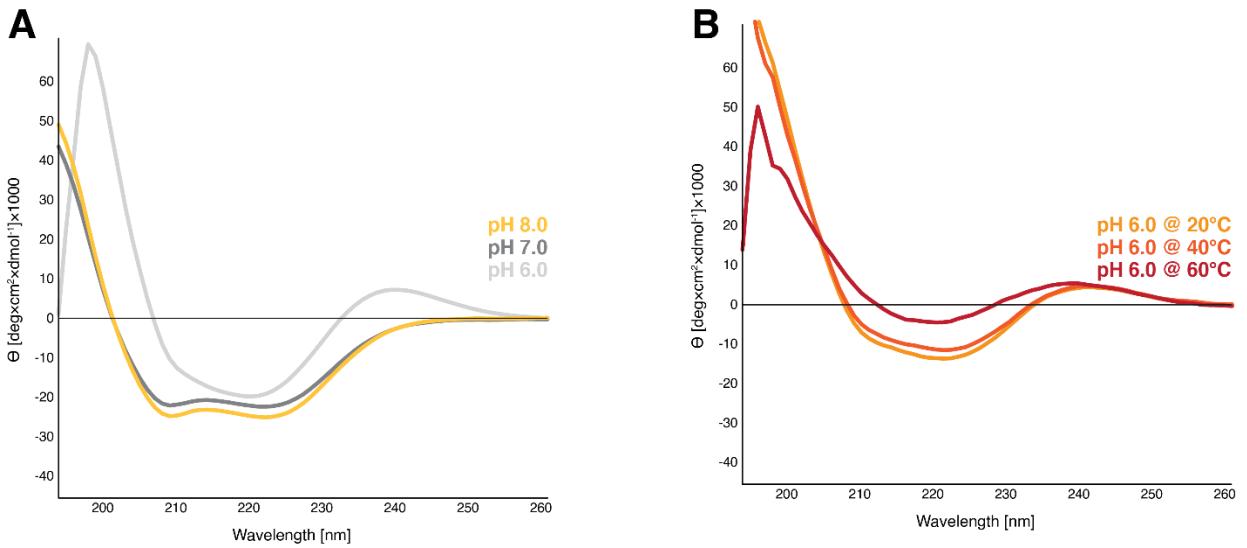

Supplementary figure 2. **A** CD spectra of the full-length BicD2 at pH value of 6.0, pH 7.0, and pH 8.0. All three runs were done at 20°C. **B** CD spectra of the full-length BicD2 at pH 6.0 at three temperatures (20, 40, and 60°C). Prior to the experiment each BicD2 sample was run twice on SEC in PBS buffer at the respective pH.

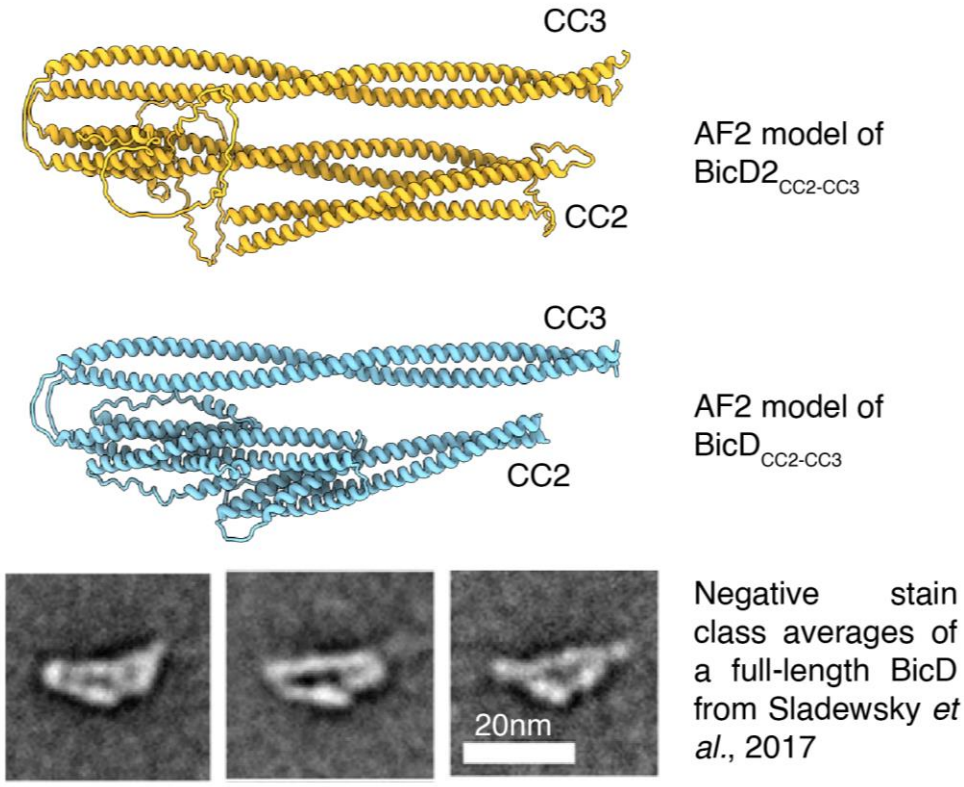

Supplementary figure 3. Comparison of the AF2-predicted human BicD2$_{CC2-CC3}$, fruit fly BicD$_{CC2-CC3}$, and negative stain class-averages of the full-length BicD.

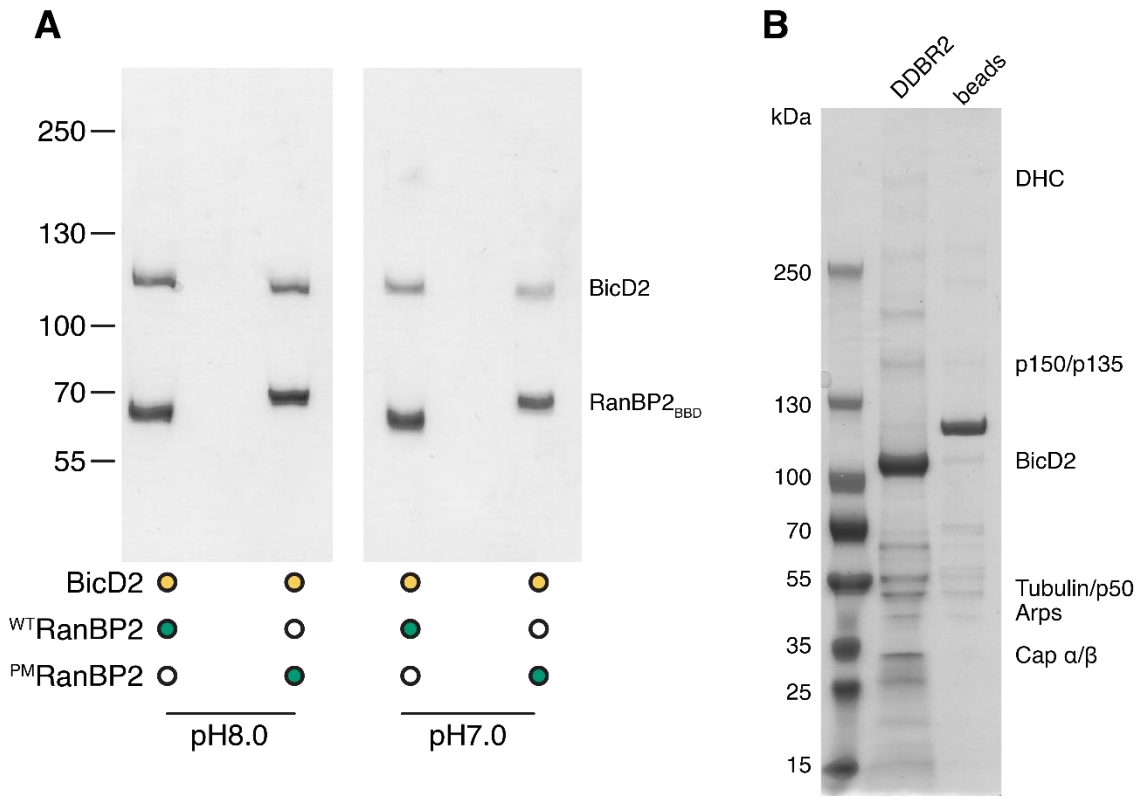

Supplementary figure 3. A The double pull-down of the BicD2-RanBP2$_{BBD}$ complex. The first pull-down was done on Strep-tagged BicD2 followed by 6xHis-tagged RanBP2. The complex was pulled with either RanBP2$_{BBD}$ (RanBP2$_{BBD}$-WT) or the phosphomimetic mutant of RanBP2$_{BBD}$ (RanBP2$_{BBD}$-PM) and at two different pH values. **B** The BicD2 pull-down from the rat brain lysate indicating the DDB complex characteristic bands. The dynein heavy chain and p150 bands were confirmed by MS.

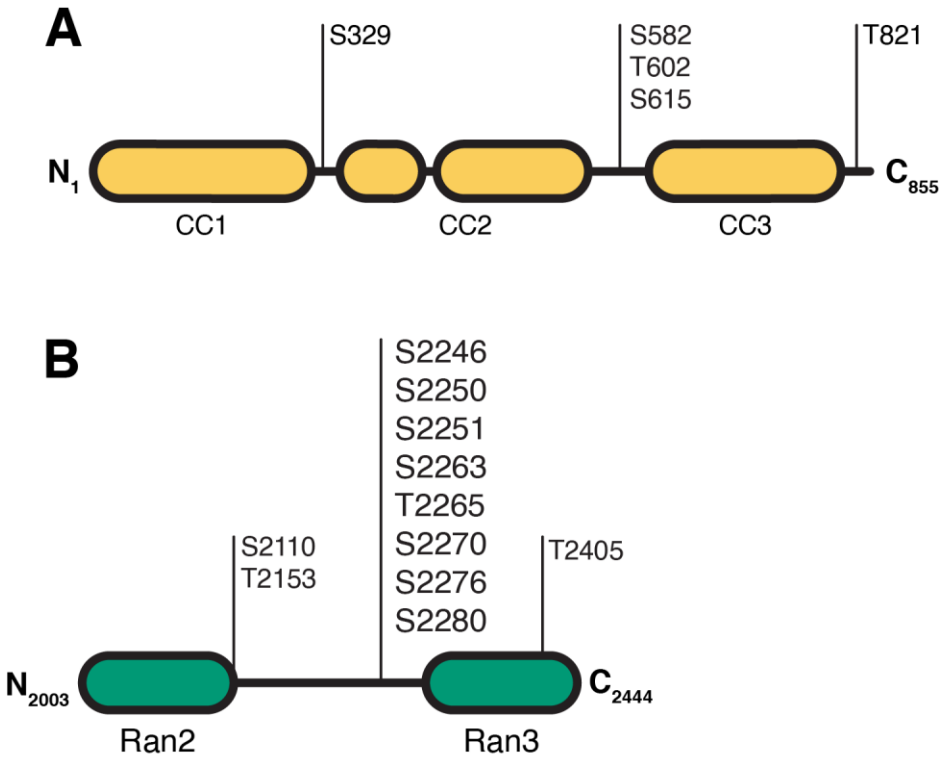

Supplementary figure 4. CDK1-CyclinB phosphorylation profile of BicD2 and RanBP2. **A** BicD2 contains five S/T sites within its sequence in structurally disordered regions. **B** $RanBP2_{BBD}$ contains multiple phosphorylation sites within the structurally disordered region between the Ran2 and Ran3 domains, which is also the BicD2 binding site.

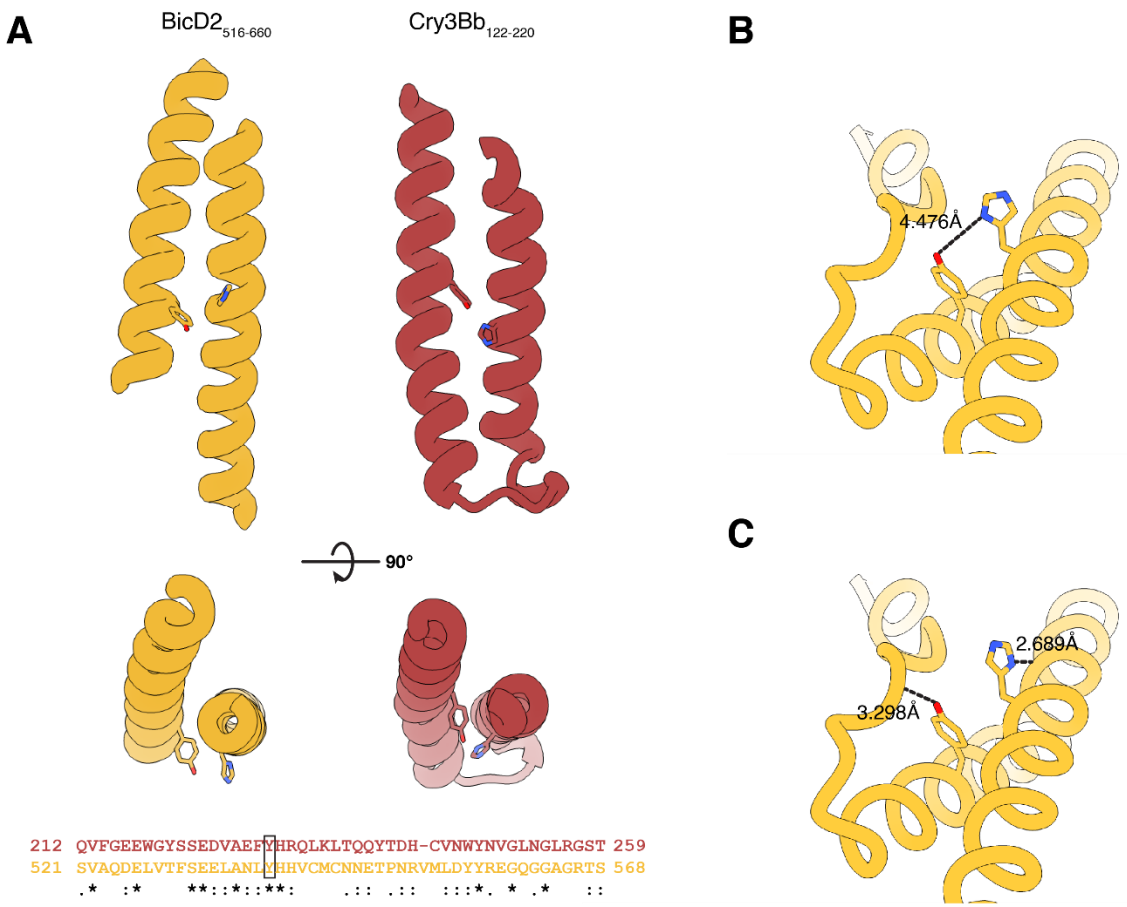

Supplementary figure 5. A Structure comparison of the computational structure of BicD2 H3-H4-H5 α-helical bundle fragment and analogous region in Cry3Bb endotoxin (PDB ID: 1CIY) and sequence alignment of the tyrosine containing helix. Loops removed for clarity reasons. **B** and **C** Probable rotamers of the H640 and respective distance from Y538.

3.2 Supplementary data

3.2.1 Human BicD2 expression and solubilisation

The gene encoding the human BicD2 isoform 2 was codon-optimized for bacterial expression in a pNHD vector, a plasmid used for site-specific unnatural amino-acid incorporation,[238] but I also observed reproducible protein expression levels in commercial vectors, such as pMMS. The gene was fused with either an N-terminal 6xHis or a StrepII tag to aid protein purification. Protein overexpression and purification is described in the attached manuscript.

For all bacterial expressions described here I used the Escherichia coli BL21(DE3) strain with no supplementary plasmids. Even though the protein was well expressed (Figure 18A), the vast majority of the protein was found in the pellet after cell lysis and centirfugation. In order to solubilize the protein, I decided to optimize first the expression conditions. In my conditions the shorter expression times gave significantly more protein (maximum 3.5h at 37°C) compared to the overnight cultures in the temperature range from 12 to 24°C, and none of these conditions affected the protein solubility. After finding the optimal expression time and temperature I decided to optimize the chemical parameters of protein expression by: decreasing the IPTG concentration from the 1mM to 0.1mM as IPTG is generally toxic to cells and often lower concentrations give better or equal results; overexpressing in the presence of 1-3% ethanol;[239] adding a mixture of arginine and glucose;[240] and heat shocking the culture upon expression induction.[241] These expression methods have been shown to increase the soluble fraction of the protein. All of these had little to no effect on protein solubility, and only in the standard expression protocol (3h overexpression at 37°C, 1mM IPTG) and heat-shocked cultures prepared as described by Chen et al., (2002) I observed a minor soluble fraction in the supernatant (Figure 18A). I loaded the soluble fraction from the standard expression protocol on a Superose® 6 column to check if the protein elutes as a homogenous peak. Based on the SEC profile it is most likely a non-functional protein as it contains several full-length BicD2 species throughout the elution (Figure 18B).

As an alternative approach for BicD2 solubilisation, I decided to purify the insoluble protein fraction under non-native conditions. The non-native purification principally consists of four steps: isolation and purification of inclusion bodies;

solubilisation of the inclusion bodies (unfolding); refolding of the solubilized proteins; and purification of the refolded proteins. At the refolding stage, the protein precipitated instantly upon decrease of the guanidine concentration, which prevented further purification (for details see Methods chapter).

Another attempt towards BicD2 solubilisation that I tried was fusion constructs with solubilizing tags. With standard cloning methods, I generated N- or C-terminal BicD2 fusions with: superfolding GFP; lipoyl domain; MBP; or trigger factor. None of these tags had an effect on BicD2 solubility as the major fraction of the protein remained in the pellet after cell lysis.

The full-length BicD2 was successfully solubilized upon addition of a detergent. Addition of non-denaturing detergents is a common practice in membrane biochemistry and for many hydrophobic proteins.[242] Among many commercial compounds the most commonly used detergents are non-ionic compounds such as Triton-X, NP40, and Tween20, and zwitterionic compounds such as CHAPS and CHAPSO.[243] CHAPS is often the preferred detergent in protein extraction and solubilisation due to its mild chemical nature and can be removed by dialysis unlike the non-ionic detergents.[244] Addition of 7mM CHAPS solubilized the majority of the protein in a dimeric form (Figure 18C) as confirmed by SEC-MALS analysis.

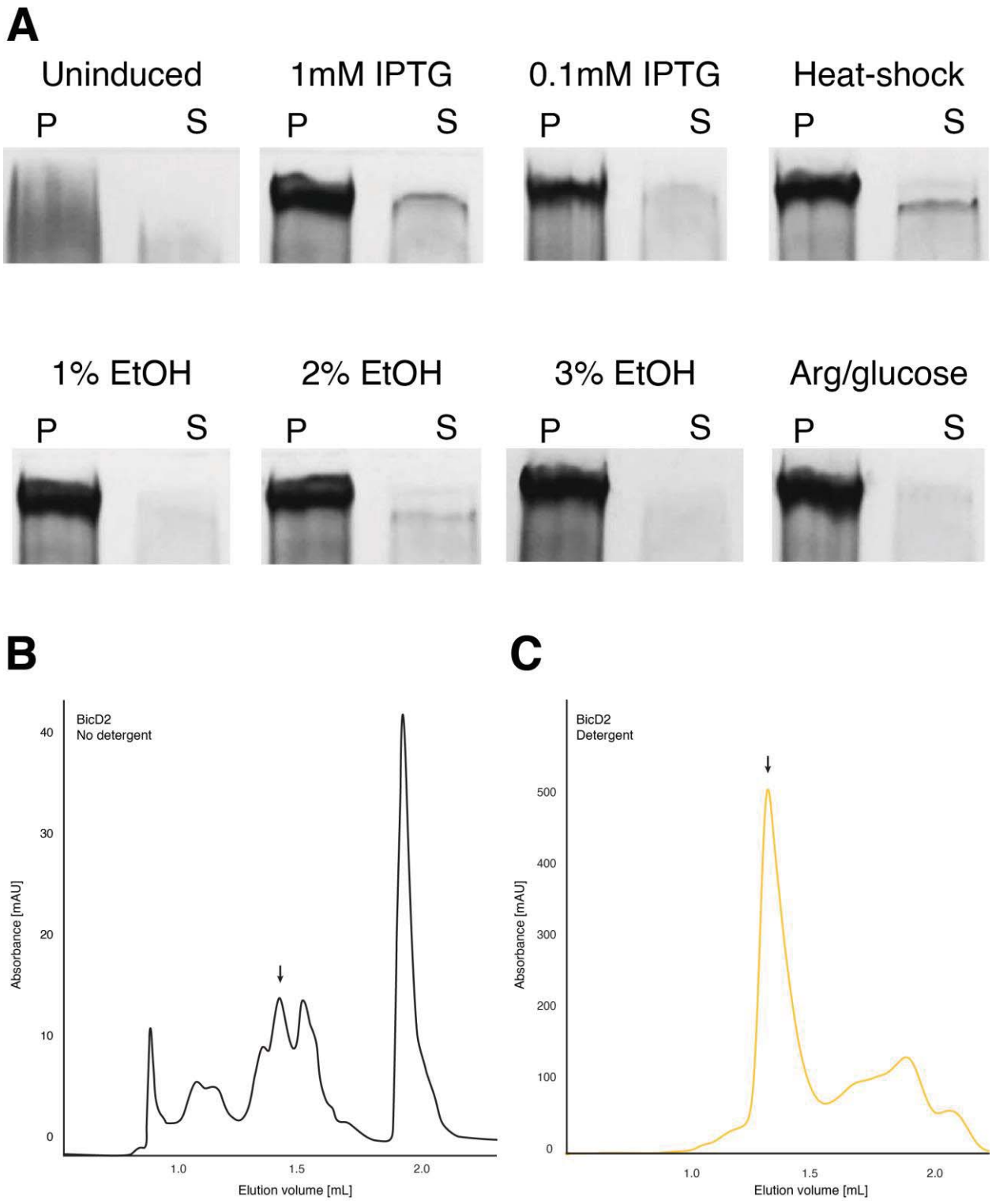

Figure 18. Expression and purification of the full-length BicD2. **A** BicD2 expression optimization. Uninduced lane shown as a control. 'P' indicates pellet and 'S' supernatant. Minor soluble fractions observed in 1mM IPTG, heat-shock, and 2% EtOH conditions. **B** BicD2 SEC profile of minor soluble fraction from standard expression protocol (3h overexpression at 37°C, 1mM IPTG). All elution peaks correspond to the full-length BicD2. **C** SEC run of CHAPS-solubilized BicD2. The arrow represents the BicD2 elution peak.

3.2.2 Negative stain BicD2 characterization

To confirm that the solubilized protein is well-folded and stable, I used several biophysical methods: circular dichroism (CD) to quantify the secondary structure content; differential scanning fluorimetry (DSF) to find an optimal buffer composition; negative stain electron microscopy to check the overall shape and conformational homogeneity; and cryoEM for the direct protein visualization under native conditions. The DSF, CD, and cryoEM experiments are described in the manuscript. In short, the DSF melting curves revealed that BicD2 is very sensitive to changes in the pH. The CD experiment has shown the primarily α-helical content of the BicD2 sample at pH7.0 and 8.0, but not for pH6.0 as protein is partly unfolded at that pH. In the cryoEM section

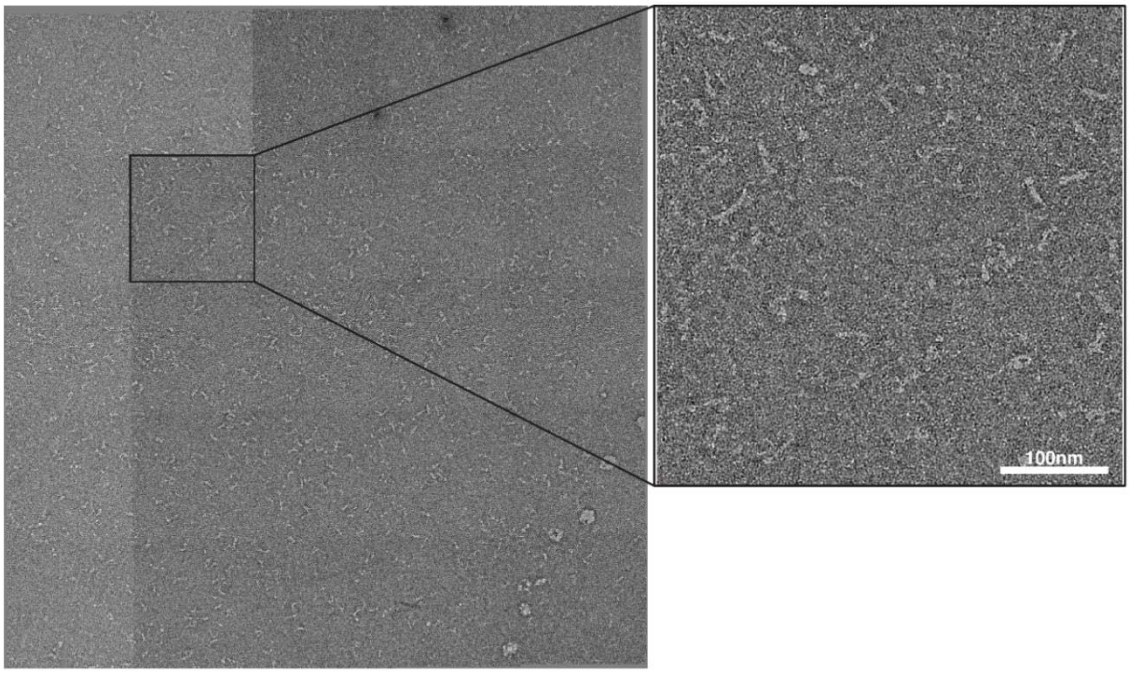

Figure 19. Negative stain image of the full-length BicD2.

I have shown that BicD2 exists in different conformations induced by changes in the pH between 7.0 and 8.0. For the negative stain electron microscopy analysis I purified the protein at pH 7.0 as it is more stable. I used a protein concentration of 10nM with no detergent. The grids were stained with a 2% uranyl acetate solution and imaged using a Tecnai G2 200kV TEM. An example image is shown in Figure 19. The sample showed a good particle distribution throughout the grid, and I collected several micrographs to check for the sample quality. The micrographs shows no signs of aggregation and an approximate particle size of 50 nm, which indicates proper protein folding consistent with other negative stain experiments reported for Drosophila BicD.[170]

3.2.3 RanBP2$_{BBD}$ production, phosphorylation, and stability

After successfully producing recombinant and soluble BicD2 I worked on the BicD2-binding RanBP2 truncation. The ~53kDa RanBP2$_{BBD}$ fragment production in bacteria has already been reported. [26,245] In short, the GOI was inserted into a pNHD vector and fused with a 6xHis tag at the C-terminus. Protein expression was induced with 1mM IPTG in E. coli BL21(DE3) strain for ~3h. Protein was extracted and purified similarly to BicD2. One litre of culture yielded around 1mg of a protein. RanBP2$_{BBD}$ is also prone to continuous degradation and I found it difficult to stabilize it in solution. I fused the protein with different purification tags (6xHis, GST, or MBP) but it did not seem to influence the stability. I decided to work with the 6xHis-tagged protein for further experiments. The best strategy to recover a majority of the intact protein, was to reduce the expression time in E.coli to a minimum, and to perform the purification under non-native conditions. In short, the protein was extracted and unfolded with 6M Urea and purified on a Ni-NTA resin and either refolded on the SEC column or dialysed against a target buffer (see Methods for the detailed protocol). Although protein unfolding and refolding is rarely advised it did reduce the degradation rate significantly and it should not interfere with reactivity as the BicD2 binding region of RanBP2$_{BBD}$ is predicted to be intrinsically disordered.[246]

Moreover, for the interaction with BicD2 it is known that RanBP2$_{BBD}$ needs to be CDK1-phosphorylated. I wondered if phosphorylation could stabilize the protein to any extent but unfortunately the protein degraded even quicker compared to the unmodified protein (Figure 20). On the other hand phosphorylation of RanBP2$_{BBD}$ narrows the pool of RanBP2$_{BBD}$ species on SEC. The unmodified protein gives several peaks unlike the phosphorylated variant which normally gives two elution peaks: the monomeric protein (based on elution volume) and degradation products. I also attempted RanBP2$_{BBD}$ expression in a eukaryotic system (Sf9) but it degraded instantly upon purification which made it difficult to perform the reconstitution experiments or elaborate the biophysical characterization steps.

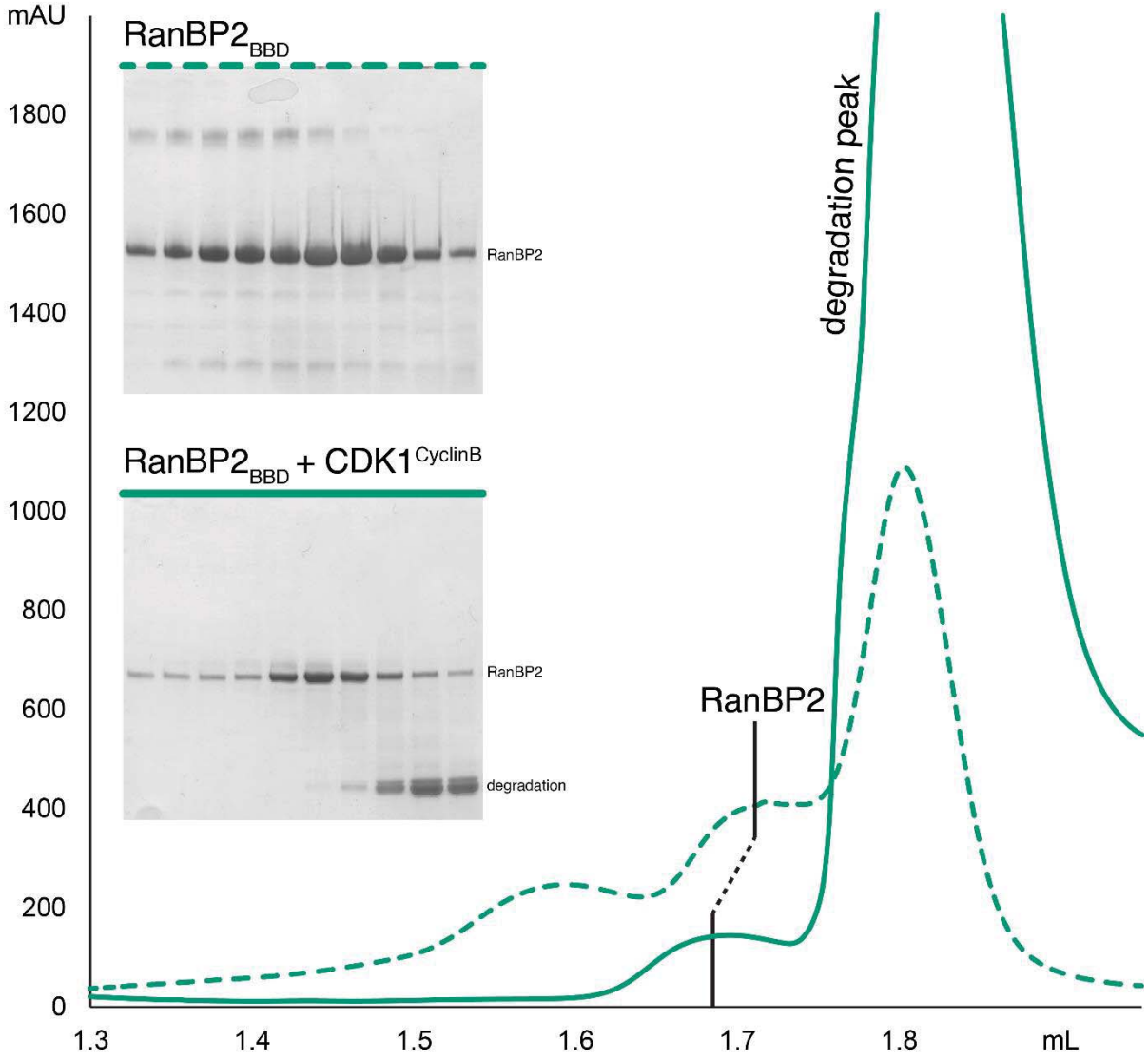

Figure 20. SEC profile of the unmodified $RanBP_{BBD}$ (dashed line) and CDK1-modified $RanBP2_{BBD}$ (solid line).

I then decided to reconstitute the complex between the two proteins: full-length BicD2 and $RanBP2_{BBD}$. For reconstituting the BicD2 and RanBP2 complex it had been shown that the intrinsically disordered region in $RanBP2_{BBD}$ needs to be CDK1-phosphorylated.[245] When I started my degree there were no efficient methods for recombinant and active CDK1 kinase production. For that reason I implemented four alternative strategies to produce phosphorylated RanBP2: (1) incorporation of the unnatural amino acid (UAA) phosphoserine (pSer);[238] (2) phosphorylation with the alternative kinases ERK2, JNK1, and p38; (3) phosphomimetic mutations; and (4) protein production in the Sf9 eukaryotic system that yields unspecific phosphorylation. For the unnatural amino acid system I identified four serines (S2246, S2251, S2276, and S2280) that can potentially be modified into phosphorylated residues. The

unnatural amino acid system involves repurposing key parts of a cell's translation machinery - tRNA and aminoacyl-tRNA synthetase, to incorporate an unnatural amino acid site selectively within a protein. The aminoacyl-tRNA synthetase (aaRS)/tRNA pairs translate 61 of the 64 codons into the 20 canonical amino acids. This leaves 3 stop codons that terminate the translation machinery and that can be conveniently used in UAA incorporation. In this case the phosphoserine-charged orthogonal tRNA was used for site specific pSer incorporation. Sometimes the stop codon is not recognized by the orthogonal tRNA on time which can stop translation machinery. This results in a truncated protein hence I moved the purification tags to the C-terminus to extract only the full-length protein. Also, for all possible mutants attempted, only two phosphoserines (S2246 and S2251) were incorporated without noticeable effect on expression levels. Incorporation of three residues also worked, but with a significant drop in expression levels (Figure 21). Successful pSer incorporation was confirmed with MS. The quadruple mutant did not yield a purifiable amount of protein.

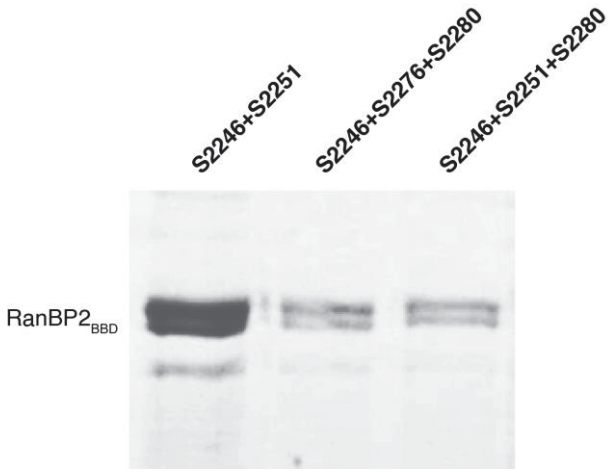

Figure 21. SDS-PAGE of the $RanBP2_{BBD}$ with incorporated unnatural amino acids. Left: $RanBP2_{BBD}$ with two phosphoserines, middle and right: two $RanBP2_{BBD}$ variants with three phosphoserines incorporated.

As incorporation of two pSer worked well, I used that mutant for further in-vitro kinase assays with ERK2, JNK1, and p38 to quantify the modified S/T sites. The alternative kinases together with unnatural pSer residues were not able to phosphorylate all CDK1

Table 3. List of $RanBP2_{BBD}$ residues modified in vitro by ERK2, JNK1, p38, and CDK1 kinases. The dots in blue indicate the $RanBP2_{BBD}$ with two phosphoserines incorporated prior to the in vitro kinase assay.

Residue	ERK2	JNK1	p38	CDK1	
S2110	•	•		•	
T2153	•	•	•	•	
T2160	•		•		
S2175	•				
T2182		•			
S2246	•	•	•	•	BicD2-binding region
S2250				•	
S2251	•	•	•	•	
S2263				•	
T2265	•		•	•	
T2270				•	
S2273	•				
S2276				•	
S2278	•				
S2280	•	•	•	•	
T2289			•		
T2387	•		•		
T2441			•		

consensus amino acids in $RanBP2_{BBD}$. While some of them overlap significantly with consensus sites of CDK1, only CDK1 is able to uniquely phosphorylate the BicD2 binding region (T2153, S2246, S2251, S2276, and S2280). The relative S/T positions phosphorylated by all four kinases are listed in Table 2 with S2246 and S2251 marked in blue as they were incorporated with the UAA system. The third and fourth approach in $RanBP2_{BBD}$ modification was mutation of the S/T sites into phosphomimetic residues and protein expression in a eukaryotic system. To generate the phosphomimetic mutant I applied classical cloning methods for introduction of 5 point mutations (T2153D, S2246D, S2251D, S2276D, and S2280D) and produced the protein as for the WT in E. coli. For expression in Sf9, I re-cloned the $RanBP2_{BBD}$ gene with purification tags into the pLIB vector and generated baculovirus for insect cell infection. For detailed steps of baculovirus generation and infections please refer to the methods chapter.

3.2.4 BicD2-RanBP2$_{BBD}$ complex reconstitution

The primary method for complex reconstitution in my work was the pull-down approach. Two differently tagged proteins were mixed together and affinity-purified on first tag, followed by another affinity step using the second protein tag. Human BicD2 was fused with an N-terminal StrepII tag to be affinity purified on Strep-Tactin resin, while RanBP2$_{BBD}$ had a C-terminal 6xHis tag allowing purification by Ni-NTI agarose beads.

To reconstitute the BicD2:RanBP2$_{BBD}$ complex, I produced several RanBP$_{BBD}$ variants: the wild type, and the four variants described above - (1) unnatural amino acids variant with two phosphoserines; (2) ERK2, JNK1, p38, and CDK1-modified RanBP2$_{BBD}$; (3) phosphomimetic mutant; and (4) Sf9-produced protein.

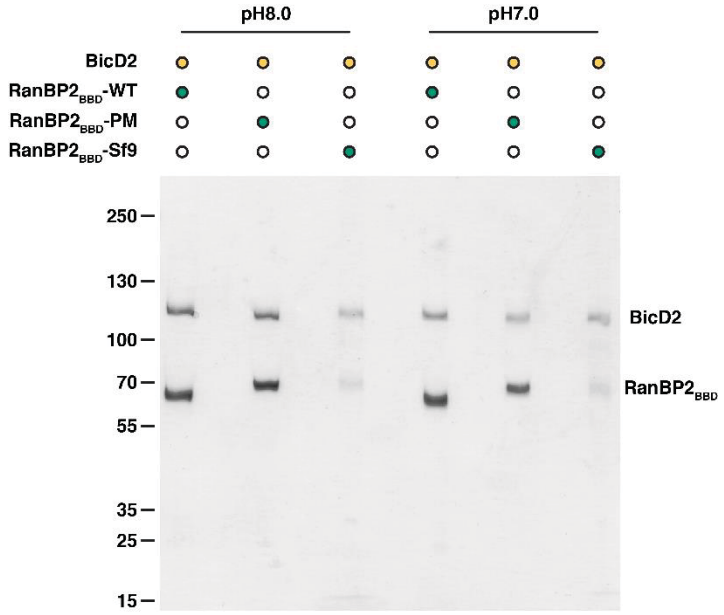

Figure 22. Double pull-down of the BicD2:RanBP2$_{BBD}$ complex. For each reaction an identical protein fragment was used. WT – wild type protein expressed in bacteria, PM – phosphomimetic mutant expressed in bacteria, Sf9 – wild type protein expressed in insect cells.

In the double pull-down experiments selected RanBP2$_{BBD}$ variants (WT, phosphomimetic, and Sf9-expressed) seem to interact well with BicD2 (Figure 22). The two proteins can form a stoichiometric (based on band intensities) complex through weak interactions. In addition I performed the same pull-downs at pH 7 and pH 8 to investigate if the different BicD2 conformations can potentially influence the complex formation. The pH value had no effect in double pull-downs. I did not use the unnatural amino acid variant in my studies as two phosphoserines were not enough

to yield a visible amount of the complex on SEC. Similarly ERK2, JNK1, and p38 did not yield a significant amount of the complex, probably due to incomplete phosphorylation of the BicD2 binding region. On the other hand, CDK1 modification facilitated efficient complex formation between BicD2 and $RanBP2_{BBD}$. Details of that approach are also shown in the attached manuscript. The phosphomimetic mutant did not form a stable complex that would not dissociate over SEC. Last but not least, the Sf9-expressed protein was degrading very fast, which did not allow me to use it for elaborate interatomic studies. Taken together the two proteins seem to interact well in the double pull-downs experiments independently from chemical modifications such as phosphorylation or pH value. Nevertheless over the SEC runs the complexes seem to dissociate quickly, implying a weak range of interaction between unmodified proteins. CDK1 modification and increased pH value significantly strengthen the interaction.

3.2.5 DDB and DDBR2 complex pull-down

After reconstituting the BicD2:$RanBP2_{BBD}$ complex I decided to reconstitute a larger complex between dynein-1, dynactin, BicD2, and $RanBP2_{BBD}$ (DDBR2) even though recombinant expression of the dynein-1 complex and dynactin is very challenging. In the interest of time, I decided to follow approaches that extract dynein and dynactin from endogenous sources, such as mouse, rat, or pig brain. It was shown that an intact dynein-dynactin-BicD2N (DDB, where BicD2N is a N-terminal truncation of BicD2) can be pelleted from mice brains in a functional form.[152] It also had been demonstrated that dynactin can be purified to homogeneity from porcine brains.[132]

I decided to attempt a pull-down experiment from rat brain lysates. The rats were obtained from the animal house at the institute which allowed me to extract the rat brains freshly. Details of this protocol are described in the methods section.

To pull-down the intact DDB or DDBR2 complexes from rat brain lysates, I have used either BicD2 or $RanBP2_{BBD}$ as a bait. Both proteins have worked in principle and were able to pull-down dynein- and dynactin-specific bands. The Strep-tagged BicD2 as a bait gave significantly cleaner eluates. This is mostly due to better Strep-tag:resin affinity compared to the 6xHis-tagged $RanBP2_{BBD}$. Before the pull-down experiments I prepared the lysate by removing bulk tubulin by adding GTP and taxol before

centrifugation.[152] In parallel to brain lysate centrifugation I was setting up the BicD2:RanBP2$_{BBD}$ reaction with CDK1 on ice. After centrifugation of the lysate I added 7 mM CHAPS as I found it crucial in extracting the DDBR2 complex from the brain lysate. I then added the BicD2:RanBP2$_{BBD}$ reaction into the lysate and left on a roller overnight at 4°C. To efficiently pull-down the DDB or DDBR2 complexes I observed that longer lysate:bait incubation times gave better results. This is probably due to the generally low endogenous protein abundance in a relatively large solution volume. A single pull-down experiment was performed on five adult rat brains lysate (less than 25mL total volume). The bait proteins were added to the lysate at a final concentration of ~0.005-0.01μM. After the complex was purified on StrepII-tagged BicD2 the elution was concentrated and loaded onto Superose® 6 3.2/300 column. The complex has an expected size of ~3 MDa hence it elutes in the void volume of the column (~0.8 mL). The void volume was loaded on a gradient SDS-PAGE to check for characteristic bands (Figure 23). Indeed there were several dynein and dynactin specific bands that I was able to confirm with MS which would indicate that the pull-down of the endogenous proteins worked with recombinant BicD2.

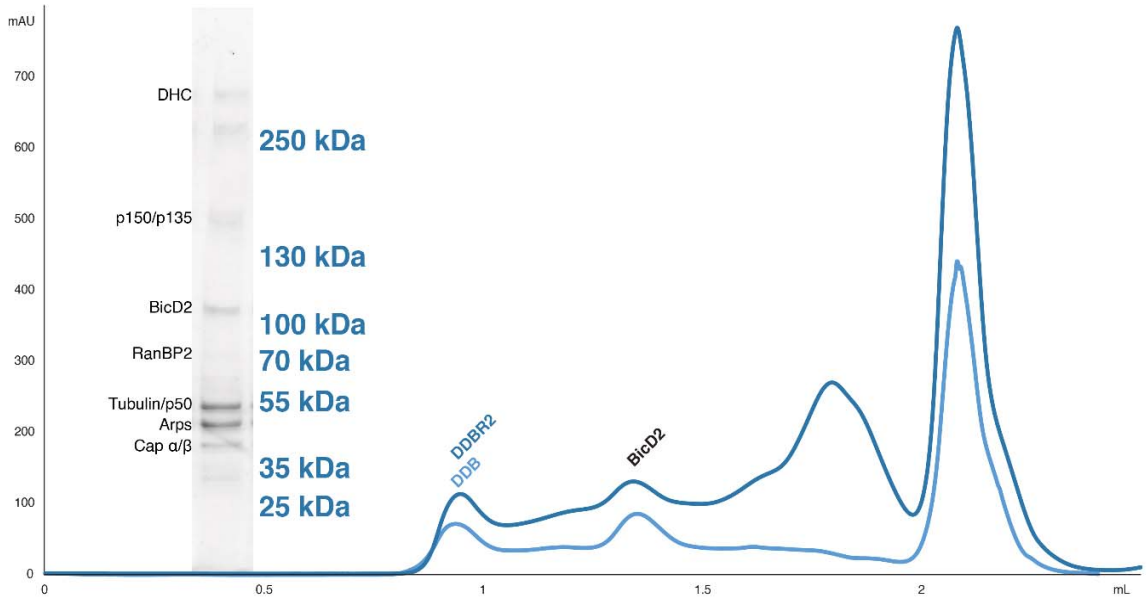

Figure 23. Reconstitution of the DDB and DDBR2 complexes from rat brain lysates. The light blue SEC profile shows the lysate incubated with the full-length BicD2 only. The dark blue SEC profile shows the lysate incubated with BicD2 and pre-phosphorylated $RanBP2_{BBD}$. Gradient SDS-PAGE gel for the void volume of the DDBR2 SEC profile.

3.3 Discussion

Cargo adaptors are long, coiled-coil proteins that are crucial in motor protein-mediated intracellular transport. Their versatility in binding partner proteins is outstanding. They can bind minus end directed motor dynein, plus end motor kinesin, and multiple cargos. The bases of dynein recruitment by some cargo adaptors have been described to a molecular level[150,133,189] shedding light on how N-terminal domain of the cargo adaptor can interact with dynein's light intermediate chain via CC1 box motif. Similarly the Spindly domain interaction with dynactin had been characterised.

In contrast the other terminus of the cargo adaptor, responsible for the cargo recruitment, is lacking molecular-level description of its interactions. For human BicD2 there are at least three cargos reported: RanBP2[26], Rab6A[165], and Nesprin[247]. There are also reports demonstrating interaction between BicD2 and viral capsids[248]. The interaction of motor proteins with viruses is well known but there was no studies correlating these interactions with specific cargo adaptors (other than HIV-1). The likely reason for such poor descriptions of these interactions are difficulties in producing and handling the cargo adaptors as well as their cargos. Also, many of these proteins are flexible and/or disordered which makes structural studies very challenging. Nevertheless structural information is needed in order to understand these mechanisms.

In order to attempt biophysical and structural studies of BicD2 I have first established an efficient protocol for producing sufficient amount of a human full-length BicD2. The main challenge in producing BicD2 was its solubility. I attempted multiple approaches to overcome its hydrophobic character by fusion with either superfolding GFP, lipoyl group, MBP, or trigger factor. I have also screened expression conditions to find out if that can keep the protein in the solution, but without a significant outcomes. The last approach I had attempted was addition of the detergent to the solution at the lysis step. Addition of a zwitterionic detergent extracted over 80% of the protein from the pellet into a soluble form. That finding allowed me to characterize full-length protein but also perform functional studies with its interactor RanBP2.

Next, I performed basic biophysical characterization of the BicD2. Upon screening BicD2 against multiple additives (salts, detergents, small molecules, buffers) it turned out that pH has a striking effect on BicD2. Variation of pH between 6

and 8 gave unique melting curves of the protein which indicated that it might undergo different conformational transitions. I further described this pH sensitivity with SEC, cryoEM, CD, negative stain to conclude that protein exists in multiple conformational states. At slightly acidic pH the protein is in partially unfolded state. It is a very interesting behaviour as protein at that pH value should still carry a negative charge (pI of BicD2 equals 5.3). At neutral values BicD2 adopts its well described autoinhibited conformation and slightly basic values release BicD2 from that state entering what we call an open conformation where CC domains do not interact with each other.

With help of MSA and structure predictions with AlphaFold2 I also identified residues in the BicD2 sequence that are crucial for maintaining its stability (Y538, H640). I confirmed stabilizing role of these residues by analysing respective point mutations with SEC, showing that folded dimeric fraction of the protein is significantly reduced upon introduction of those point mutations.

Last but not least I reconstituted a complex between known BicD2 cargo RanBP2. I was able to form a complex upon CDK1 modification of the RanBP2 fragment (but not BicD2). I also analysed to complex formation efficiency in respect to the BicD2's pH-induced conformational changes and the complex between RanBP2 and BicD2 appeared to be more homogenous at pH8.0 and lower pH values caused uniform distribution of these proteins in the SEC profiles suggesting that they do reach a steady state. I also confirmed BicD2 binding properties by incubation with rat brain lysates to demonstrate its ability to recruit dynein and dynactin. I was able to pull down motor protein dynein-1 complex with BicD2 as a bait protein, hence the DDB complex. Similarly the same complex with cargo was reconstituted using RanBP2 as a bait (DDBR2).

My work on BicD2 cargo adaptor has provided an efficient protocol for production of soluble and fully functional cargo adaptor paving the way in DDB complexes regulation studies. It is also a first attempt at visualising the cargo adaptor with cryoEM proving its conformational dynamics. I also described biochemical activity of the full-length adaptor by establishing a methodology to reconstitute large DDBR2 complex extracted from mammalian brain tissue.

METHODS

4. Methods

4.1 Molecular biology

4.1.1 PCR reactions

PCR reactions were normally prepared in a 25 μL volume. Depending on the GC content I used 5 μL of either 5x Phusion HF or GC buffer (New England Biolabs), 0.2 mM of the dNTP mix, 0.15 μL of forward and reverse primers (100 pmol/μL), ~0.5 μL of the template DNA (~100 ng/μL), and 0.25 μL of Phusion® High-Fidelity DNA Polymerase (New England Biolabs). The remaining volume was filled up with mQ H_2O.

4.1.2 Gibson assembly

The Gibson assembly master mix was prepared according to the standard protocol.[249] In short, 320 μL of freshly thawed 5x ISO buffer was mixed with 0.64 μL 10 U/μL T5 exonuclease, 20 μL of 2 U/μL Phusion® High-Fidelity DNA Polymerase, 160 μL of 40 U/μL Taq DNA ligase, and filled up with mQ water up to 1.2 mL and stored at -20 °C in 15 μL aliquots. For the assembly reaction, the Gibson assembly aliquot was thawed on ice and mixed with DNA (linearized vector and insert at equimolar ratio) in a total volume of 20 μL. The reaction mixture was then incubated at 50°C in either water bath or thermocycler for 1 hour. Then the reaction mixture was incubated for 2 minutes on ice and used for transformation into the TOP10 E. coli strain.

4.1.3 Transformation for DNA preparation

The Gibson assembly reaction or plasmids were transformed into chemically competent TOP10 cells by mixing the DNA with 100 μL of cells (or 100 ng of DNA). The cells were then incubated on ice for 30 minutes, heat shocked at 42°C for 45 seconds and then mixed with 400 μL of LB medium and recovered at 37°C in a shaking incubator for 1 hour. After recovery 100 μL of the cells were plated out on a selective plate and incubated overnight at 37°C.

4.1.4 Bacmid preparation

The target plasmid was transformed into the DH10MB E. coli strain similarly to the TOP10 transformation protocol. After the heat shock the cell suspension was mixed with 2 mL of LB and recovered at 37°C for 5-6 hours. Then 100 μL of the cells were plated out on a selective plate containing 50 μg/mL kanamycin, 10 μg/mL tetracycline, 7 μg/mL gentamicin, 0.4 mM IPTG, and 500 μg/mL X-gal. Plates were then incubated at 37°C overnight, followed by incubation at room temperature for the next 24-48 hours until the blue color developed well. Once the white colonies were identifiable they were re-streaked on to a fresh selective plate to further confirm the recombination (with a blue one as a negative control). A few white colonies were then inoculated in 6 mL of LB media for bacmid production and incubated overnight at 37 °C in a shaker. The cells were then spun down at 12000 rpm at 4°C for 10 minutes. The supernatant was discarded and the pellet re-suspended in 250 μL of A1 buffer (Macherey-Nagel). Then 250 μL of P2 buffer (0.2M NaOH, 1% SDS) was added and mixed gently. After 5 minutes 300 μL of the P3 buffer (3M KOAc, pH5.5) was added and mixed gently. Then the tubes were spun at 12000 rpm at 4°C for 10 minutes, the supernatant was collected into a new tube, and the procedure repeated three times (to ensure there is no leftover pellet in the tube). The tubes were then left to reach RT and then 800 μL of isopropanol was added, gently mixed, and incubated for 10 minutes on ice. Bacmid DNA was precipitated by spinning down (12000 rpm, 15 min, RT) and after supernatant removal the pellet was washed with 500 μL ice-cold 70% ethanol and spun down again at RT for 5 minutes and 12000 rpm. The supernatant was removed and the tubes were left to dry off in a sterile place. Bacmid DNA was then immediately taken for transfection.

4.1.5 Transfection

Prior to transfection, the Sf9 cells were split to 1×10^6 cells/mL a day before. I then prepared a transfection 'master mix' by mixing 250 μL of media (Sf-900 II SFM, Gibco), 5 μL of the transfection reagent (FuGENE HD, Promega), and 10-50 μL of the bacmid DNA. The reaction was then left under the laminar flow hood for 30 minutes. Then Sf9 cells were spun down at 2000 rpm for 5 minutes and resuspended in fresh media to a final cell count of 1×10^6 cells/mL. The cells were then split into a 6-well plate well in 2 mL portions, mixed with the transfection mixture, and incubated at 27°C.

Every DH10MB strain used in this work contained one fluorescent protein to visually assess the presence of the virus (either CFP, YFP, or mCherry). Once the P0 virus was visible under the light microscope a shaking Sf9 culture was prepared for further virus amplification (P1) and subsequent protein production (infections with P2 or higher).

4.2 Protein production

4.2.1 Bacterial expression and purification

Plasmids for bacterial expression were transformed into E. coli BL21(DE3) chemically competent cells and grown overnight on selective plates. The plate was used for inoculation of the 50 mL pre-culture and grown overnight at 37°C in LB medium for further scale-up. Protein expression was induced at ~25°C with 1mM isopropyl-1-thio-β-D-galactopyranoside (IPTG) and expressed for 3 h at 37°C. Cells were harvested, washed with 1xPBS and frozen for purification. In my work I used many proteins expressed in bacteria which is why I will describe the general protocol used. Pellets were re suspended in the lysis buffer (containing 20 mM Tris pH 8.0, 100 mM NaCl, 10% glycerol, 1 mM DTT, 2 mM PMSF, protease inhibitors) and incubated on a roller for 1-2h at 4°C. Cells were lysed by sonication (5x30s with 30s breaks on ice) and centrifuged at 30000 rpm at 4°C for 1 hour. The supernatant was mixed with pre-equilibrated respective resin (depending on the tag) for 30 minutes at 4°C and loaded on to a gravity flow column. The resin was then washed with 10 CV of the lysis buffer, 10 CV of the wash buffer (20 mM Tris pH8.0, 10% glycerol, 2 mM DTT), and eluted with the elution buffer (composition depending on the construct). The pooled fractions were concentrated to the highest concentration possible and snap-frozen in 100μL aliquots for further experiments and gel filtration. General deviations from this protocol include the use of 7 mM CHAPS for all BicD2 preparations and replacement of the Tris buffer with PBS. RanBP2$_{BBD}$ was normally purified under non-native conditions hence the lysis and wash buffer contained 6M urea and incubation steps were done at RT.

4.2.2 CDK1-CyclinB complex insect cell expression and purification

Insect-cell expression plasmids were transformed into E. coli DH10MB-MCherry chemically competent cells. The P2 virus was used for large scale infection of the Sf9 cultures. The Sf9 cells were split to 1×10^6 cells/mL and expressed for 72 hours or to 2×10^6 cells/mL and expressed for 48 hours. The cells were then collected at 1000 rpm for 10 min at 4°C. The pellet was flash-frozen in liquid nitrogen and stored at -80°C until purification. The $CDK1^{CyclinB}$ complex pellet was re suspended in the lysis buffer containing 50 mM Tris-HCl pH8.0, 10 mM $MgCl_2$, 10% glycerol, 0.1% NP40, 0.1 mM EDTA, 2 mM DTT, 2 mM PMSF, protease inhibitors, and incubated on a roller for 1h at 4°C. Cells were lysed by sonication (2x30s with 30s breaks on ice) and centrifuged at 40000 rpm at 4°C for 1 hour. The supernatant was then mixed with pre-equilibrated GST-sepharose beads for 30 minutes at RT and loaded on to a gravity flow column. The resin was washed with 10 CV of the lysis buffer, 10 CV of the wash buffer (20 mM Tris-HCl pH8.0, 150mM NaCl, 10% glycerol, 0.1mM EDTA), and eluted with the elution buffer (20 mM Tris-HCl pH8.0, 150 mM NaCl, 10% glycerol, 0.1 mM EDTA, 25 mM reduced GST). Pooled fractions were concentrated to 0.5 mg/mL and snap-frozen in 50 μL aliquots for further experiments. The RanBP2 and BicD2 constructs expressed in Sf9 were purified similarly.

4.2.3 Dynein-2 insect cell expression and purification

All dynein-2 constructs were purified similarly to the method described previously.[15] In short, the virus encoding WT dynein-2 or a deletion mutant was used to infect the Sf9 cells at 1×10^6 cells/mL count for 72 hours. The frozen pellets were re suspended in lysis buffer (30 mM HEPES pH 7.4, 50 mM KOAc, 2 mM MgOAc, 0.2 mM EGTA, 10% v/v glycerol, 300 mM KCl, 0.2 mM Mg.ATP, 1 mM DTT and 2 mM PMSF) and lysed in a dounce tissue homogenizer or sonicated on ice (~30 seconds). The lysate was then cleared by centrifugation at 45000 rpm for 1 h at 4 °C. The supernatant was incubated for 3 h with IgG beads with around 2-3 mL beads per 1 L of the Sf9 culture. The beads were then loaded on to a gravity-flow column and washed with 10 CV of the lysis buffer and 10 CV of TEV buffer (50 mM Tris-HCl pH 8, 150 mM KOAc, 2 mM MgOAc, 1 mM EGTA, 10% v/v glycerol, 1 mM DTT and 0.2 mM Mg.ATP). Beads were then re-suspended in the TEV buffer (~1:2 beads to buffer ratio) and incubated overnight with TEV protease on a roller in the cold room. The next day, the

protein was eluted, concentrated to 4 mg/mL, snap-frozen in 50 μL aliquots, and stored at -80 °C. The stocks were thawed on ice and run on a Superose® 6 SEC column prior to use. For all dynein-2 constructs expression levels are normally within the milligrams range for 1 L of the Sf9 culture.

4.2.4 Dynein-1 complex insect cell expression and purification

The dynein-1 complex was expressed and purified as described.[33] The virus encoding dynein-1 complex was used to infect the Sf9 cells at 1×10^6 cells/mL count for 72 hours. The frozen pellets were re suspended in lysis buffer (50 mM HEPES pH 7.4, 100 mM NaCl, 1 mM DTT, 0.1 mM ATP, 10% glycerol, 2 mM PMSF) and lysed in a dounce tissue homogenizer (~30 strokes). The lysate was then cleared by centrifugation at 45000 rpm for 1 h at 4 °C. All further steps were identical as for the dynein-2 purification.

4.2.5 Inclusion bodies purification

The cells were lysed in a lysis buffer followed by four washing steps (wash buffer: 100mM Tris pH 8.0, 2M urea, 0.5M NaCl, 5mM EDTA, 2% Triton, 1mM β-mercaptoethanol). For each wash step the 1L culture pellet was re suspended in ~50mL of the wash buffer, incubated on a roller for 45 minutes at RT, and centrifuged at 20000g at 4°C. The inclusion bodies were then re suspended in the denaturation buffer (100mM Tris pH8.0, 6M guanidine-HCl, 20mM β-mercaptoethanol) and incubated for 1h at 70°C. The denatured protein was then filtered and incubated at RT with Ni-NTI agarose beads (at that time I worked with 6xHis tagged BicD2) and eluted under denaturing conditions (denaturation buffer with 400mM imidazole was used for elution). The eluted protein was then dialysed against a wash buffer at ~4°C overnight in a dialysis tube with a 10kDa cutoff membrane (SnakeSkinTM).

4.3 Structural studies

4.3.1 CryoEM sample preparation

For the BicD2 cryoEM analysis 100μL of the sample was thawed on ice and equilibrated with 5xPBS at either pH8.0 or 7.0. The Superose6® increase SEC column was equilibrated for 16h at a specific pH (in PBS buffer only) and the dimer fraction taken for grid preparation. Cu/Rh 1.2/1.3 300mesh grids were plasma cleaned for 90 seconds at 30% plasma power (under 80:20 argon:oxygen). The protein concentration was adjusted to 1 μM and then applied on the grid and plunge-frozen in a Vitrobot Mark IV robot (ThermoFisher), maintained at 100% humidity and 10°C.

All dynein-2 constructs were purified on a Superose6® column prior to cryoEM grid preparation. The peak fraction was adjusted to 1-2 μM and then mixed with the ATP hydrolysis transition state analogue ADP.vanadate (ADP.Vi). To achieve that the 100 mM stock of sodium orthovanadate (New England Biolabs) was heated at 95 °C for 5 minutes, cooled down on ice and added to the protein sample to a final concentration of 3 mM followed by the addition of Mg.ATP to a final concentration of 3 mM. The protein was then used for grid preparation. For the majority of grid preparations, I used Cu/Rh 1.2/1.3 300mesh grids, cleaned with a plasma cleaner at 30% plasma power under a 80:20 argon:oxygen mixture for 90 seconds. 3 uL of the sample were applied on to the grid and plunge-frozen in a Vitrobot Mark IV robot (ThermoFisher) maintained at 100% humidity and 10 °C. For most of the dynein grids the blotting force was set to 0, and blotting time was in the range between 2 to 6 seconds. These parameters were giving uniform ice-thickness and good particle distribution. I did not observe a significant difference in particle distribution on the grid when I used 1 μM or 2 μM of the sample at grid preparation stage. The grids were then stored in LN_2 until the screening session. In the beginning, I was screening the grids on an in-house Polara microscope which was later replaced by a Glacios™ Cryo-TEM microscope (ThermoFisher). The grids with good parameters were saved for high-resolution data collection on a Titan Krios Cryo-TEM 300keV microscope.

4.3.2 CryoEM data collection and image analysis

Datasets for BicD2 at pH8.0 and pH7.0 were collected using the Glacios™ Cryo-TEM operating at 200keV with a K2 Summit® direct electron detector (Gatan). Videos were collected in counting mode, with a final calibrated pixel size of 1.078 Å/pixel, 8s exposure, and total dose of ~ 54 $e^-/Å^2$. SerialEM was used for automated data collection and videos were processed using Relion3.0.[250] Micrographs were filtered manually giving each dataset ~700 micrographs. Particles were picked using the general model in TOPAZ and 2D classified twice. Each dataset yielded around 150k particles used for 2D classification. All data processing steps were done reference-free.

4.3.3 Negative staining

All protein constructs were screened for the right concentration using negative stain analysis. Most of the proteins (whether dynein-1, dynein-2, BicD2, or $RanBP2_{BBD}$) were in range from 10 to 30 nM to obtain a good particle distribution. The grids were plasma cleaned as for the cryoEM analysis. Around 10-20 μL of the protein was loaded onto the grid, incubated for 20-30 seconds and blotted away manually. Then 20 μL of the uranyl acetate solution (2%) was applied onto the grid, gently pipetted up and down and left on the grid for ~30 seconds. This step was repeated 3 times to ensure a good sample embedding in the stain. Before staining the uranyl acetate solution was spun down at 17000g for 2 minutes (to remove the aggregates).

4.3.4 AlphFold2 structure prediction

The CC2 and CC3 domain of a human isoform 2 of BicD2 (residues 265-855) was used for homooligomer modelling using the AlphaFold2 advanced package (Google Colab). We generated 5 models and used MMseqs2 (UniRef+Environmental) for the MSA generation. MMseqs2 covered between 650-800 residues in the N-terminal part of the fragment used, except for the C-terminal coil sequence (unique to human BicD2 isoform2).

4.4 Other biophysical and biochemical methods

4.4.1 In vitro kinase assays and phosphorylation mapping

$CDK1^{CyclinB}$ was mixed with the target protein at a 1:100 molar ratio with 0.1mM Mg.ATP and incubated for 30min at RT. Each sample had a negative control that did not contain Mg.ATP. Each reaction mixture was loaded onto SDS-PAGE and stained with pro-Q diamond stain to check for phosphorylated proteins. Phosphorylation sites were analysed with trypsin digest MS using Orbitrap Elite and an Acclaim Pepmap 100 column. The PSMs values corresponded to the number of MS2 spectra which made it possible to identify peptides. In BicD2 75% of the sequence was covered (PSM's: 2087) while for RanBP2 85% of the sequence was covered (PSM's: 1195).

4.4.2 Unnatural amino acid-incorporation

Target serine codons were point mutated into TAG stop codons. The plasmids were then transformed into SepRS(2)/pSer tRNA(B4)CUA/EF-Sep bacterial strain. The strain was a kind gift from the Jason Chin lab at LMB. The transformation was grown overnight on selective LB plates (tetracycline/chloramphenicol). The colonies were used to inoculate a shaking culture for further upscaling. Bacterial cultures were started at OD_{600}=0.1. At OD_{600}=0.35-0.4, 2 mM phosphoserine was added to the cultures and further incubated to reach OD_{600}=0.5. Prior to induction with 1 mM IPTG another 2 mM of phosphoserine was added. Proteins were expressed for 4 hours at 37°C and pellets were frozen until needed.

4.4.3 SEC-MALS

Prior to SEC-MALS analysis BicD2 dimer was purified on Superose® 6 Increase 3.2/300 column in SEC buffer (50 mM Tris pH 7.5, 150 mM Potassium acetate, 10 mM Magnesium acetate, 7 mM CHAPS). Then 90μL of BicD2 sample (1mg/mL) was injected into FPLC Ettan Micro LC (formerly GE Healthcare, now Cytiva) coupled with MiniDAWN TREOS MALS detector (Wyatt Technology), Optilab T-rEX (Wyatt Technology) RI detector, and Superdex® S200 10/300 GL (formerly GE Healthcare, now Cytiva) column and run at 25°C in SEC buffer (50 mM Tris pH 7.5, 150 mM Potassium acetate, 10 mM Magnesium acetate). The data was processed using the ASTRA software (Wyatt Technology).

4.4.4 Circular dichroism

CD experiments were recorded on a Jasco J-815 spectropolarimeter (Easton, MD) equipped with an automatic 6-position Peltier thermostated cell holder. The instrument was calibrated with 10-camphorsulphonic acid. Samples (65 µL) were prepared in PBS supplemented with CHAPS 7 mM and buffered at various pH (6.0, 7.0 or 8.0). Far-UV CD data were collected in the 182–270 nm range using a 0.1 mm pathlength cell (Quartz-Suprasil, Hellma UK Ltd) at 20.0 °C ± 0.1 °C. Spectra were acquired using a continuous scan rate of 50 nm/min and are presented as an average of 10 successive scans. The response time and the bandwidth were 1.0 s and 1 nm, respectively. The spectra were corrected by subtracting the solvent spectrum obtained under identical conditions.

4.4.5 Rat brain lysate preparation

Freshly sacrificed rats were taken for brain extraction. The organs were gently washed in PMEE buffer (35mM PIPES pH7.2, 5mM MgSO4, 1mM EGTA, 6.8% glycerol, 1mM TCEP, protease inhibitors) and snap frozen until needed. Upon thawing on ice the brains were mixed with protease inhibitors and a minimal amount of the PMEE buffer. Then the brains were homogenized for a few seconds with a tissue homogenizer (on a minimal setting to avoid foaming) followed by 30 strokes in a dounce homogenizer on ice. Lysed brains were then centrifuged at 40000 rpm for 1 h at 4°C. The cleared lysate was instantly used for further experiments without further freezing.

References

1. Rao, Q. et al. Structures of outer-arm dynein array on microtubule doublet reveal a motor coordination mechanism. Nat. Struct. Mol. Biol. 2021 2810 **28**, 799–810 (2021).
2. Walton, T., Wu, H. & Brown, A. Structure of a microtubule-bound axonemal dynein. Nat. Commun. **12**, (2021).
3. Kubo, S. et al. Remodeling and activation mechanisms of outer arm dyneins revealed by cryo-EM. EMBO Rep. **22**, (2021).
4. Toropova, K. et al. Structure of the dynein-2 complex and its assembly with intraflagellar transport trains. Nat. Struct. Mol. Biol. 2019 269 **26**, 823–829 (2019).
5. Jordan, M. A. & Pigino, G. In situ cryo-electron tomography and subtomogram averaging of intraflagellar transport trains. Methods Cell Biol. **152**, 179–195 (2019).
6. L, U. et al. Cryo-EM shows how dynactin recruits two dyneins for faster movement. Nature **554**, 202–206 (2018).
7. Foster, H. E., Santos, C. V. & Carter□, A. P. A cryo-ET survey of microtubules and intracellular compartments in mammalian axons. (2021). doi:10.1083/jcb.202103154
8. SA, B., ML, W., H, S., PJ, K. & K, O. Dynein structure and power stroke. Nature **421**, 715–718 (2003).
9. AP, C., C, C., L, J. & RD, V. Crystal structure of the dynein motor domain. Science **331**, 1159–1165 (2011).
10. T, K. et al. The 2.8 Å crystal structure of the dynein motor domain. Nature **484**, 345–350 (2012).
11. T, K., K, S. & G, K. X-ray structure of a functional full-length dynein motor domain. Nat. Struct. Mol. Biol. **18**, 638–642 (2011).
12. AJ, R. et al. AAA+ Ring and linker swing mechanism in the dynein motor. Cell **136**, 485–495 (2009).
13. Schmidt, H., Gleave, E. S. & Carter, A. P. Insights into dynein motor domain function from a 3.3-Å crystal structure. Nat. Struct. Mol. Biol. **19**, 492–7, S1 (2012).
14. Schmidt, H., Zalyte, R., Urnavicius, L. & Carter, A. P. Structure of human cytoplasmic dynein-2 primed for its power stroke. Nature **518**, 435–438 (2015).
15. H, S., ES, G. & AP, C. Insights into dynein motor domain function from a 3.3-Å crystal structure. Nat. Struct. Mol. Biol. **19**, 492–497 (2012).
16. Bhabha, G. et al. Allosteric communication in the dynein motor domain. Cell **159**, 857–868 (2014).
17. T, K. et al. The 2.8 Å crystal structure of the dynein motor domain. Nature **484**, 345–350 (2012).
18. LM, I., DD, L., EV, K. & L, A. Evolutionary history and higher order classification of AAA+ ATPases. J. Struct. Biol. **146**, 11–31 (2004).
19. Schmidt, H. Dynein motors: How AAA+ ring opening and closing coordinates microtubule binding and linker movement. BioEssays **37**, 532–543 (2015).
20. Dewitt, M. A., Cypranowska, C. A., Cleary, F. B., Belyy, V. & Yildiz, A. THE AAA3 DOMAIN OF CYTOPLASMIC DYNEIN ACTS AS A SWITCH TO FACILITATE MICROTUBULE RELEASE. Nat. Struct. Mol. Biol. **22**, 73 (2015).

21. Bielas, S., Higginbotham, H., Koizumi, H., Tanaka, T. & Gleeson, J. G. Cortical neuronal migration mutants suggest separate but intersecting pathways. Annu. Rev. Cell Dev. Biol. **20**, 593–618 (2004).
22. Spear, P. C. & Erickson, C. A. Interkinetic nuclear migration: a mysterious process in search of a function. Dev. Growth Differ. **54**, 306–316 (2012).
23. Tsai, J. W., Chen, Y., Kriegstein, A. R. & Vallee, R. B. LIS1 RNA interference blocks neural stem cell division, morphogenesis, and motility at multiple stages. J. Cell Biol. **170**, 935–945 (2005).
24. Tsai, J. W., Lian, W. N., Kemal, S., Kriegstein, A. R. & Vallee, R. B. Kinesin 3 and cytoplasmic dynein mediate interkinetic nuclear migration in neural stem cells. Nat. Neurosci. **13**, 1463–1472 (2010).
25. Hu, D. J. K. et al. Dynein recruitment to nuclear pores activates apical nuclear migration and mitotic entry in brain progenitor cells. Cell **154**, 1300 (2013).
26. Splinter, D. et al. Bicaudal D2, dynein, and kinesin-1 associate with nuclear pore complexes and regulate centrosome and nuclear positioning during mitotic entry. PLoS Biol. **8**, 1000350 (2010).
27. Baffet, A. D., Hu, D. J. & Vallee, R. B. Cdk1 Activates Pre-mitotic Nuclear Envelope Dynein Recruitment and Apical Nuclear Migration in Neural Stem Cells. Dev. Cell **33**, 703–716 (2015).
28. Bolhy, S. et al. A Nup133-dependent NPC-anchored network tethers centrosomes to the nuclear envelope in prophase. J. Cell Biol. **192**, 855–871 (2011).
29. McKenney, R. J., Vershinin, M., Kunwar, A., Vallee, R. B. & Gross, S. P. LIS1 and NudE induce a persistent dynein force-producing state. Cell **141**, 304–314 (2010).
30. Shu, T. et al. Ndel1 operates in a common pathway with LIS1 and cytoplasmic dynein to regulate cortical neuronal positioning. Neuron **44**, 263–277 (2004).
31. Toyo-Oka, K. et al. Recruitment of katanin p60 by phosphorylated NDEL1, an LIS1 interacting protein, is essential for mitotic cell division and neuronal migration. Hum. Mol. Genet. **14**, 3113–3128 (2005).
32. McKenney, R. J., Huynh, W., Tanenbaum, M. E., Bhabha, G. & Vale, R. D. Activation of cytoplasmic dynein motility by dynactin-cargo adapter complexes. Science (80-.). **345**, 337–341 (2014).
33. MA, S., HT, H., L, U., SL, B. & AP, C. In vitro reconstitution of a highly processive recombinant human dynein complex. EMBO J. **33**, 1855–1868 (2014).
34. Toropova, K., Mladenov, M. & Roberts, A. J. Intraflagellar transport dynein is autoinhibited by trapping of its mechanical and track-binding elements. Nat. Struct. Mol. Biol. 2017 245 **24**, 461–468 (2017).
35. Zhang, K. et al. Cryo-EM Reveals How Human Cytoplasmic Dynein Is Auto-inhibited and Activated. Cell **169**, 1303-1314.e18 (2017).
36. Herrmann, H., Bär, H., Kreplak, L., Strelkov, S. V. & Aebi, U. Intermediate filaments: From cell architecture to nanomechanics. Nature Reviews Molecular Cell Biology **8**, 562–573 (2007).
37. Fletcher, D. A. & Mullins, R. D. Cell mechanics and the cytoskeleton. Nature **463**, 485–492 (2010).
38. Perrais, D. & Merrifield, C. J. Dynamics of endocytic vesicle creation. Developmental Cell **9**, 581–592 (2005).
39. Geli MI, R. H. E. internalization in yeast and animal cells: similar and different. J. C. S. 1998 A. (P. 8):1031-7. P. 9512499. No Title.

40. Wickstead, B. & Gull, K. The evolution of the cytoskeleton. Journal of Cell Biology **194**, 513–525 (2011).
41. Cooper, G. No Title. in The Cell: A Molecular Approach (Sunderland (MA): Sinauer Associates, 2000).
42. Weisenberg, R. C. Microtubule formation in vitro in solutions containing low calcium concentrations. Science (80-.). **177**, 1104–1105 (1972).
43. Desai, A. & Mitchison, T. J. Microtubule polymerization dynamics. Annual Review of Cell and Developmental Biology **13**, 83–117 (1997).
44. Nogales, E., Wolf, S. G. & Downing, K. H. Structure of the αβ tubulin dimer by electron crystallography. Nature **391**, 199–203 (1998).
45. Löwe, J., Li, H., Downing, K. H. & Nogales, E. Refined structure of αβ-tubulin at 3.5 Å resolution. J. Mol. Biol. **313**, 1045–1057 (2001).
46. Tuszynski, J. A. et al. The evolution of the structure of tubulin and its potential consequences for the role and function of microtubules in cells and embryos. Int. J. Dev. Biol. **50**, 341–358 (2006).
47. Walker, R. A. et al. Dynamic instability of individual microtubules analyzed by video light microscopy: rate constants and transition frequencies. J. Cell Biol. **107**, 1437–1448 (1988).
48. Nogales, E. Structural insights into microtubule function. Annual Review of Biophysics and Biomolecular Structure **30**, 397–420 (2001).
49. Burbank, K. S. & Mitchison, T. J. Microtubule dynamic instability. Current Biology **16**, (2006).
50. Kirschner, M. & Mitchison, T. Beyond self-assembly: From microtubules to morphogenesis. Cell **45**, 329–342 (1986).
51. Inoué, S. & Salmon, E. D. Force generation by microtubule assembly/disassembly in mitosis and related movements. Molecular Biology of the Cell **6**, 1619–1640 (1995).
52. Verhey, K. J. & Gaertig, J. The tubulin code. Cell Cycle **6**, 2152–2160 (2007).
53. Hammond, J. W., Cai, D. & Verhey, K. J. Tubulin modifications and their cellular functions. Current Opinion in Cell Biology **20**, 71–76 (2008).
54. Fukushima, N., Furuta, D., Hidaka, Y., Moriyama, R. & Tsujiuchi, T. Post-translational modifications of tubulin in the nervous system. J. Neurochem. **109**, 683–693 (2009).
55. Hoffmann, P. C. et al. Electron cryo-tomography reveals the subcellular architecture of growing axons in human brain organoids. Elife **10**, (2021).
56. Ishikawa, T. Cryo-electron tomography of motile cilia and flagella. Cilia **4**, (2015).
57. Kiesel, P. et al. The molecular structure of mammalian primary cilia revealed by cryo-electron tomography. Nat. Struct. Mol. Biol. 2020 2712 **27**, 1115–1124 (2020).
58. C, I., V, B.-K., M, S. & G, P. Protein particles in Chlamydomonas flagella undergo a transport cycle consisting of four phases. J. Cell Biol. **153**, 13–24 (2001).
59. Chien, A. et al. Dynamics of the IFT machinery at the ciliary tip. Elife **6**, (2017).
60. Vale, R. D. The Molecular Motor Toolbox for Intracellular Transport. Cell **112**, 467–480 (2003).
61. G, P. & K, M. Transport of a novel complex in the cytoplasmic matrix of Chlamydomonas flagella. Proc. Natl. Acad. Sci. U. S. A. **94**, 4457–4462 (1997).
62. Oztas, E. Neuronal tracing. **2**, 2–5 (2003).
63. Cytoplasmic dynein conversion at a crush injury in rat peripheral axons - Li - 2000 - Journal of Neuroscience Research - Wiley Online Library. Available at:

https://onlinelibrary.wiley.com/doi/10.1002/1097-4547(20000715)61:2%3C151::AID-JNR6%3E3.0.CO;2-N. (Accessed: 19th October 2021)
64. SJ, S., WO, H. & KK, P. Distinct cytoplasmic dynein complexes are transported by different mechanisms in axons. Biochim. Biophys. Acta **1496**, 76–88 (2000).
65. Belyy, V. et al. The mammalian dynein–dynactin complex is a strong opponent to kinesin in a tug-of-war competition. Nat. Cell Biol. 2016 189 **18**, 1018–1024 (2016).
66. RS, S. Studies on the mechanism of the reversal of rapid organelle transport in myelinated axons of Xenopus laevis. Cell Motil. Cytoskeleton **10**, 296–308 (1988).
67. Ma, M. et al. Structure of the Decorated Ciliary Doublet Microtubule. Cell **179**, 909-922.e12 (2019).
68. ST, B., KK, P. & GS, B. A monoclonal antibody against kinesin inhibits both anterograde and retrograde fast axonal transport in squid axoplasm. Proc. Natl. Acad. Sci. U. S. A. **87**, 1061–1065 (1990).
69. SW, D. et al. Dynactin is required for bidirectional organelle transport. J. Cell Biol. **160**, 297–301 (2003).
70. SP, G., MA, W., SM, B. & EF, W. Coordination of opposite-polarity microtubule motors. J. Cell Biol. **156**, 715–724 (2002).
71. M, M. et al. Cytoplasmic dynein, the dynactin complex, and kinesin are interdependent and essential for fast axonal transport. Mol. Biol. Cell **10**, 3717–3728 (1999).
72. Reck-Peterson, S. L., Redwine, W. B., Vale, R. D. & Carter, A. P. The cytoplasmic dynein transport machinery and its many cargoes. Nat. Rev. Mol. Cell Biol. (2018). doi:10.1038/s41580-018-0004-3
73. IR, G. & AJ, R. Dynein: A Protein with Adenosine Triphosphatase Activity from Cilia. Science **149**, 424–426 (1965).
74. BM, P., HS, S. & RB, V. MAP 1C is a microtubule-activated ATPase which translocates microtubules in vitro and has dynein-like properties. J. Cell Biol. **105**, 1273–1282 (1987).
75. GJ, P., BL, D. & GB, W. The DHC1b (DHC2) isoform of cytoplasmic dynein is required for flagellar assembly. J. Cell Biol. **144**, 473–481 (1999).
76. ME, P., R, B., JA, K., P, B. & W, D. Cytoplasmic dynein heavy chain 1b is required for flagellar assembly in Chlamydomonas. Mol. Biol. Cell **10**, 693–712 (1999).
77. J, G. et al. Cytoplasmic dynein function is essential in Drosophila melanogaster. Genetics **142**, 865–878 (1996).
78. A, H. et al. Golgi vesiculation and lysosome dispersion in cells lacking cytoplasmic dynein. J. Cell Biol. **141**, 51–59 (1998).
79. Harms, M. B. et al. Mutations in the tail domain of DYNC1H1 cause dominant spinal muscular atrophy. Neurology **78**, 1714–1720 (2012).
80. Tsurusaki, Y. et al. A DYNC1H1 mutation causes a dominant spinal muscular atrophy with lower extremity predominance. Neurogenetics **13**, 327–332 (2012).
81. Scoto, M. et al. Novel mutations expand the clinical spectrum of DYNC1H1-associated spinal muscular atrophy. Neurology **84**, 668–679 (2015).
82. K, P. et al. Novel mutations in the DYNC1H1 tail domain refine the genetic and clinical spectrum of dyneinopathies. Hum. Mutat. **36**, 287–291 (2015).
83. Strickland, A. V. et al. Mutation screen reveals novel variants and expands the

phenotypes associated with DYNC1H1. J. Neurol. **262**, 2124–2134 (2015).
84. Weedon, M. N. et al. Exome sequencing identifies a DYNC1H1 mutation in a large pedigree with dominant axonal Charcot-Marie-Tooth disease. Am. J. Hum. Genet. **89**, 308–312 (2011).
85. Fiorillo, C. et al. Novel dynein DYNC1H1 neck and motor domain mutations link distal spinal muscular atrophy and abnormal cortical development. Hum. Mutat. **35**, 298–302 (2014).
86. J, L., M, K., J, J. & CC, H. Mutations in cytoplasmic dynein and its regulators cause malformations of cortical development and neurodegenerative diseases. Biochem. Soc. Trans. **41**, 1605–1612 (2013).
87. Paschal, B. M. & Vallee, R. B. Retrograde transport by the microtubule-associated protein MAP 1C. Nature **330**, 181–183 (1987).
88. Wilson, M. H. & Holzbaur, E. L. F. Opposing microtubule motors drive robust nuclear dynamics in developing muscle cells. J. Cell Sci. **125**, 4158–4169 (2012).
89. Fu, M. meng & Holzbaur, E. L. F. Integrated regulation of motor-driven organelle transport by scaffolding proteins. Trends in Cell Biology **24**, 564–574 (2014).
90. Schiavo, G., Greensmith, L., Hafezparast, M. & Fisher, E. M. C. Cytoplasmic dynein heavy chain: The servant of many masters. Trends in Neurosciences **36**, 641–651 (2013).
91. SR, G. et al. Dynactin, a conserved, ubiquitously expressed component of an activator of vesicle motility mediated by cytoplasmic dynein. J. Cell Biol. **115**, 1639–1650 (1991).
92. TA, S. & MP, S. Two activators of microtubule-based vesicle transport. J. Cell Biol. **115**, 1309–1318 (1991).
93. J, M. & EF, W. Dominant maternal-effect mutations of Drosophila melanogaster causing the production of double-abdomen embryos. Genetics **112**, 803–822 (1986).
94. Schlager, M. A., Hoang, H. T., Urnavicius, L., Bullock, S. L. & Carter, A. P. In vitro reconstitution of a highly processive recombinant human dynein complex. EMBO J. **33**, 1855–68 (2014).
95. Yingling, J. et al. Neuroepithelial Stem Cell Proliferation Requires LIS1 for Precise Spindle Orientation and Symmetric Division. Cell **132**, 474–486 (2008).
96. Feng, Y. et al. LIS1 Regulates CNS Lamination by Interacting with mNudE, a Central Component of the Centrosome. Neuron **28**, 665–679 (2000).
97. Feng, Y. & Walsh, C. A. Mitotic spindle regulation by Nde1 controls cerebral cortical size. Neuron **44**, 279–293 (2004).
98. Cianfrocco, M. A., DeSantis, M. E., Leschziner, A. E. & Reck-Peterson, S. L. Mechanism and Regulation of Cytoplasmic Dynein. Annu. Rev. Cell Dev. Biol. **31**, 83 (2015).
99. Gibbons, B. H., Asai, D. J., Tang, W. J., Hays, T. S. & Gibbons, I. R. Phylogeny and expression of axonemal and cytoplasmic dynein genes in sea urchins. https://doi.org/10.1091/mbc.5.1.57 **5**, 57–70 (2017).
100. Tanaka, Y., Zhang, Z. & Hirokawa, N. Identification and molecular evolution of new dynein-like protein sequences in rat brain. J. Cell Sci. **108**, 1883–1893 (1995).
101. Pazour, G. J., Wilkerson, C. G. & Witman, G. B. A Dynein Light Chain Is Essential for the Retrograde Particle Movement of Intraflagellar Transport (IFT). J. Cell Biol. **141**, 979–992 (1998).
102. Porter, M. E., Bower, R., Knott, J. A., Byrd, P. & Dentler, W. Cytoplasmic Dynein

Heavy Chain 1b Is Required for Flagellar Assembly in Chlamydomonas. https://doi.org/10.1091/mbc.10.3.693 **10**, 693–712 (2017).
103. Signor, D. et al. Role of a Class Dhc1b Dynein in Retrograde Transport of Ift Motors and Ift Raft Particles along Cilia, but Not Dendrites, in Chemosensory Neurons of Living Caenorhabditis elegans. J. Cell Biol. **147**, 519–530 (1999).
104. Vuolo, L., Stevenson, N. L., Mukhopadhyay, A. G., Roberts, A. J. & Stephens, D. J. CELL SCIENCE AT A GLANCE Cytoplasmic dynein-2 at a glance. (2020). doi:10.1242/jcs.240614
105. Cao, M. et al. Uni-directional ciliary membrane protein trafficking by a cytoplasmic retrograde IFT motor and ciliary ectosome shedding. Elife **2015**, (2015).
106. Hao, L., Efimenko, E., Swoboda, P. & Scholey, J. M. The Retrograde IFT Machinery of C. elegans Cilia: Two IFT Dynein Complexes? PLoS One **6**, e20995 (2011).
107. Rosenbaum, J. L., Witman, G. B. & Cilia, N. INTRAFLAGELLAR TRANSPORT. Nat. Rev. l Mol. CELL Biol. **3**, 3 (2002).
108. Jordan, M. A., Diener, D. R., Stepanek, L. & Pigino, G. The cryo-EM structure of intraflagellar transport trains reveals how dynein is inactivated to ensure unidirectional anterograde movement in cilia. Nat. Cell Biol. 2018 2011 **20**, 1250–1255 (2018).
109. EV, K., YI, W. & L, A. Protein fold recognition using sequence profiles and its application in structural genomics. Adv. Protein Chem. **54**, 245–275 (2000).
110. Hanson, P. I. & Whiteheart, S. W. AAA+ proteins: have engine, will work. Nat. Rev. Mol. Cell Biol. 2005 67 **6**, 519–529 (2005).
111. Snider, J., Thibault, G. & Houry, W. A. The AAA+ superfamily of functionally diverse proteins. Genome Biol. 2008 94 **9**, 1–8 (2008).
112. DD, L., YI, W., EV, K. & L, A. Classification and evolution of P-loop GTPases and related ATPases. J. Mol. Biol. **317**, 41–72 (2002).
113. Samora, C. P. et al. MAP4 and CLASP1 operate as a safety mechanism to maintain a stable spindle position in mitosis. Nat. Cell Biol. **13**, 1040–1052 (2011).
114. T, K. & IM, C. Chromosome- and spindle-pole-derived signals generate an intrinsic code for spindle position and orientation. Nat. Cell Biol. **14**, 311–317 (2012).
115. Lin, S. X. & Collins, C. A. Immunolocalization of cytoplasmic dynein to lysosomes in cultured cells. J. Cell Sci. **101**, 125–137 (1992).
116. M, S., PR, S. & A, W. The P-loop--a common motif in ATP- and GTP-binding proteins. Trends Biochem. Sci. **15**, 430–434 (1990).
117. Walker, J. E., Saraste, M., Runswick, M. J. & Gay, N. J. Distantly related sequences in the alpha- and beta-subunits of ATP synthase, myosin, kinases and other ATP-requiring enzymes and a common nucleotide binding fold. EMBO J. **1**, 945 (1982).
118. Bugreev, D. V. & Mazin, A. V. Ca2+ activates human homologous recombination protein Rad51 by modulating its ATPase activity. Proc. Natl. Acad. Sci. **101**, 9988–9993 (2004).
119. Koonin, E. V. A common set of conserved motifs in a vast variety of putative nucleic acid-dependent ATPases including MCM proteins involved in the initiation of eukaryotic DNA replication. Nucleic Acids Res. **21**, 2541–2547 (1993).
120. DD, L., EV, K. & L, A. Evolution and classification of P-loop kinases and related

proteins. J. Mol. Biol. **333**, 781–815 (2003).
121. T, O. & AJ, W. AAA+ superfamily ATPases: common structure--diverse function. Genes Cells **6**, 575–597 (2001).
122. Neuwald, A. F., Aravind, L., Spouge, J. L. & Koonin, E. V. AAA+: A Class of Chaperone-Like ATPases Associated with the Assembly, Operation, and Disassembly of Protein Complexes. Genome Res. **9**, 27–43 (1999).
123. K, K., T, I., AJ, W., T, T. & T, O. Dissecting the role of a conserved motif (the second region of homology) in the AAA family of ATPases. Site-directed mutagenesis of the ATP-dependent protease FtsH. J. Biol. Chem. **274**, 26225–26232 (1999).
124. Mann, D. et al. Mechanism of the intrinsic arginine finger in heterotrimeric G proteins. Proc. Natl. Acad. Sci. **113**, E8041–E8050 (2016).
125. P, W., S, C., M, K. & S, K. Structure and function of the AAA+ nucleotide binding pocket. Biochim. Biophys. Acta **1823**, 2–14 (2012).
126. IR, G., BH, G., G, M. & DJ, A. Multiple nucleotide-binding sites in the sequence of dynein beta heavy chain. Nature **352**, 640–643 (1991).
127. T, K., M, N., R, O., YY, T. & K, S. Distinct functions of nucleotide-binding/hydrolysis sites in the four AAA modules of cytoplasmic dynein. Biochemistry **43**, 11266–11274 (2004).
128. AP, C. Crystal clear insights into how the dynein motor moves. J. Cell Sci. **126**, 705–713 (2013).
129. AJ, R., T, K., PJ, K., K, S. & SA, B. Functions and mechanics of dynein motor proteins. Nat. Rev. Mol. Cell Biol. **14**, 713–726 (2013).
130. Vallee, R. B., Wall, J. S., Paschal, B. M. & Shpetner, H. S. Microtubule-associated protein 1C from brain is a two-headed cytosolic dynein. Nature **332**, 561–563 (1988).
131. L, U. et al. Cryo-EM shows how dynactin recruits two dyneins for faster movement. Nature **554**, 202–206 (2018).
132. L, U. et al. The structure of the dynactin complex and its interaction with dynein. Science **347**, 1441–1446 (2015).
133. IG, L. et al. A conserved interaction of the dynein light intermediate chain with dynein-dynactin effectors necessary for processivity. Nat. Commun. **9**, (2018).
134. CM, S., JM, O., NT, H. & RD, V. A Ras-like domain in the light intermediate chain bridges the dynein motor to a cargo-binding region. Elife **3**, 1–22 (2014).
135. CM, S. & RD, V. Assembly and activation of dynein-dynactin by the cargo adaptor protein Hook3. J. Cell Biol. **214**, 309–318 (2016).
136. AP, C., AG, D. & L, U. How dynein and dynactin transport cargos: a structural perspective. Curr. Opin. Struct. Biol. **37**, 62–70 (2016).
137. Waterman-Storer, C. M., Karki, S. & Holzbaur, E. L. The p150Glued component of the dynactin complex binds to both microtubules and the actin-related protein centractin (Arp-1). Proc. Natl. Acad. Sci. U. S. A. **92**, 1634 (1995).
138. Hamada, Y., Tsurumi, Y., Nozaki, S., Katoh, Y. & Nakayama, K. Interaction of WDR60 intermediate chain with TCTEX1D2 light chain of the dynein-2 complex is crucial for ciliary protein trafficking. https://doi.org/10.1091/mbc.E18-03-0173 **29**, 1628–1639 (2018).
139. Asante, D., Stevenson, N. L. & Stephens, D. J. Subunit composition of the human cytoplasmic dynein-2 complex. J. Cell Sci. **127**, 4774–4787 (2014).
140. Grissom, P. M., Vaisberg, E. A. & McIntosh, J. R. Identification of a Novel Light Intermediate Chain (D2LIC) for Mammalian Cytoplasmic Dynein 2. https://doi.org/10.1091/mbc.01-08-0402 **13**, 817–829 (2002).

141. Hou, Y., Pazour, G. J. & Witman, G. B. A Dynein Light Intermediate Chain, D1bLIC, Is Required for Retrograde Intraflagellar Transport. https://doi.org/10.1091/mbc.e04-05-0377 **15**, 4382–4394 (2004).
142. Li, W., Yi, P. & Ou, G. Somatic CRISPR–Cas9-induced mutations reveal roles of embryonically essential dynein chains in Caenorhabditis elegans cilia. J. Cell Biol. **208**, 683–692 (2015).
143. Mikami, A. et al. Molecular structure of cytoplasmic dynein 2 and its distribution in neuronal and ciliated cells. **2**, (2002).
144. Reck, J. et al. The role of the dynein light intermediate chain in retrograde IFT and flagellar function in Chlamydomonas. https://doi.org/10.1091/mbc.E16-03-0191 **27**, 2404–2422 (2016).
145. Asante, D. et al. A role for the Golgi matrix protein giantin in ciliogenesis through control of the localization of dynein-2. J. Cell Sci. **126**, 5189–5197 (2013).
146. Huber, C. et al. WDR34 Mutations that Cause Short-Rib Polydactyly Syndrome Type III/Severe Asphyxiating Thoracic Dysplasia Reveal a Role for the NF-κB Pathway in Cilia. Am. J. Hum. Genet. **93**, 926–931 (2013).
147. Schmidts, M. et al. Mutations in the Gene Encoding IFT Dynein Complex Component WDR34 Cause Jeune Asphyxiating Thoracic Dystrophy. Am. J. Hum. Genet. **93**, 932–944 (2013).
148. McInerney-Leo, A. M. et al. Short-Rib Polydactyly and Jeune Syndromes Are Caused by Mutations in WDR60. Am. J. Hum. Genet. **93**, 515–523 (2013).
149. Kanie, T. et al. The CEP19-RABL2 GTPase Complex Binds IFT-B to Initiate Intraflagellar Transport at the Ciliary Base. Dev. Cell **42**, 22-36.e12 (2017).
150. JB, G. et al. Molecular mechanism of dynein recruitment to kinetochores by the Rod-Zw10-Zwilch complex and Spindly. J. Cell Biol. **216**, 943–960 (2017).
151. Olenick, M. A. & Holzbaur, E. L. F. Dynein activators and adaptors at a glance. J. Cell Sci. **132**, (2019).
152. Chowdhury, S., Ketcham, S. A., Schroer, T. A. & Lander, G. C. Structural organization of the dynein-dynactin complex bound to microtubules. doi:10.1038/nsmb.2996
153. Splinter, D. et al. BICD2, dynactin, and LIS1 cooperate in regulating dynein recruitment to cellular structures. https://doi.org/10.1091/mbc.e12-03-0210 **23**, 4226–4241 (2012).
154. McKenney, R. J., Huynh, W., Tanenbaum, M. E., Bhabha, G. & Vale, R. D. Activation of cytoplasmic dynein motility by dynactin-cargo adapter complexes. Science (80-.). **345**, 337–341 (2014).
155. Hoogenraad, C. C. et al. Bicaudal D induces selective dynein-mediated microtubule minus end-directed transport. EMBO J. **22**, 6004–6015 (2003).
156. Wanschers, B. F. J. et al. A role for the Rab6B Bicaudal–D1 interaction in retrograde transport in neuronal cells. Exp. Cell Res. **313**, 3408–3420 (2007).
157. Hoogenraad, C. C. et al. Mammalian golgi-associated Bicaudal-D2 functions in the dynein-dynactin pathway by interacting with these complexes. EMBO J. **20**, 4041–4054 (2001).
158. Short, B., Preisinger, C., Schaletzky, J., Kopajtich, R. & Barr, F. A. The Rab6 GTPase Regulates Recruitment of the Dynactin Complex to Golgi Membranes. Curr. Biol. **12**, 1792–1795 (2002).
159. Schlager, M. A. et al. Pericentrosomal targeting of Rab6 secretory vesicles by Bicaudal-D-related protein 1 (BICDR-1) regulates neuritogenesis. EMBO J. **29**, 1637–1651 (2010).

160. Matanis, T. et al. Bicaudal-D regulates COPI-independent Golgi-ER transport by recruiting the dynein-dynactin motor complex. Nat. Cell Biol. **4**, 986–992 (2002).
161. SV, I., ME, B. & WJ, B. Bicaudal D1-dependent trafficking of human cytomegalovirus tegument protein pp150 in virus-infected cells. J. Virol. **84**, 3162–3177 (2010).
162. K, P. et al. Molecular defects in the motor adaptor BICD2 cause proximal spinal muscular atrophy with autosomal-dominant inheritance. Am. J. Hum. Genet. **92**, 955–964 (2013).
163. PM, H. et al. Purification, cloning, and characterization of Nek8, a novel NIMA-related kinase, and its candidate substrate Bicd2. J. Biol. Chem. **277**, 16229–16240 (2002).
164. EC, O. et al. Mutations in BICD2 cause dominant congenital spinal muscular atrophy and hereditary spastic paraplegia. Am. J. Hum. Genet. **92**, 965–973 (2013).
165. K, P. et al. Molecular defects in the motor adaptor BICD2 cause proximal spinal muscular atrophy with autosomal-dominant inheritance. Am. J. Hum. Genet. **92**, 955–964 (2013).
166. Splinter, D. et al. Bicaudal D2, dynein, and kinesin-1 associate with nuclear pore complexes and regulate centrosome and nuclear positioning during mitotic entry. PLoS Biol. **8**, (2010).
167. Terawaki, S. I., Yoshikane, A., Higuchi, Y. & Wakamatsu, K. Structural basis for cargo binding and autoinhibition of Bicaudal-D1 by a parallel coiled-coil with homotypic registry. Biochem. Biophys. Res. Commun. **460**, 451–456 (2015).
168. Y, L. et al. Bicaudal-D uses a parallel, homodimeric coiled coil with heterotypic registry to coordinate recruitment of cargos to dynein. Genes Dev. **27**, 1233–1246 (2013).
169. Wharton, R. P. & Struhl, G. Structure of the Drosophila BicaudalD protein and its role in localizing the posterior determinant nanos. Cell **59**, 881–892 (1989).
170. Sladewski, T. E. et al. Recruitment of two dyneins to an mRNA-dependent bicaudal D transport complex. Elife **7**, (2018).
171. Stuurman, N. et al. Interactions between coiled-coil proteins: Drosophila lamin Dm0 binds to the Bicaudal-D protein. Eur. J. Cell Biol. **78**, 278–287 (1999).
172. W, H. & RD, V. Disease-associated mutations in human BICD2 hyperactivate motility of dynein-dynactin. J. Cell Biol. **216**, 3051–3060 (2017).
173. MA, M. et al. RNA-directed activation of cytoplasmic dynein-1 in reconstituted transport RNPs. Elife **7**, (2018).
174. Grotjahn, D. A. et al. Cryo-electron tomography reveals that dynactin recruits a team of dyneins for processive motility. Nat. Struct. Mol. Biol. 2018 253 **25**, 203–207 (2018).
175. Schlager, M. A. et al. Bicaudal D Family Adaptor Proteins Control the Velocity of Dynein-Based Movements. Cell Rep. **8**, 1248–1256 (2014).
176. JH, W., AJ, D., X, L. & H, K. The Golgi-associated hook3 protein is a member of a novel family of microtubule-binding proteins. J. Cell Biol. **152**, 923–934 (2001).
177. MA, O., M, T., M, B., R, D. & EL, H. Hook Adaptors Induce Unidirectional Processive Motility by Enhancing the Dynein-Dynactin Interaction. J. Biol. Chem. **291**, 18239–18251 (2016).
178. K, L. et al. Interconnections of CLN3, Hook1 and Rab proteins link Batten disease to defects in the endocytic pathway. Hum. Mol. Genet. **13**, 3017–3027 (2004).

179. L, M.-B., NB, C., H, K. & JG, D. Microtubule-dependent endosomal sorting of clathrin-independent cargo by Hook1. J. Cell Biol. **201**, 233–247 (2013).
180. L, X. et al. An FTS/Hook/p107(FHIP) complex interacts with and promotes endosomal clustering by the homotypic vacuolar protein sorting complex. Mol. Biol. Cell **19**, 5059–5071 (2008).
181. X, G., GG, F., R, M. & JS, B. Rab5 and its effector FHF contribute to neuronal polarity through dynein-dependent retrieval of somatodendritic proteins from the axon. Proc. Natl. Acad. Sci. U. S. A. **113**, E5318–E5327 (2016).
182. G, S., B, H., R, Y., AI, H. & H, K. Hook2 localizes to the centrosome, binds directly to centriolin/CEP110 and contributes to centrosomal function. Traffic **8**, 32–46 (2007).
183. KL, M., R, P., PM, M., I, K. & DM, B. Murine CENP-F regulates centrosomal microtubule nucleation and interacts with Hook2 at the centrosome. Mol. Biol. Cell **20**, 4790–4803 (2009).
184. CR, G., GD, S. & BC, K. SUT-2 potentiates tau-induced neurotoxicity in Caenorhabditis elegans. Hum. Mol. Genet. **18**, 1825–1838 (2009).
185. D, D., A, K., S, R., SVS, M. & M, S. The dynein adaptor Hook2 plays essential roles in mitotic progression and cytokinesis. J. Cell Biol. **218**, 871–894 (2019).
186. MA, O., R, D. & ELF, H. Dynein activator Hook1 is required for trafficking of BDNF-signaling endosomes in neurons. J. Cell Biol. **218**, 220–233 (2019).
187. M, B. et al. Spindly/CCDC99 is required for efficient chromosome congression and mitotic checkpoint regulation. Mol. Biol. Cell **21**, 1968–1981 (2010).
188. ER, G., N, S. & RD, V. Spindly, a novel protein essential for silencing the spindle assembly checkpoint, recruits dynein to the kinetochore. J. Cell Biol. **177**, 1005–1015 (2007).
189. R, G. et al. Removal of Spindly from microtubule-attached kinetochores controls spindle checkpoint silencing in human cells. Genes Dev. **24**, 957–971 (2010).
190. R, G. et al. A new mechanism controlling kinetochore-microtubule interactions revealed by comparison of two dynein-targeting components: SPDL-1 and the Rod/Zwilch/Zw10 complex. Genes Dev. **22**, 2385–2399 (2008).
191. YW, C. et al. Mitotic control of kinetochore-associated dynein and spindle orientation by human Spindly. J. Cell Biol. **185**, 859–874 (2009).
192. CP, H., SR, H., RS, J., CE, F. & MW, M. Rab11-FIP3 links the Rab11 GTPase and cytoplasmic dynein to mediate transport to the endosomal-recycling compartment. J. Cell Sci. **123**, 181–191 (2010).
193. Yazaki, Y., Hara, Y., Tamaki, H., Fukaya, M. & Sakagami, H. Endosomal localization of FIP3/Arfophilin-1 and its involvement in dendritic formation of mouse hippocampal neurons. Brain Res. **1557**, 55–65 (2014).
194. Song, M. et al. Slitrk5 Mediates BDNF-Dependent TrkB Receptor Trafficking and Signaling. Dev. Cell **33**, 690–702 (2015).
195. Redwine, W. B. et al. The human cytoplasmic dynein interactome reveals novel activators of motility. Elife **6**, (2017).
196. Mogensen, M. M., Malik, A., Piel, M., Bouckson-Castaing, V. & Bornens, M. Microtubule minus-end anchorage at centrosomal and non-centrosomal sites: the role of ninein. J. Cell Sci. **113**, 3013–3023 (2000).
197. Dammermann, A. & Merdes, A. Assembly of centrosomal proteins and microtubule organization depends on PCM-1. J. Cell Biol. **159**, 255–266 (2002).
198. Delgehyr, N., Sillibourne, J. & Bornens, M. Microtubule nucleation and anchoring at the centrosome are independent processes linked by ninein function. J. Cell

Sci. **118**, 1565–1575 (2005).
199. Lechler, T. & Fuchs, E. Desmoplakin: an unexpected regulator of microtubule organization in the epidermis. J. Cell Biol. **176**, 147–154 (2007).
200. Dauber, A. et al. Novel Microcephalic Primordial Dwarfism Disorder Associated with Variants in the Centrosomal Protein Ninein. J. Clin. Endocrinol. Metab. **97**, E2140–E2151 (2012).
201. Bachmann-Gagescu, R. et al. The Ciliopathy Protein CC2D2A Associates with NINL and Functions in RAB8-MICAL3-Regulated Vesicle Trafficking. PLOS Genet. **11**, e1005575 (2015).
202. Dona, M. et al. NINL and DZANK1 Co-function in Vesicle Transport and Are Essential for Photoreceptor Development in Zebrafish. PLOS Genet. **11**, e1005574 (2015).
203. MacDonald, M. E. et al. A novel gene containing a trinucleotide repeat that is expanded and unstable on Huntington's disease chromosomes. Cell **72**, 971–983 (1993).
204. Engelender, S. et al. Huntingtin-associated Protein 1 (HAP1) Interacts with the p150Glued Bubunit of Dynactin. Hum. Mol. Genet. **6**, 2205–2212 (1997).
205. McGuire, J. R., Rong, J., Li, S.-H. & Li, X.-J. Interaction of Huntingtin-associated Protein-1 with Kinesin Light Chain: IMPLICATIONS IN INTRACELLULAR TRAFFICKING IN NEURONS*. J. Biol. Chem. **281**, 3552–3559 (2006).
206. Twelvetrees, A. E. et al. Delivery of GABAARs to Synapses Is Mediated by HAP1-KIF5 and Disrupted by Mutant Huntingtin. Neuron **65**, 53–65 (2010).
207. Yang, G.-Z. et al. Huntingtin associated protein 1 regulates trafficking of the amyloid precursor protein and modulates amyloid beta levels in neurons. J. Neurochem. **122**, 1010–1022 (2012).
208. Wong, Y. C. & Holzbaur, E. L. F. The Regulation of Autophagosome Dynamics by Huntingtin and HAP1 Is Disrupted by Expression of Mutant Huntingtin, Leading to Defective Cargo Degradation. J. Neurosci. **34**, 1293–1305 (2014).
209. Gunawardena, S. et al. Disruption of Axonal Transport by Loss of Huntingtin or Expression of Pathogenic PolyQ Proteins in Drosophila. Neuron **40**, 25–40 (2003).
210. Weiss, K. R. & Littleton, J. T. Characterization of axonal transport defects in Drosophila Huntingtin mutants. https://doi.org/10.1080/01677063.2016.1202950 **30**, 212–221 (2016).
211. Colin, E. et al. Huntingtin phosphorylation acts as a molecular switch for anterograde/retrograde transport in neurons. EMBO J. **27**, 2124–2134 (2008).
212. Her, L.-S. & Goldstein, L. S. B. Enhanced Sensitivity of Striatal Neurons to Axonal Transport Defects Induced by Mutant Huntingtin. J. Neurosci. **28**, 13662–13672 (2008).
213. RS, S., LJ, M., J, G.-A., IA, M. & TL, S. Axonal transport of mitochondria to synapses depends on milton, a novel Drosophila protein. Neuron **36**, 1063–1077 (2002).
214. Y, F., L, S., X, T., M, G. & NM, B. A novel Drosophila model of nerve injury reveals an essential role of Nmnat in maintaining axonal integrity. Curr. Biol. **22**, 590–595 (2012).
215. J, G.-A. et al. Mitochondria are redistributed in Drosophila photoreceptors lacking milton, a kinesin-associated protein. J. Comp. Neurol. **463**, 372–388 (2003).
216. O, L. & FA, S. Localization of the kinesin adaptor proteins trafficking kinesin

proteins 1 and 2 in primary cultures of hippocampal pyramidal and cortical neurons. J. Neurosci. Res. **93**, 1056–1066 (2015).
217. M, van S. et al. TRAK/Milton motor-adaptor proteins steer mitochondrial trafficking to axons and dendrites. Neuron **77**, 485–502 (2013).
218. T, K. & F, M. Evidence that dendritic mitochondria negatively regulate dendritic branching in pyramidal neurons in the neocortex. J. Neurosci. **34**, 6938–6951 (2014).
219. Cantalupo, G., Alifano, P., Roberti, V., Bruni, C. B. & Bucci, C. Rab-interacting lysosomal protein (RILP): the Rab7 effector required for transport to lysosomes. EMBO J. **20**, 683–693 (2001).
220. Jordens, I. et al. The Rab7 effector protein RILP controls lysosomal transport by inducing the recruitment of dynein-dynactin motors. Curr. Biol. **11**, 1680–1685 (2001).
221. Johansson, M. et al. Activation of endosomal dynein motors by stepwise assembly of Rab7–RILP–p150Glued, ORP1L, and the receptor βIII spectrin. J. Cell Biol. **176**, 459–471 (2007).
222. Dickens, M. et al. A Cytoplasmic Inhibitor of the JNK Signal Transduction Pathway. Science (80-.). **277**, 693–696 (1997).
223. Yasuda, J., Whitmarsh, A. J., Cavanagh, J., Sharma, M. & Davis, R. J. The JIP Group of Mitogen-Activated Protein Kinase Scaffold Proteins. Mol. Cell. Biol. **19**, 7245–7254 (1999).
224. Kelkar, N., Standen, C. L. & Davis, R. J. Role of the JIP4 Scaffold Protein in the Regulation of Mitogen-Activated Protein Kinase Signaling Pathways. Mol. Cell. Biol. **25**, 2733–2743 (2005).
225. Verhey, K. J. et al. Cargo of Kinesin Identified as Jip Scaffolding Proteins and Associated Signaling Molecules. J. Cell Biol. **152**, 959–970 (2001).
226. Bowman, A. B. et al. Kinesin-Dependent Axonal Transport Is Mediated by the Sunday Driver (SYD) Protein. Cell **103**, 583–594 (2000).
227. Montagnac, G. et al. ARF6 Interacts with JIP4 to Control a Motor Switch Mechanism Regulating Endosome Traffic in Cytokinesis. Curr. Biol. **19**, 184–195 (2009).
228. Fu, M. & Holzbaur, E. L. F. JIP1 regulates the directionality of APP axonal transport by coordinating kinesin and dynein motors. J. Cell Biol. **202**, 495–508 (2013).
229. Cavalli, V., Kujala, P., Klumperman, J. & Goldstein, L. S. B. Sunday Driver links axonal transport to damage signaling. J. Cell Biol. **168**, 775–787 (2005).
230. Gowrishankar, S., Wu, Y. & Ferguson, S. M. Impaired JIP3-dependent axonal lysosome transport promotes amyloid plaque pathology. J. Cell Biol. **216**, 3291–3305 (2017).
231. Drerup, C. M. & Nechiporuk, A. V. JNK-Interacting Protein 3 Mediates the Retrograde Transport of Activated c-Jun N-Terminal Kinase and Lysosomes. PLOS Genet. **9**, e1003303 (2013).
232. Edwards, S. L. et al. An Organelle Gatekeeper Function for Caenorhabditis elegans UNC-16 (JIP3) at the Axon Initial Segment. Genetics **194**, 143–161 (2013).
233. Zheng, S. Q. et al. MotionCor2: anisotropic correction of beam-induced motion for improved cryo-electron microscopy. Nat. Methods **14**, 331–332 (2017).
234. Zhang, K. Gctf: Real-time CTF determination and correction. J. Struct. Biol. **193**, 1–12 (2016).

235. Kimanius, D., Forsberg, B. O., Scheres, S. H. W. & Lindahl, E. Accelerated cryo-EM structure determination with parallelisation using GPUs in RELION-2. Elife **5**, (2016).
236. Gillies, J. P. et al. Structural Basis for Cytoplasmic Dynein-1 Regulation by Lis1. bioRxiv 2021.06.11.448119 (2021). doi:10.1101/2021.06.11.448119
237. Huang, L. Y. et al. Unnatural amino acid replacement in a yeast G protein-coupled receptor in its native environment. Biochemistry **47**, 5638–5648 (2008).
238. Rogerson, D. T. et al. Efficient genetic encoding of phosphoserine and its nonhydrolyzable analog. Nat. Chem. Biol. 2015 117 **11**, 496–503 (2015).
239. Chhetri, G., Kalita, P. & Tripathi, T. An efficient protocol to enhance recombinant protein expression using ethanol in Escherichia coli. MethodsX **2**, 385–391 (2015).
240. Wang, Y. & Li, Y. Z. Cultivation to improve in vivo solubility of overexpressed arginine deiminases in Escherichia coli and the enzyme characteristics. BMC Biotechnol. **14**, 1–10 (2014).
241. (13) (PDF) Enhancement of the solubility of proteins overexpressed in Escherichia coli by heat shock. Available at: https://www.researchgate.net/publication/11034438_Enhancement_of_the_solubility_of_proteins_overexpressed_in_Escherichia_coli_by_heat_shock. (Accessed: 22nd December 2021)
242. Seddon, A. M., Curnow, P. & Booth, P. J. Membrane proteins, lipids and detergents: not just a soap opera. Biochim. Biophys. Acta - Biomembr. **1666**, 105–117 (2004).
243. Detergents for Cell Lysis and Protein Extraction | Thermo Fisher Scientific - FR. Available at: https://www.thermofisher.com/fr/fr/home/life-science/protein-biology/protein-biology-learning-center/protein-biology-resource-library/pierce-protein-methods/detergents-cell-lysis-protein-extraction.html?ef_id=CjwKCAiAtouOBhA6EiwA2nLKH19gI-fFG6Ku_Xy8sY9a6ZvW2hY3b9EZnfAc9vZAM_oJD9Drfp19MRoC4fUQAvD_BwE:G:s&s_kwcid=AL!3652!3!386235918378!!!g!!&cid=bid_pca_ppf_r01_co_cp1359_pjt0000_bid00000_0se_gaw_dy_pur_con&gclid=CjwKCAiAtouOBhA6EiwA2nLKH19gI-fFG6Ku_Xy8sY9a6ZvW2hY3b9EZnfAc9vZAM_oJD9Drfp19MRoC4fUQAvD_BwE. (Accessed: 22nd December 2021)
244. Hjelmeland, L. M. A nondenaturing zwitterionic detergent for membrane biochemistry: design and synthesis. Proc. Natl. Acad. Sci. **77**, 6368–6370 (1980).
245. Baffet, A. D., Hu, D. J. & Vallee, R. B. Cdk1 Activates Pre-mitotic Nuclear Envelope Dynein Recruitment and Apical Nuclear Migration in Neural Stem Cells. Dev. Cell **33**, 703–716 (2015).
246. Gibson 1$, J. M. et al. Coil-to-Helix Transition at the Nup358-BicD2 Interface for Dynein Recruitment and Activation. bioRxiv 2021.05.06.443034 (2021). doi:10.1101/2021.05.06.443034
247. Gonçalves, J. C., Quintremil, S., Yi, J. & Vallee, R. B. Nesprin-2 Recruitment of BicD2 to the Nuclear Envelope Controls Dynein/Kinesin-Mediated Neuronal Migration In Vivo. Curr. Biol. **30**, 3116-3129.e4 (2020).
248. Designed Research; A, E. M. C. D. Bicaudal D2 facilitates the cytoplasmic trafficking and nuclear import of HIV-1 genomes during infection. doi:10.1073/pnas.1712033114
249. Gibson, D. G. et al. Enzymatic assembly of DNA molecules up to several

hundred kilobases. Nat. Methods 2009 65 **6**, 343–345 (2009).
250. Zivanov, J. et al. New tools for automated high-resolution cryo-EM structure determination in RELION-3. Elife **7**, (2018).
251. J, C., H, P. & C, S. How does a registry change in dynein's coiled-coil stalk drive binding of dynein to microtubules? Biochemistry **50**, 7629–7636 (2011).
252. Kon, T. et al. Helix sliding in the stalk coiled coil of dynein couples ATPase and microtubule binding. Nat. Struct. Mol. Biol. **16**, 325–333 (2009).

Résumé en français suivi des mots-clés en français

Les dynéines cytoplasmiques dirigent la majorité des événements de transport rétrograde des microtubules dans les cellules eucaryotes. La dynéine cytoplasmique-1 est impliquée dans la division cellulaire, le transport des organelles et des vésicules, le développement du cerveau et des muscles, tandis que la dynéine cytoplasmique-2 facilite l'assemblage des flagelles dans les cellules de mammifères. Dans le cortex en développement, la dynéine-1, la dynactine et l'adaptateur de cargaison BicD2 sont recrutés vers le noyau, pour les déplacer du côté apical vers le côté basal du néocortex. L'adaptateur de cargaison BicD2 est une protéine de liaison allongée et flexible qui interagit avec le moteur dynéine dirigé vers l'extrémité négative, le moteur kinésine-1 dirigé vers l'extrémité positive, les composants du pore nucléaire, l'ARN et les particules virales. Ce travail se concentre sur deux aspects fondamentaux du transport médié par la dynéine : comment la dynéine génère-t-elle la force nécessaire au mouvement via le remodelage de la liaison, et comment l'adaptateur de cargaison humain BicD2 médiatise-t-il l'interaction avec sa cargaison ?

Mots-clés : dynéine-1, dynéine-2, BicD2, cryoEM, biophysique.

Résumé en anglais suivi des mots-clés en anglais

Cytoplasmic dyneins drive the majority of the retrograde microtubule transport events in eukaryotic cells. Cytoplasmic dynein-1 is involved in cell division, transport of organelles and vesicles, brain and muscle development, while cytoplasmic dynein-2 facilitates flagella assembly in mammalian cells. In the developing cortex, dynein-1, dynactin, and the BicD2 cargo adaptor are recruited to the nucleus, to move it from the apical to the basal side of the neocortex. The BicD2 cargo adaptor is an elongated, flexible linker protein mediating interaction with the minus-end directed dynein motor, the plus-end motor kinesin-1, nuclear pore components, RNA, and viral particles. This work focuses on two fundamental aspects of dynein-mediated transport: how does dynein generate force for movement via linker remodeling, and second how does human cargo adaptor BicD2 mediates the interaction with its cargo.

Keywords: dynein-1, dynein-2, BicD2, cryoEM, biophysics.